Planck 2015 results: X. Diffuse component separation: Foreground maps

Adam, R.; Ade, P. A R; Aghanim, N.; Alves, M. I R; Arnaud, M.; Ashdown, M.; Aumont, J.; Baccigalupi, C.; Banday, A. J.; Barreiro, R. B.

Total number of authors:
239

Published in:
Astronomy and Astrophysics

Link to article, DOI:
10.1051/0004-6361/201525967

Publication date:
2016

Document Version
Publisher's PDF, also known as Version of record

A&A 594, A10 (2016)
DOI: 10.1051/0004-6361/201525967

Astronomy & Astrophysics
Special feature

Planck 2015 results

Planck 2015 results

X. Diffuse component separation: Foreground maps

Planck Collaboration: R. Adam[82], P. A. R. Ade[97], N. Aghanim[65], M. I. R. Alves[107,11,65], M. Arnaud[80], M. Ashdown[76,6], J. Aumont[65], C. Baccigalupi[95], A. J. Banday[107,11], R. B. Barreiro[71], J. G. Bartlett[1,73], N. Bartolo[33,72], E. Battaner[109,110], K. Benabed[66,106], A. Benoît[63], A. Benoit-Lévy[27,66,106], J.-P. Bernard[107,11], M. Bersanelli[36,53], P. Bielewicz[90,11,95], J. J. Bock[73,13], A. Bonaldi[74], L. Bonavera[71], J. R. Bond[10], J. Borrill[16,101], F. R. Bouchet[66,99], F. Boulanger[65], M. Bucher[1], C. Burigana[52,34,54], R. C. Butler[52], E. Calabrese[103], J.-F. Cardoso[81,1,66], A. Catalano[82,79], A. Challinor[68,76,14], A. Chamballu[80,18,65], R.-R. Chary[62], H. C. Chiang[30,7], P. R. Christensen[91,39], D. L. Clements[61], S. Colombi[66,106], L. P. L. Colombo[26,73], C. Combet[82], F. Couchot[78], A. Coulais[79], B. P. Crill[73,13], A. Curto[71,6,76], F. Cuttaia[52], L. Danese[95], R. D. Davies[74], R. J. Davis[74], P. de Bernardis[35], A. de Rosa[52], G. de Zotti[49,95], J. Delabrouille[1], F.-X. Désert[59], C. Dickinson[74], J. M. Diego[71], H. Dole[65,64], S. Donzelli[53], O. Doré[73,13], M. Douspis[65], A. Ducout[66,61], X. Dupac[42], G. Efstathiou[68], F. Elsner[27,66,106], T. A. Enßlin[86], H. K. Eriksen[69], E. Falgarone[79], J. Fergusson[14], F. Finelli[52,54], O. Forni[107,11], M. Frailis[51], A. A. Fraisse[30], E. Franceschi[52], A. Frejsel[91], S. Galeotta[51], S. Galli[75], K. Ganga[1], T. Ghosh[65], M. Giard[107,11], Y. Giraud-Héraud[1], E. Gjerløw[69], J. González-Nuevo[22,71], K. M. Górski[73,112], S. Gratton[76,68], A. Gregorio[37,51,58], A. Gruppuso[52], J. E. Gudmundsson[104,93,30], F. K. Hansen[69], D. Hanson[88,73,10], D. L. Harrison[68,76], G. Helou[13], S. Henrot-Versillé[78], C. Hernández-Monteagudo[15,86], D. Herranz[71], S. R. Hildebrandt[73,13], E. Hivon[66,106], M. Hobson[6], W. A. Holmes[73], A. Hornstrup[19], W. Hovest[86], K. M. Huffenberger[28], G. Hurier[65], A. H. Jaffe[61], T. R. Jaffe[107,11], W. C. Jones[30], M. Juvela[29], E. Keihänen[29], R. Keskitalo[16], T. S. Kisner[84], R. Kneissl[41,8], J. Knoche[86], M. Kunz[20,65,3], H. Kurki-Suonio[29,47], G. Lagache[5,65], A. Lähteenmäki[2,47], J.-M. Lamarre[79], A. Lasenby[6,76], M. Lattanzi[34,55], C. R. Lawrence[73], M. Le Jeune[1], J. P. Leahy[74], R. Leonardi[9], J. Lesgourgues[67,105], F. Levrier[79], M. Liguori[33,72], P. B. Lilje[69], M. Linden-Vørnle[19], M. López-Caniego[42,71], P. M. Lubin[31], J. F. Macías-Pérez[82], G. Maggio[51], D. Maino[36,53], N. Mandolesi[52,34], A. Mangilli[65,78], M. Maris[51], D. J. Marshall[80], P. G. Martin[10], E. Martínez-González[71], S. Masi[35], S. Matarrese[33,72,44], P. McGehee[62], P. R. Meinhold[31], A. Melchiorri[35,56], L. Mendes[42], A. Mennella[36,53], M. Migliaccio[68,76], S. Mitra[60,73], M.-A. Miville-Deschênes[65,10], A. Moneti[66], L. Montier[107,11], G. Morgante[52], D. Mortlock[61], A. Moss[98], D. Munshi[97], J. A. Murphy[89], P. Naselsky[92,40], F. Nati[30], P. Natoli[34,4,55], C. B. Netterfield[23], H. U. Nørgaard-Nielsen[19], F. Noviello[74], D. Novikov[85], I. Novikov[91,85], E. Orlando[111], C. A. Oxborrow[19], F. Paci[95], L. Pagano[35,56], F. Pajot[65], R. Paladini[62], D. Paoletti[52,54], B. Partridge[46], F. Pasian[51], G. Patanchon[1], T. J. Pearson[13,62], O. Perdereau[78], L. Perotto[82], F. Perrotta[95], V. Pettorino[45], F. Piacentini[35], M. Piat[1], E. Pierpaoli[26], D. Pietrobon[73], S. Plaszczynski[78], E. Pointecouteau[107,11], G. Polenta[4,50], G. W. Pratt[80], G. Prézeau[13,73], S. Prunet[66,106], J.-L. Puget[65], J. P. Rachen[24,86], W. T. Reach[108], R. Rebolo[70,17,21], M. Reinecke[86], M. Remazeilles[74,65,1], C. Renault[82], A. Renzi[38,57], I. Ristorcelli[107,11], G. Rocha[73,13], C. Rosset[1], M. Rossetti[36,53], G. Roudier[1,79,73], J. A. Rubiño-Martín[70,21], B. Rusholme[62], M. Sandri[52], D. Santos[82], M. Savelainen[29,47], G. Savini[94], D. Scott[25], M. D. Seiffert[73,13], E. P. S. Shellard[14], L. D. Spencer[97], V. Stolyarov[6,102,77], R. Stompor[1], A. W. Strong[87], R. Sudiwala[97], R. Sunyaev[86,100], D. Sutton[68,76], A.-S. Suur-Uski[29,47], J.-F. Sygnet[66], J. A. Tauber[43], L. Terenzi[96,52], L. Toffolatti[22,71,52], M. Tomasi[36,53], M. Tristram[78], M. Tucci[20], J. Tuovinen[12], G. Umana[48], L. Valenziano[52], J. Valiviita[29,47], F. Van Tent[83], P. Vielva[71], F. Villa[52], L. A. Wade[73], B. D. Wandelt[66,106,32], I. K. Wehus[73,69,⋆], A. Wilkinson[74], D. Yvon[18], A. Zacchei[51], and A. Zonca[31]

(Affiliations can be found after the references)

Received 26 February 2015 / Accepted 22 February 2016

ABSTRACT

Planck has mapped the microwave sky in temperature over nine frequency bands between 30 and 857 GHz and in polarization over seven frequency bands between 30 and 353 GHz in polarization. In this paper we consider the problem of diffuse astrophysical component separation, and process these maps within a Bayesian framework to derive an internally consistent set of full-sky astrophysical component maps. Component separation dedicated to cosmic microwave background (CMB) reconstruction is described in a companion paper. For the temperature analysis, we combine the *Planck* observations with the 9-yr *Wilkinson* Microwave Anisotropy Probe (WMAP) sky maps and the Haslam et al. 408 MHz map, to derive a joint model of CMB, synchrotron, free-free, spinning dust, CO, line emission in the 94 and 100 GHz channels, and thermal dust emission. Full-sky maps are provided for each component, with an angular resolution varying between 7.′5 and 1°. Global parameters (monopoles, dipoles, relative calibration, and bandpass errors) are fitted jointly with the sky model, and best-fit values are tabulated. For polarization, the model includes CMB, synchrotron, and thermal dust emission. These models provide excellent fits to the observed data, with rms temperature residuals smaller than $4\,\mu$K over 93% of the sky for all *Planck* frequencies up to 353 GHz, and fractional errors smaller than 1% in the remaining 7% of the sky. The main limitations of the temperature model at the lower frequencies are internal degeneracies among the spinning dust, free-free, and synchrotron components; additional observations from external low-frequency experiments will be essential to break these degeneracies. The main limitations of the temperature model at the higher frequencies are uncertainties in the 545 and 857 GHz calibration and zero-points. For polarization, the main outstanding issues are instrumental systematics in the 100–353 GHz bands on large angular scales in the form of temperature-to-polarization leakage, uncertainties in the analogue-to-digital conversion, and corrections for the very long time constant of the bolometer detectors, all of which are expected to improve in the near future.

Key words. ISM: general – cosmology: observations – polarization – cosmic background radiation – diffuse radiation – Galaxy: general

⋆ Corresponding author: I. K. Wehus; i.k.wehus@astro.uio.no

1. Introduction

This paper, one of a set associated with the 2015 release of data from the *Planck*[1] mission (Planck Collaboration I 2016), presents a coherent astrophysical model of the microwave sky in both temperature and polarization, as derived from the most recent *Planck* observations. For temperature, the analysis also incorporates the 9-yr WMAP observations (Bennett et al. 2013) and a 408 MHz survey (Haslam et al. 1982), allowing the separation of synchrotron, free-free, and spinning dust emission.

In March 2013, the *Planck* Consortium released its first temperature measurements of the microwave sky, summarized in terms of nine frequency maps between 30 and 857 GHz (Planck Collaboration I 2014). The richness of these data has enabled great progress in our understanding of the astrophysical composition of the microwave sky. The current *Planck* data release presents additionally high-sensitivity, full-sky maps of the polarized microwave sky, offering a fresh view on both cosmological and astrophysical phenomena.

With increased data volume and quality comes both greater scientific potential and more stringent requirements on model complexity and sophistication. The current *Planck* data release is more ambitious than the 2013 release in terms of component separation efforts, accounting for more astrophysical effects and components. In this round, three related papers summarize the *Planck* 2015 component separation products and approaches. First, cosmic microwave background (CMB) reconstruction and extraction are discussed in Planck Collaboration IX (2016). Second, this paper presents the diffuse astrophysical foreground products derived from the 2015 *Planck* observations, both in temperature and polarization. Third, Planck Collaboration XXV (2016) discusses the scientific interpretation of the new low-frequency *Planck* foreground products.

The main goal of the current paper is to establish a single, internally coherent and global parametric model of the microwave sky, simultaneously accounting for all significant diffuse astrophysical components and relevant instrumental effects using the Bayesian `Commander` analysis framework (Eriksen et al. 2004, 2006, 2008). As such, our discussion does not focus on any single emission component, but rather emphasize the global picture. In the 2013 data release, the same framework was applied to the *Planck* temperature measurements for frequencies between 30 and 353 GHz, considering only angular scales larger than 40′ full-width half-maximum (FWHM). This resulted in low-resolution CMB, CO, and thermal dust emission maps, as well as a single low-frequency foreground component combining contributions from synchrotron, free-free, and spinning dust emission (Planck Collaboration XII 2014). Here we extend that analysis in multiple directions. First, instead of 15.5 months of temperature data, the new analysis includes the full *Planck* mission data, 50 months of Low Frequency Instrument (LFI) and 29 months of High Frequency Instrument (HFI) data, in both temperature and polarization. Second, we now also include the 9-yr WMAP observations between 23 and 94 GHz and a 408 MHz survey map, providing enough frequency constraints to decompose the low-frequency foregrounds into separate synchrotron, free-free, and spinning dust components. Third, we now include the *Planck* 545 and 857 GHz frequency bands, allowing us to constrain the thermal dust temperature and emissivity index with greater precision, thereby reducing degeneracies between CMB, CO, and free-free emission. At the same time, we find that the calibration and bandpass measurements of these two channels represent two of the most important sources of systematic uncertainty in the analysis. Fourth, the present analysis implements a multi-resolution strategy to provide component maps at high angular resolution. Specifically, the CMB is recovered with angular resolution 5′ FWHM (Planck Collaboration IX 2016), thermal dust emission and CO $J = 2 \rightarrow 1$ lines are recovered at 7.′5 FWHM, and synchrotron, free-free, and spinning dust are recovered at 1° FWHM. The resulting parameter fits define the *Planck* 2015 baseline astrophysical model in temperature and polarization. We emphasize, however, that these models are not unique, but instead represent minimal physically well-motivated models that are able to reproduce the current data.

As in the 2013 data release, the CMB solutions derived, using this Bayesian approach, form the basis of the *Planck* 2015 CMB temperature likelihood on large angular scales. This is described in detail in Planck Collaboration XI (2016), which also presents a detailed characterization of the low-multipole CMB angular power spectrum. The low-frequency astrophysical model presented here is used as input for the temperature-to-polarization bandpass mismatch corrections for the LFI polarization maps (Planck Collaboration II 2016).

The paper is organized as follows. Section 2 gives an overview of the computational framework implemented in the `Commander` code. Section 3 describes the data selection and processing. Section 4, gives an overview of the relevant astrophysical components and systematic effects. Sections 5 and 6 give the main temperature and polarization products. We summarize in Sect. 7.

2. Algorithms

2.1. Data, posterior distribution and priors

Most of the results derived in this paper are established within a standard Bayesian analysis framework, as implemented in the `Commander` code, in which an explicit parametric model, $\boldsymbol{s}(\theta)$, is fitted to a set of observations, $\boldsymbol{d}$, either by maximizing or mapping out the corresponding posterior distribution,

$$P(\theta|\boldsymbol{d}) = \frac{P(\boldsymbol{d}|\theta)P(\theta)}{P(\boldsymbol{d})} \propto \mathcal{L}(\theta)P(\theta). \quad (1)$$

Here θ denotes some general set of free parameters in the model, $\mathcal{L}(\theta) = P(\boldsymbol{d}|\theta)$ is the likelihood, and $P(\theta)$ denotes a set of priors on θ. The evidence, $P(\boldsymbol{d})$, is a constant with respect to the parameter set, and is neglected in the following.

The data are defined by a set of pixelized frequency-channel sky maps, $\boldsymbol{d} = \{\boldsymbol{d}_\nu\}$, comprising the three Stokes parameters I, Q and U. In this paper, however, we analyse temperature and polarization separately; therefore the data vector comprises either I or $\{Q, U\}$.

We start by assuming that the data at a given frequency ν may be described as a linear sum of signal $\boldsymbol{s}_\nu$ and noise $\boldsymbol{n}_\nu$,

$$\boldsymbol{d}_\nu = \boldsymbol{s}_\nu + \boldsymbol{n}_\nu, \quad (2)$$

where $\boldsymbol{n}_\nu$ is assumed to be Gaussian-distributed with a known covariance matrix N_ν. For the signal, we adopt the following parametric expression:

$$\boldsymbol{s}_\nu(\theta) = s_\nu(\boldsymbol{a}_i, \beta_i, g_\nu, \boldsymbol{m}_\nu, \Delta_\nu) \quad (3)$$

$$= g_\nu \sum_{i=1}^{N_{\rm comp}} \mathsf{F}^i_\nu(\beta_i, \Delta_\nu)\boldsymbol{a}_i + \mathsf{T}_\nu \boldsymbol{m}_\nu, \quad (4)$$

[1] *Planck* (`http://www.esa.int/Planck`) is a project of the European Space Agency (ESA) with instruments provided by two scientific consortia funded by ESA member states and led by Principal Investigators from France and Italy, telescope reflectors provided through a collaboration between ESA and a scientific consortium led and funded by Denmark, and additional contributions from NASA (USA).

where $\boldsymbol{a}_i$ is an amplitude map for component i at a given reference frequency, β_i is a general set of spectral parameters for the same component, g_ν is a multiplicative calibration factor for frequency ν, Δ_ν is a linear shift in the bandpass central frequency, and $\boldsymbol{m}_\nu$ is a set of template correction amplitudes, such as monopole, dipole, or zodiacal light corrections for temperature, or calibration leakage templates for polarization. The corresponding spatially fixed templates are organized column-wise in a template matrix T_ν. The mixing matrix, $\mathsf{F}^i_\nu(\beta_i, \Delta_\nu)$, accounts for the effect of spectral changes as a function of frequency for component i, parametrized by β_i, as well as bandpass integration effects and unit conversions. For numerical stability, all internal calculations are performed in units of brightness temperature, and $\boldsymbol{a}$ is therefore naturally defined in the same units at some specified reference frequency.

The posterior distribution takes the usual form,

$$\begin{aligned} P(\theta|\boldsymbol{d}_\nu) &= P(\boldsymbol{d}_\nu|\boldsymbol{a}_i, \beta_i, g_\nu, \boldsymbol{m}_\nu, \Delta_\nu, C_\ell) P(\boldsymbol{a}_i, \beta_i, g_\nu, \boldsymbol{m}_\nu, \Delta_\nu, C_\ell) \\ &= \mathcal{L}(\boldsymbol{a}_i, \beta_i, g_\nu, \boldsymbol{m}_\nu, \Delta_\nu) P(\boldsymbol{a}_i) P(\beta_i) P(\boldsymbol{a}_{\rm cmb}|C_\ell), \end{aligned} \tag{5}$$

where we have included the CMB power spectrum, C_ℓ, and also implicitly adopted uniform priors on $\boldsymbol{g}_\nu$, Δ_ν, $\boldsymbol{m}_\nu$, and C_ℓ. Because the noise is assumed to be Gaussian and independent between frequency channels, the likelihood reads

$$\mathcal{L}(\boldsymbol{a}_i, \beta_i, g_\nu, \boldsymbol{m}_\nu, \Delta_\nu) \propto \exp\left(-\frac{1}{2}\sum_\nu [\boldsymbol{d}_\nu - \boldsymbol{s}_\nu(\theta)]^{\rm T} \mathsf{N}^{-1} [\boldsymbol{d}_\nu - \boldsymbol{s}_\nu(\theta)]\right) \tag{6}$$

Likewise, we further assume the CMB signal to be Gaussian distributed with a covariance matrix, $\mathsf{S}(C_\ell)$, given by the power spectrum, and the corresponding CMB prior factor therefore reads

$$P(\boldsymbol{a}_{\rm cmb}|C_\ell) = \frac{e^{-\frac{1}{2}\boldsymbol{a}^{\rm T}_{\rm cmb}\mathsf{S}^{-1}(C_\ell)\boldsymbol{a}_{\rm cmb}}}{\sqrt{|\mathsf{S}(C_\ell)|}}. \tag{7}$$

The only undefined factors in the posterior are the amplitude and spectral parameter priors, $P(\boldsymbol{a}^i)$ and $P(\beta^i)$. These represent the most difficult problem to handle from a conceptual point of view, since the prior is to some extent a matter of personal preference. However, we adopt the following general practices in this paper. First, for low-resolution analyses that include fitting of template amplitudes (e.g., monopoles and dipoles), we always impose a strict positivity prior, i.e., $\boldsymbol{a}_i > 0$, on all signal amplitudes except the CMB. Without such a prior, there are large degeneracies between the zero-points of the amplitude maps and the individual template amplitudes. Second, for the high angular resolution analysis, we fix the template amplitudes at the low-resolution values and disable the positivity prior, in order to avoid noise bias. Third, to further break degeneracies, we adopt fiducial values for the monopole, dipole, and calibration factors for a few selected channels, effectively imposing a set of external priors from CMB dipole measurements and H I cross-correlation (Planck Collaboration VIII 2014) to anchor the full solution. Fourth, for the spectral parameters, we adopt Gaussian priors with means and variances informed by the high signal-to-noise values observed in the Galactic plane, which for all practical purposes are independent of the adopted priors. Intuitively, we demand that a map of the spectral parameter in question should not be much different in the data-dominated and the prior-dominated regions of the sky. Fourth, one of the components in the temperature model is free-free emission, which has two free parameters, namely the effective emission measure, EM, and the electron temperature, $T_{\rm e}$. The latter of these is very poorly constrained with the current data set except in the central Galactic plane, and we therefore adopt a smoothness prior on this paper to increase the effective signal-to-noise ratio, demanding that is must be smooth on 2° FWHM scales. This in turn has a large computational cost by making the overall foreground parameter estimation process non-local, and $T_{\rm e}$ is therefore only varied in fast maximum-likelihood searches, not in expensive sampling analyses. Its effect on other parameters is, however, minimal, precisely because of its low signal-to-noise ratio. Finally, in addition to these informative priors, we adopt a Jeffreys prior for the spectral parameters in order to suppress prior volume effects (Jeffreys 1946; Eriksen et al. 2008; Dunkley et al. 2009).

2.2. Gibbs sampling and posterior maximization

As described above, the posterior distribution contains many millions of free (both non-Gaussian and strongly correlated) parameters for *Planck* – ranging from 11 million in the following low-resolution analysis to 200 million in the corresponding high-resolution analysis – and mapping out this distribution poses a significant computational problem. Indeed, no direct sampling algorithm exists for the full distribution, and the only computationally efficient solution currently known is that of Gibbs sampling, a well-known textbook algorithm in modern statistical analysis (e.g., Gelman et al. 2003). The underlying idea of this method is that samples from a complicated multivariate distribution may be drawn by iteratively sampling over the corresponding conditional distributions, which usually have much simpler, and often analytic, sampling algorithms. This framework was originally introduced to the CMB analysis field by Jewell et al. (2004) and Wandelt et al. (2004), and subsequently developed into a fully functional computer code called `Commander` by Eriksen et al. (2004, 2008).

For the problem in question in this paper, this algorithm may be schematically translated into an explicit set of sampling steps through the following Gibbs chain:

$$\boldsymbol{a}_i \leftarrow P(\boldsymbol{a}_i|\beta_i, g_\nu, \boldsymbol{m}_\nu, \Delta_\nu, C_\ell) \tag{8}$$
$$\beta_i \leftarrow P(\beta_i|\boldsymbol{a}_i, g_\nu, \boldsymbol{m}_\nu, \Delta_\nu, C_\ell) \tag{9}$$
$$g_\nu \leftarrow P(g_\nu|\boldsymbol{a}_i, \beta_i, \boldsymbol{m}_\nu, \Delta_\nu, C_\ell) \tag{10}$$
$$\boldsymbol{m}_\nu \leftarrow P(m_\nu|\boldsymbol{a}_i, \beta_i, g_\nu, \Delta_\nu, C_\ell) \tag{11}$$
$$\Delta_\nu \leftarrow P(\Delta_\nu|\boldsymbol{a}_i, \beta_i, g_\nu, \boldsymbol{m}_\nu, C_\ell) \tag{12}$$
$$C_\ell \leftarrow P(C_\ell|\boldsymbol{a}_i, \beta_i, g_\nu, \boldsymbol{m}_\nu, \Delta_\nu). \tag{13}$$

Here "←" denotes drawing a sample from the distribution on the right-hand side. After some burn-in period, the theory of Gibbs sampling guarantees that the joint set of parameters is indeed drawn from the correct joint distribution. For a full description of the various steps in the algorithm, see Eriksen et al. (2008).

While no fully functional alternatives to Gibbs sampling have been established for this full joint distribution to date, Gibbs sampling alone by no means solves all computational problems. In particular, this algorithm is notorious for its slow convergence for nearly degenerate parameters, since it by construction only moves through parameter space parallel to coordinate axes. For this reason, we implement an additional posterior maximization phase, in which we search directly for the posterior maximum point rather than attempt to sample from the full distribution. The resulting solution may then serve either as a final product in its own right, by virtue of being a maximum-posterior estimate, or as the starting position for a regular Gibbs sampling analysis. The crucial point, though, is that special-purpose nonlinear

search algorithms can be used in this phase, moving in arbitrary directions through parameter space, and individual optimization combinations may be introduced to jointly probe directions with particularly strong degeneracies. Perhaps the single most important example in this respect is the parameter combination between component amplitudes, detector calibrations, and bandpass uncertainties, $\{\boldsymbol{a}_i, g_\nu, \Delta_\nu\}$, all three of which essentially correspond to scaling parameters. However, since both g_ν and $\boldsymbol{a}_i$ are conditionally linear parameters, and only Δ_ν is truly nonlinear, it is possible to solve analytically for g_ν or $\boldsymbol{a}_i$, *conditioning* on any given fixed value of Δ_ν. Consequently, one can set up a nonlinear Powell-type search (Press et al. 2002) for Δ_ν, in which the optimal values of either g_ν or $\boldsymbol{a}_i$ are quickly computed at each iteration in the search. A second example is the electron temperature discussed above, for which non-local optimization is feasible, whereas a full-blown sampling algorithm is too expensive to converge robustly. In this situation, fixing the parameter at its maximum-posterior value is vastly preferable compared to adding an unconverged degree of freedom in the full sampler.

Even with this optimization phase, however, there is always an inherent danger of the algorithm being trapped in a local posterior maximum. Indeed, with a distribution involving millions of highly correlated parameters, it is exceedingly difficult to prove that the derived solution is the true global posterior maximum. As a partial solution to this problem, we initialize the search using different starting positions, and carefully monitor the convergence properties of the chains.

3. Data selection and processing

The primary data used in this paper are the 2015 *Planck* temperature and polarization sky maps (Planck Collaboration VI 2016; Planck Collaboration VIII 2016). For the temperature analysis we additionally include the 9-yr WMAP observations[2] (Bennett et al. 2013) and a full-sky 408 MHz survey map (Haslam et al. 1982), with the goal of individually resolving synchrotron, free-free, and spinning dust emission. For WMAP, we adopt the beam-symmetrized frequency maps for the foreground-dominated *K*- and *Ka*-bands, to mitigate beam artifacts around compact sources, but we use the standard maps for the CMB-dominated *Q*-, *V*-, and *W*-bands, because of their more accurate noise description. At the lowest frequency, we adopt the destriped version of the 408 MHz survey map recently published by Remazeilles et al. (2015).

In order to maximize our leverage with respect to bandpass measurement uncertainties and line emission mechanisms, we employ individual detector and detector set ("ds") maps for all *Planck* frequencies between 70 and 857 GHz, and differencing assembly ("DA") maps for WMAP. However, the polarization analysis employs frequency maps in order to maximize signal-to-noise ratio and to minimize correlated noise from destriper mapmaking uncertainties. Intensity-to-polarization leakage from bandpass mismatch between detectors is suppressed through the use of precomputed leakage templates (Planck Collaboration II 2016; Planck Collaboration VIII 2016). For LFI, these templates are based on a preliminary version of the foreground products presented in this paper. The full set of clean channels used in this analysis is summarized in Table 1 in terms of centre frequencies, resolution, and noise levels. In total, 32 individual detector and detector set maps[3] and frequency maps are included in the temperature analysis, and seven frequency maps in the polarization analysis.

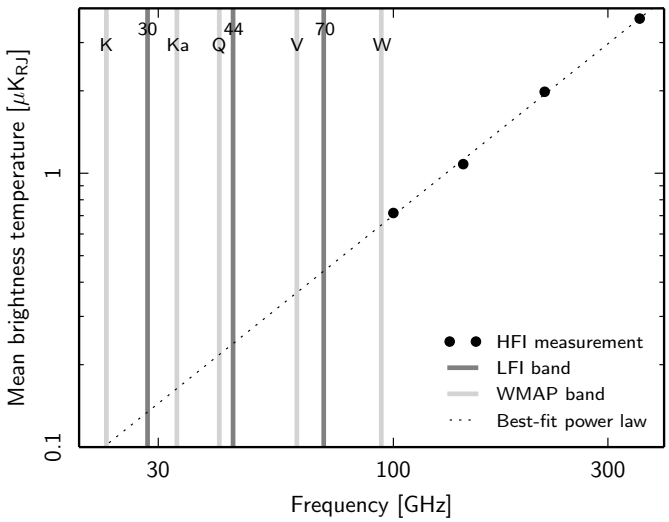

Fig. 1. Zodiacal light extrapolation from HFI to LFI and WMAP frequency channels in terms of full-sky mean brightness temperature. The dotted line shows the power-law fit to the HFI observations between 100 and 353 GHz, $s(\nu) = 0.70\,\mu K_{RJ}\,(\nu/100\,\mathrm{GHz})^{1.31}$, and the vertical grey lines indicate the central frequencies of the LFI and WMAP frequency bands.

For the *Planck* HFI channels, a model of zodiacal light emission is subtracted from the time-ordered data prior to mapmaking (Planck Collaboration VIII 2016). In addition, in this paper we apply a small correction to the low-frequency LFI and WMAP channels by scaling the effective HFI 100 GHz zodiacal light correction map (i.e., uncorrected minus corrected map) to each frequency according to a power law fitted to frequencies between 100 and 353 GHz (Planck Collaboration XIV 2014), as illustrated in Fig. 1; the actual template amplitudes relative to the 100 GHz correction map (in thermodynamic units) are listed in Table 2. Although the magnitude of this correction is small, with a maximum amplitude of 2 μK in the 70 GHz map, applying no correction at all below 100 GHz results in a visually noticeable bias in the derived CO $J = 1 \rightarrow 0$ map at high Galactic latitudes, in the characteristic form of the zodiacal light. Extending the zodiacal light model to low frequencies efficiently eliminates this structure.

In our 2013 release, colour corrections and unit conversions for all *Planck* channels were based on individual bandpass profiles as measured on the ground before launch (Planck Collaboration V 2014; Planck Collaboration IX 2014). However, as discussed in detail in Sects. 2, 4.3, and 5, during the component separation process we find that systematic uncertainties in the nominal bandpasses induce significant residuals between data and model, and it is necessary to fit for these bandpass uncertainties in order to obtain statistically acceptable fits. For WMAP, we adopt the nominal bandpasses[4] for the first DA within each frequency band, and fit for the remaining DA bandpasses within each frequency. For the 408 MHz survey, we adopt a delta function response at the nominal frequency. The unit conversion factors between thermodynamic and brightness

[2] http://lambda.gsfc.nasa.gov

[3] For uniformity, we refer to the 70 GHz horn pair maps as "detector set" maps in this paper, with the {ds1, ds2, ds3} maps corresponding to horns {18+23, 19+22, 20+21}, respectively.

[4] As described by Bennett et al. (2013), the WMAP bandpasses evolved during the 9 yr of WMAP observations, resulting in slightly lower effective full-mission frequencies as compared to the nominal bandpasses. We correct for these small shifts in the present analysis by shifting the bandpasses accordingly.

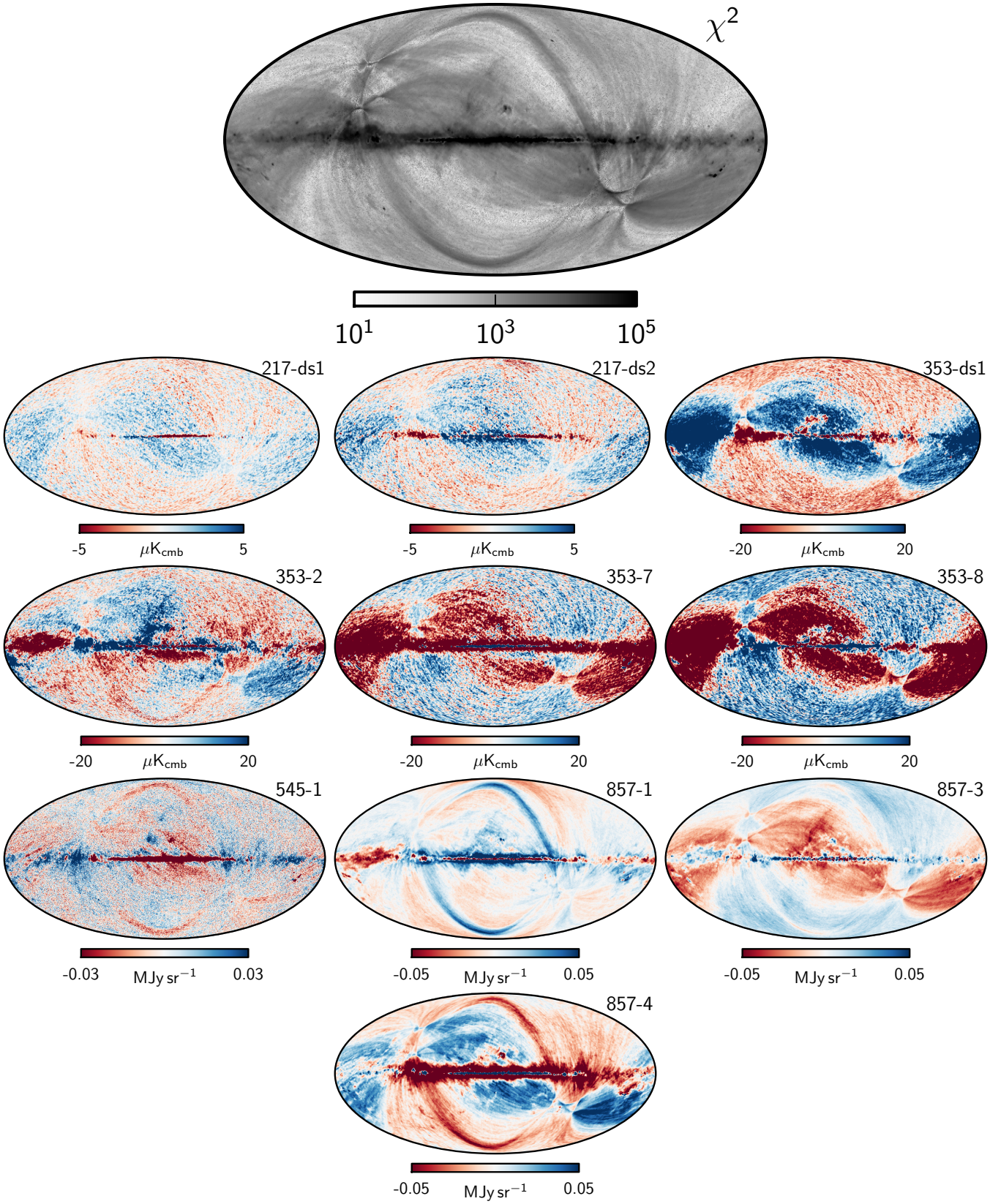

Fig. 2. χ^2 (*top*) and residual maps, $\boldsymbol{d}_\nu - \boldsymbol{s}_\nu$ (*bottom*), for a `Commander` analysis that includes all *Planck* channel maps. These residual maps correspond to channels that are rejected from the baseline analysis due to instrumental systematics; the labels in the *top left corner* in each panel indicates frequency channels. No regularization noise has been added to the high-frequency channels in this case. The sharp ring-like features at high Galactic latitudes correspond to far sidelobe residuals; the broad features extending between the north and south ecliptic poles correspond to destriping errors; and the Galactic plane features correspond to calibration, bandpass, and modelling residuals. All maps (and all other full-sky plots later in the paper) are shown in Galactic coordinates adopting a Mollweide projection with the Galactic centre ($l = 0°$) located in the centre of each panel.

Table 1. Overview of data sets.

Instrument	Frequency [GHz]	Detector label	Resolution	Noise rms $\sigma^T(1^\circ)$ or $\sigma^P(40')$	Min smooth scale	Units	Reference
Temperature							
Planck LFI	30	(all)	32.′4	2.8	40′	μK	Planck Collaboration VI (2016)
	44	(all)	27.′1	3.0	40′	μK	
	70	ds1	13.′6	3.8	40′	μK	
		ds2	13.′3	4.0	40′	μK	
		ds3	13.′0	4.1	40′	μK	
Planck HFI	100	ds1	9.′7	0.9	40′	μK	Planck Collaboration VIII (2016)
		ds2	9.′7	0.8	40′	μK	
	143	ds1	7.′2	0.7	7.′5	μK	
		ds2	7.′2	0.7	7.′5	μK	
		5	7.′2	0.9	7.′5	μK	
		6	7.′2	1.1	7.′5	μK	
		7	7.′2	1.0	7.′5	μK	
	217	1	5.′0	1.8	7.′5	μK	
		2	5.′0	1.9	7.′5	μK	
		3	5.′0	1.7	7.′5	μK	
		4	5.′0	1.8	7.′5	μK	
	353	ds2	4.′9	4.5	7.′5	μK	
		1	4.′9	3.5	7.′5	μK	
	545	2	4.′7	0.01	7.′5	MJy sr^{-1}	
		4	4.′7	0.01	7.′5	MJy sr^{-1}	
	857	2	4.′4	0.01	7.′5	MJy sr^{-1}	
WMAP	23	K	53′	5.9	60′	μK	Bennett et al. (2013)
	33	Ka	40′	4.3	60′	μK	
	41	Q1	31′	5.3	60′	μK	
		Q2	31′	5.1	60′	μK	
	61	V1	21′	6.4	60′	μK	
		V2	21′	5.5	60′	μK	
	95	W1	13′	8.84	60′	μK	
		W2	13′	10.1	60′	μK	
		W3	13′	10.6	60′	μK	
		W4	13′	10.1	60′	μK	
Haslam et al.	0.408		56′	1.1	60′	K	Haslam et al. (1982), Remazeilles et al. (2015)
Polarization							
Planck LFI	30		32.′4	7.5	40′	μK	Planck Collaboration VI (2016)
	44		27.′1	7.5	40′	μK	
	70		13.′3	4.8	40′	μK	
Planck HFI	100		9.′5	1.3	10′	μK	Planck Collaboration VIII (2016)
	143		7.′2	1.1	10′	μK	
	217		5.′0	1.6	10′	μK	
	353		4.′9	6.9	10′	μK	

Notes. The top section lists all detector and detector set ("ds") maps included in the temperature analysis, and the bottom section lists all frequency maps included in the polarization analysis.

temperatures and flux density per area are tabulated for both nominal and fitted bandpass profiles in Table 3.

Some *Planck* detector maps are affected more strongly by systematic errors than others (Planck Collaboration VIII 2016), and in the following temperature analysis we exclude the worst channels in order not to compromise the overall solution. Out of a total of 31 potential *Planck* detector and detector set maps, 10 are removed from further analysis, while the remaining 21 are listed in Tables 1 and 3. The 10 removed maps are shown in Fig. 2 in the form of a $(\boldsymbol{d}_\nu - \boldsymbol{s}_\nu)$ residual map, where $\boldsymbol{s}_\nu$ is a signal model based on the global and spectral parameters derived in Sect. 5, but with amplitudes re-fitted to all 42 channels. The top panel shows the corresponding χ^2 map, defined as

$$\chi^2(p) = \sum_\nu \left(\frac{\boldsymbol{d}_\nu(p) - \mathbf{s}_\nu(p)}{\sigma_\nu(p)} \right)^2 . \quad (14)$$

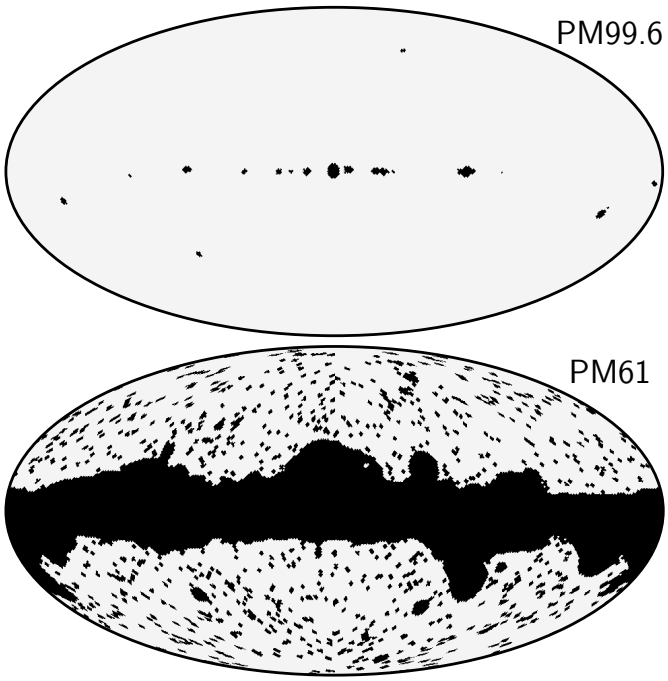

Fig. 3. Processing masks (PM) used in the joint temperature analysis, including 99.6% and 61% of the sky, respectively. The former is used for calibration and bandpass estimation, and the latter for monopole and dipole estimation.

Including any one of these ten maps in the full joint analysis increases the χ^2 of the total fit far beyond what is allowed by random statistical fluctuations.

Several different classes of systematic effects may be seen in these plots. Starting with the 217-ds1 map, we see a large-scale red-blue pattern, aligned with the *Planck* scanning strategy and crossing through the Ecliptic poles (Planck Collaboration I 2014). The same spatial pattern is seen in the 217-ds2, 353-ds1, 353-2, 353-7, 353-8, 857-3, and 857-4 maps as well, with varying amplitudes and signs. These are due to low-amplitude destriping errors induced in the mapmaking process (Planck Collaboration VIII 2016), and only become visually apparent after component separation removes the dominant Galactic signal. These residuals may therefore, at least in principle, be suppressed by iterating between mapmaking and component separation, essentially performing a joint mapmaking/component separation χ^2 fit for the destriping offsets.

A second example of residual systematics is seen in the 857-1 and 857-4 maps, and to a lesser extent in the 545-1 map, in the form of sharp features at high Galactic latitudes. These correspond to far sidelobe (FSL) contamination at the 0.05 MJy sr^{-1} level. Third, and somewhat more subtly, one can see the effect of the very-long time constants (VLTC) discussed in Planck Collaboration VIII (2016), particularly south of the Galactic plane in 353-2, 353-7, and 545-1. In each of these maps, the Galactic plane appears to have been smeared along the scanning direction. As in the case of destriping errors, combining mapmaking and component separation should prove very powerful in suppressing both FSL and VLTC errors in future analyses.

While several channels are omitted from the analysis, it is important to note that the *Planck* HFI temperature observations are strongly signal-dominated at all angular scales above 7′ FWHM. Our data cuts therefore have very little effect on the full error budget, which is dominated by modelling and systematic errors for most parameters. The main cost of these cuts comes in the form of reduced internal redundancy. In particular, having access to only one clean 857 GHz channel limits our ability to determine its bandpass and calibration coefficients. This situation will improve in the next *Planck* data release, when the remaining three 857 GHz channels are better cleaned at the time domain level.

Table 2. Zodiacal light template coefficients for WMAP and LFI frequencies relative to the 100 GHz HFI zodical light template in thermodynamic temperature units.

Band	Amplitude
Planck 30	0.15
44	0.28
70	0.56
WMAP *K*	0.11
Ka	0.19
Q	0.25
V	0.45
W	0.89

The current analysis is carried out in a number of stages according to angular resolution, in which higher-resolution stages implement a simpler foreground model than lower-resolution stages. For temperature, each full-resolution map is downgraded from its native resolution to 1° (all channels), 40′ (all Planck channels), and 7.′5 (HFI channels above 100 GHz) by deconvolving the intrinsic instrumental beam profile and convolving with a Gaussian beam of the appropriate size before repixelizing at `HEALPix`[5] resolutions $N_{\rm side}$ = 256, 256, and 2048, respectively (Górski et al. 2005). For polarization, the corresponding smoothing scales are 40′ and 10′ FWHM, pixelized at $N_{\rm side}$ = 256 and 1024, respectively.

The instrumental noise is assumed to be spatially uncorrelated and Gaussian for all channels, with a spatially-varying rms given by the scanning strategy of the experiment and the instantaneous sensitivity of each detector. The low-resolution noise rms map is found by convolving the high-resolution rms with the appropriate smoothing kernel, properly accounting for its matrix-like nature, and retaining only the diagonal element of the resulting covariance matrix. For the 545 and 857 GHz channels, we additionally add 0.01 MJy sr^{-1} of uniform white noise, to prevent known residual far sidelobe and destriping contamination from propagating to lower frequencies through the thermal dust temperature and spectral index and contaminating both the CMB and CO solutions. Similarly, for the 408 MHz channel we add regularization noise, equal to 1% of the amplitude of the map, to account for low-level residuals not captured by the white noise model described above.

Finally, two different processing masks are employed in the temperature analysis (PM99.6 and PM61), removing 0.4% and 39% of the sky, respectively, as shown in Fig. 3. PM99.6 is generated by thresholding the (smoothed) χ^2 map of a preliminary analysis[6] at 10^4, removing only the very brightest outliers in the data set; this mask is used for bandpass estimation and gain calibration of the 545-4 and 857-2 channels. PM61 is generated as the product of the χ^2 map resulting from an analysis without bandpass corrections thresholded at the 5σ level, and the 9-yr WMAP point source mask. This mask is used for calibration estimation of the CMB frequencies, and for monopole and dipole estimation.

[5] `http://healpix.sourceforge.net/`

[6] The preliminary analysis was similar to the one presented in this paper, but without application of any processing mask for calibration purposes.

Table 3. Unit conversion coefficients between thermodynamic and brightness temperature and between thermodynamic temperature and flux density per unit area for each channel, with and without the bandpass corrections described in Sect. 5.

Instrument	Frequency [GHz]	Detector label	U_c [K_{CMB}/K_{RJ}]			U_c [MJy sr^{-1}/K_{CMB}]		
			Nominal	Fitted	Change [%]	Nominal	Fitted	Change [%]
Planck LFI	30	. . .	1.0212	1.0217	0.1	23.510	24.255	3.2
	44	. . .	1.0515	1.0517	0.0	55.735	56.094	0.6
	70	ds1	1.1378	1.1360	−0.2	132.07	129.77	−1.7
		ds2	1.1361	1.1405	0.4	129.75	135.37	4.3
		ds3	1.1329	1.1348	0.2	126.05	128.57	2.0
Planck HFI	100	ds1	1.3090	1.3058	−0.2	244.59	241.58	−1.2
		ds2	1.3084	1.3057	−0.2	243.77	241.22	−1.1
	143	ds1	1.6663	1.6735	0.4	365.18	368.68	1.0
		ds2	1.6754	1.6727	−0.2	369.29	368.00	−0.4
		5	1.6961	1.6910	−0.3	380.12	377.68	−0.6
		6	1.6829	1.6858	0.2	373.34	374.74	0.4
		7	1.6987	1.6945	−0.2	381.25	379.26	−0.5
	217	1	3.2225	3.2203	−0.1	486.02	485.87	−0.0
		2	3.2378	3.2336	−0.1	486.39	486.10	−0.1
		3	3.2296	3.2329	0.1	486.89	485.85	−0.2
		4	3.2183	3.2161	−0.1	486.01	487.11	0.2
	353	ds2	14.217	14.261	0.3	287.89	287.62	−0.1
		1	14.113	14.106	−0.1	288.41	288.45	0.0
	545	2	164.54	168.94	2.7	58.880	57.953	−1.6
		4	167.60	174.13	3.9	58.056	56.732	−2.3
	857	2	9, 738.8	10, 605.	8.9	2.3449	2.1974	−6.3
WMAP	23	K	1.0134	···	···	14.985	···	···
	33	Ka	1.0284	···	···	31.556	···	···
	41	Q1	1.0437	···	···	47.880	···	···
		Q2	1.0433	1.0439	0.1	47.179	48.226	2.2
	61	V1	1.0974	···	···	97.343	···	···
		V2	1.1006	1.1001	−0.1	101.87	101.20	−0.7
	94	W1	1.2473	···	···	209.61	···	···
		W2	1.2500	1.2458	−0.3	213.65	209.38	−2.0
		W3	1.2440	1.2460	0.1	207.88	209.92	1.0
		W4	1.2488	1.2453	−0.3	211.78	208.18	−1.7
Haslam	0.408	. . .	1.0000	···	···	0.0051	···	···

4. Model survey

Before presenting the results of our analysis, it is useful to review the various model components that are relevant for this work, with the goal of building intuition concerning important degeneracies and residuals that may be observed in various goodness-of-fit statistics. We first review each of the astrophysical sky signal components for both temperature and polarization, as summarized in Table 4 and Fig. 4, and then each of the most important instrumental effects.

4.1. Sky components in intensity

CMB – The CMB is given by a perfect blackbody with only a single spectral parameter, namely the CMB temperature. We adopt a mean value of $T_{cmb} = 2.7255 \pm 0.0006$ K (Fixsen 2009), and notice that the uncertainty in this value is sufficiently small to justify its use as a delta function prior. In the current paper, we neglect both Rayleigh scattering and higher-order relativistic effects (Planck Collaboration XXVII 2014; Lewis 2013); these could be accounted for in future work. The resulting CMB brightness temperature is plotted as a dashed line in each panel of Fig. 4, with an amplitude of 70 μK, corresponding to the CMB rms at 1° FWHM resolution, providing a useful consistent visual reference for other components.

Synchrotron – Diffuse synchrotron emission is generated by relativistic cosmic-ray electrons spiraling in the Galactic magnetic field. This radiation may be highly polarized, with a maximum polarization fraction of 0.75. Both theoretical models and observations suggest that the synchrotron spectrum is well approximated by a power law with an index of $\beta_s \approx -3$ at frequencies above 20 GHz, but with significant flattening at low frequencies. In this paper we adopt a fixed spectral template for the synchrotron spectrum. We use a spectrum extracted from the GALPROP z10LMPD_SUNfE synchrotron model from Orlando & Strong (2013), as described in Planck Collaboration XXV (2016). For brevity we refer to this as the GALPROP model

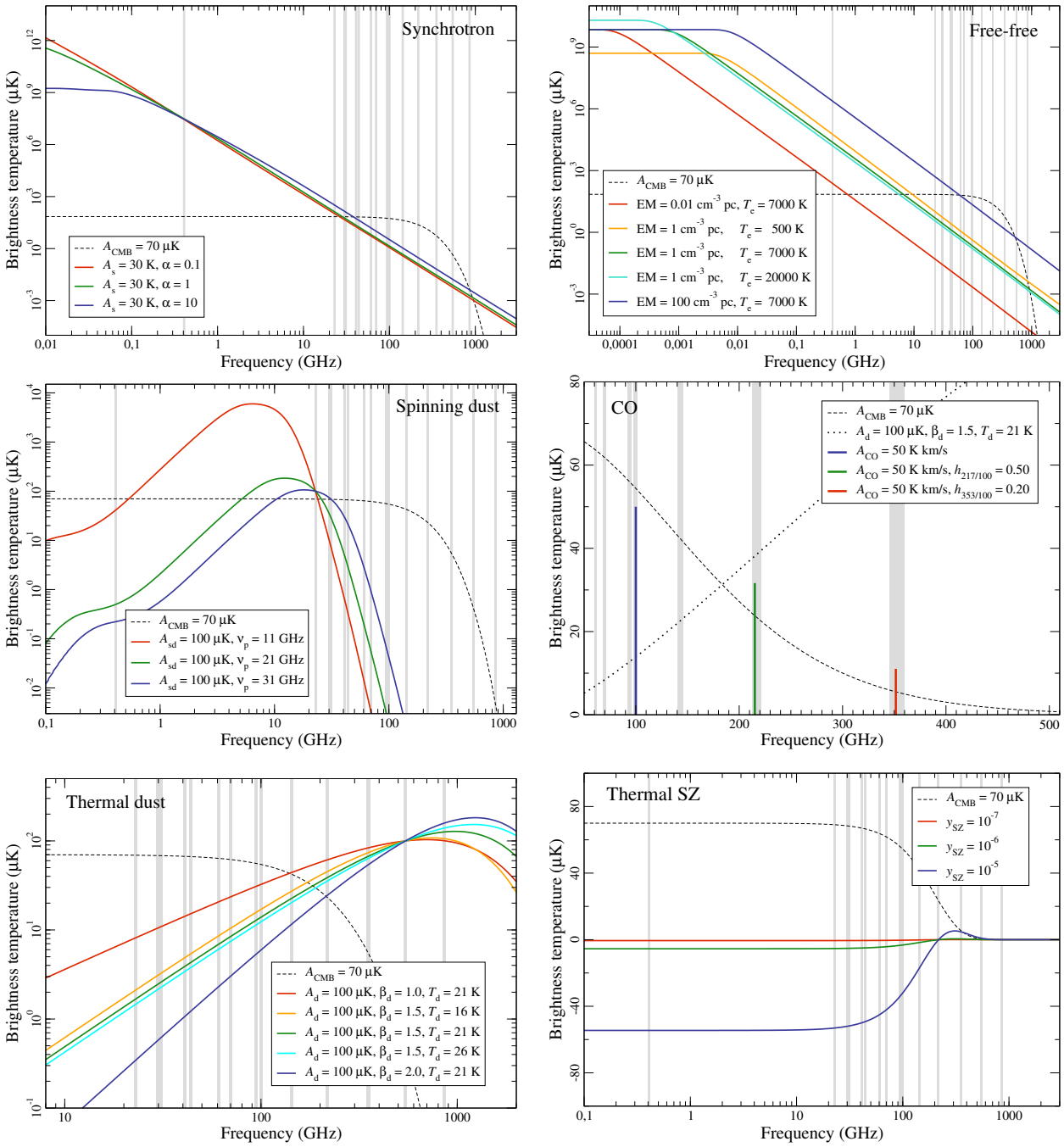

Fig. 4. Spectral energy densities (SEDs) for the main astrophysical components included in the present analysis, in brightness temperature. *From left to right and top to bottom*, panels show: (1) synchrotron emission; (2) free-free emission; (3) spinning dust emission; (4) CO line emission; (5) thermal dust emission; and (6) the thermal Sunyaev-Zeldovich effect. For each case, several parameter combinations are shown to illustrate their effect on the final observable spectrum. Vertical grey bands indicate the centre frequencies of the observations listed in Table 1, but for clarity true bandwidths are suppressed. In each panel, the black dashed line shows the CMB brightness temperature corresponding to a thermodynamic temperature of 70 μK, the CMB rms at 1° FWHM angular scale. In the fourth (CO) panel, the dotted line indicates the SED of thermal dust emission with typical parameter values.

from now on. A description of the GALPROP[7,8] code can be found in Moskalenko & Strong (1998), Strong et al. (2007), Orlando & Strong (2013) and references therein. We allow this spectrum to be rigidly shifted in $\log \nu$–$\log S$ space with a single global frequency shift parameter, α, for the full sky; see Table 4 for the explicit definition. The main effect of such translation, however, is to modify the synchrotron amplitude at 408 MHz, leaving β_s at frequencies above 20 GHz essentially constant and equal to −3.11 for any realistic shift parameter; see Fig. 4. Thus, with the current data the synchrotron amplitude is determined almost exclusively by the 408 MHz survey, while the frequency spectrum is determined by the GALPROP model, with the only free spectral parameter being the relative normalization between the 408 MHz and higher frequency channels. Several

[7] http://galprop.stanford.edu/
[8] https://sourceforge.net/projects/galprop

Table 4. Summary of main parametric signal models for the temperature analysis.

Component	Free parameters and priors	Brightness temperature, s_ν [μK$_{\rm RJ}$]	Additional information
CMB[a]	$A_{\rm cmb} \sim$ Uni$(-\infty, \infty)$	$x = \frac{h\nu}{k_{\rm B}T_{\rm CMB}}$ $g(\nu) = (\exp(x)-1)^2/(x^2\exp(x))$ $s_{\rm CMB} = A_{\rm CMB}/g(\nu)$	$T_{\rm CMB} = 2.7255$ K
Synchrotron[a] . . .	$A_{\rm s} > 0$ $\alpha >$ 0, spatially constant	$s_{\rm s} = A_{\rm s}\left(\frac{\nu_0}{\nu}\right)^2 \frac{f_{\rm s}(\frac{\nu}{\alpha})}{f_{\rm s}(\frac{\nu_0}{\alpha})}$	$\nu_0 = 408$ MHz $f_{\rm s}(\nu) =$ Ext template
Free-free	$\log {\rm EM} \sim$ Uni$(-\infty, \infty)$ $T_{\rm e} \sim N(7000 \pm 500\,{\rm K})$	$g_{\rm ff} = \log\left\{\exp\left[5.960 - \sqrt{3}/\pi \log(\nu_9\ T_4^{-3/2})\right] + e\right\}$ $\tau = 0.05468\ T_{\rm e}^{-3/2}\ \nu_9^{-2}\ {\rm EM}\ g_{\rm ff}$ $s_{\rm ff} = 10^6\, T_{\rm e}\,(1-e^{-\tau})$	$T_4 = T_{\rm e}/10^4$ $\nu_9 = \nu/(10^9\,{\rm Hz})$
Spinning dust . . .	$A^1_{\rm sd}, A^2_{\rm sd} > 0$ $\nu^1_{\rm p} \sim N(19 \pm 3\,{\rm GHz})$ $\nu^2_{\rm p} >$ 0, spatially constant	$s_{\rm sd} = A_{\rm sd} \cdot \left(\frac{\nu_0}{\nu}\right)^2 \frac{f_{\rm sd}(\nu\cdot\nu_{\rm p0}/\nu_{\rm p})}{f_{\rm sd}(\nu_0\cdot\nu_{\rm p0}/\nu_{\rm p})}$	$\nu^1_0 = 22.8$ GHz $\nu^2_0 = 41.0$ GHz $\nu_{\rm p0} = 30.0$ GHz $f_{\rm sd}(\nu) =$ Ext template
Thermal dust[a] . .	$A_{\rm d} > 0$ $\beta_{\rm d} \sim N(1.55 \pm 0.1)$ $T_{\rm d} \sim N(23 \pm 3\,{\rm K})$	$\gamma = \frac{h}{k_{\rm B}T_{\rm d}}$ $s_{\rm d} = A_{\rm d} \cdot \left(\frac{\nu}{\nu_0}\right)^{\beta_{\rm d}+1} \frac{\exp(\gamma\nu_0)-1}{\exp(\gamma\nu)-1}$	$\nu_0 = 545$ GHz
SZ	$y_{\rm sz} > 0$	$s_{\rm sz} = 10^6\, y_{\rm sz}/g(\nu)\, T_{\rm CMB}\left(\frac{x(\exp(x)+1)}{\exp(x)-1} - 4\right)$	
Line emission . .	$A_i > 0$ $h_{ij} >$ 0, spatially constant	$s_i = A_i h_{ij} \frac{F_i(\nu_j)}{F_i(\nu_0)} \frac{g(\nu_0)}{g(\nu_j)}$	$i \in$ { CO $J=1\to0$; CO $J=2\to1$; CO $J=3\to2$; 94/100 } $j =$ detector index $F =$ unit conversion

Notes. For polarization, the same parametric functions are employed, but only CMB, synchrotron, and thermal dust emission are included in the model, with spectral parameters fixed to the result of the temperature analysis. The symbol "$\sim$" implies that the respective parameter has a prior as given by the right-hand side distribution; Uni denotes a uniform distribution within the indicated limits, and N denotes a (normal) Gaussian distribution with the indicated mean and standard devation. [(a)] Polarized component.

alternative models (straight, broken, or logarithmically-curved power laws) were also considered in the preparation of this paper, but we found no statistically robust evidence in favour of any of them over the GALPROP spectrum. With only one very low frequency channel, the current data set contains very little information about the synchrotron spectral index. To constrain the synchrotron component, and break remaining degeneracies between the synchrotron, free-free, and spinning dust components, data from up-coming low-frequency experiments such as S-PASS (2.3 GHz; Carretti et al. 2009), C-BASS (5 GHz; King et al. 2010, 2014), and QUIJOTE (10–40 GHz; Rubiño-Martín et al. 2012) are critically important. For now, we prefer the GALPROP model over various power-law variations, simply because it provides an acceptable fit to the data with essentially no free additional parameters, and that it is based on a well-defined physical model. For further discussion of synchrotron emission in the *Planck* observations, see Planck Collaboration XXV (2016).

Free-free – Free-free emission, or bremsstrahlung, is radiation from electron-ion collisions, and consequently has a frequency spectrum that is well-constrained by physical considerations (Dickinson et al. 2003). We adopt the recent two-parameter model of Draine (2011), in which the free parameters are the (effective beam-averaged) emission measure, EM (i.e., the integrated squared electron density along a line of sight), and the electron temperature, $T_{\rm e}$. As seen in Fig. 4, the spectrum is close to a power law at frequencies above 1 GHz, but exhibits a sharp break at lower frequencies, where the medium becomes optically thick and the brightness temperature becomes equal to the electron temperature. Intuitively, over our frequency range, the EM determines the amplitude of the free-free emission, scaling the spectrum up or down, while the electron temperature changes the effective power law index very slightly, from $\beta = -2.13$ for $T_{\rm e} = 500$ K to $\beta = -2.15$ for $T_{\rm e} = 20\,000$ K. At low frequencies, free-free emission is significantly degenerate with synchrotron emission, but because its power-law index is flatter than for synchrotron, it extends into the high signal-to-noise HFI channels. As a result, it is in fact possible to measure the electron temperature for particularly high signal-to-noise regions of the sky when imposing the smoothness prior discussed in Sect. 2.1. The main difficulty regarding free-free emission lies in a four-way degeneracy between CMB, free-free, spinning dust, and CO emission.

Thermal dust – At frequencies above 100 GHz, the dominant radiation mechanism is thermal dust emission Planck Collaboration XI (2014; Planck Collaboration XIV 2014; Planck Collaboration XVII 2014; Planck Collaboration Int. XIX 2015). The characteristic frequency is determined by the temperature of the dust grains, and therefore varies with dust population and environment. Empirically, thermal dust emission may be accurately described across the *Planck* frequencies as

a modified blackbody with a free emissivity index, β_d, and dust temperature, T_d, per pixel, often referred to as a grey-body, (Planck Collaboration XII 2014; Planck Collaboration Int. XVII 2014). At frequencies above 857 GHz, extending into the *COBE*-DIRBE frequencies (Hauser et al. 1998), the dust physics quickly becomes far more complicated, and the instrumental systematics more difficult to contain, and we therefore restrict our current analysis to frequencies up to 857 GHz. Correspondingly, we emphasize that the model derived here is only expected to be accurate at frequencies up to 857 GHz, and its main application is extrapolation to low, not high, frequencies. However, alternative parametrizations of thermal dust have been suggested in the literature, for instance in terms of a two-component grey-body model (e.g., Finkbeiner et al. 1999; Meisner & Finkbeiner 2015), in which each of the two components has a spatially constant emissivity and temperature. Similar to the alternative synchrotron models mentioned above, we also considered such models in the preparation of this paper. Without higher-frequency observations we found that the data are not able to discriminate between the various scenarios at any statistically significant level. For simplicity, we therefore adopt the one-component greybody model with a varying spectral index as a phenomenological parametric thermal dust model, noting that it provides a highly efficient representation of the true sky for frequencies up to 857 GHz, with no additional free global parameters. Finally, we point out that cosmic infrared background fluctuations (CIB) is interpreted as thermal dust emission in our model, by virtue of having a frequency spectrum similar to a greybody component (Planck Collaboration XXX 2014). However, because CIB is relatively weak compared to the Galactic signal, this is only a significant issue in low-foreground regions of the sky.

Spinning dust – Dust grains not only vibrate, but they can also rotate. If they have a non-zero electric dipole moment, this rotation will necessarily lead to microwave emission, as first demonstrated by Erickson (1957) and, in detail, by Draine & Lazarian (1998). The first hints of such radiation in real data were found by cross-correlating CMB data with far-IR observations (Kogut et al. 1996; de Oliveira-Costa et al. 1997; Netterfield et al. 1997), but at the time this correlation was thought to be dominated by free-free emission, coupled to dust due to star formation. The first identification of a new anomalous component was made by Leitch et al. (1997), and the observed excess emission was simply referred to as "anomalous microwave emission", in order not to make premature conclusions regarding its physical nature. However, recent observational progress has made the physical association much more firm (e.g., Davies et al. 2006; Planck Collaboration XX 2011; Gold et al. 2011; Planck Collaboration XXI 2011; Bennett et al. 2013; Planck Collaboration Int. XV 2014, and references theirin) and we refer to this component simply as spinning dust. We adopt a spinning dust spectral template as our spectral model, as evaluated for a cold neutral medium with `SpDust2` (Ali-Haïmoud et al. 2009; Ali-Haïmoud 2010; Silsbee et al. 2011). To fit this template to the data, we introduce a free peak frequency, ν_p, and allow rigid translations the $\log\nu$–$\log S$ space. As explicitly demonstrated by Bennett et al. (2013), this simple two-parameter model can accommodate a large number of spinning dust model variations to high precision.

To facilitate comparison with previously reported results, we report the peak frequency for a spinning dust spectrum defined in flux density units, and note that the conversion between brightness temperature and flux density is $\propto\lambda^{-2}$; see Table 4. The exact value of ν_p is highly uncertain, and depends on the physical properties of the dust grains, but is typically found to lie between 20 and 30 GHz from dedicated observations of individual objects (Planck Collaboration XX 2011), in some objects reaching as high as ≈50 GHz (Planck Collaboration Int. XV 2014). The exact shape of the spectrum is also uncertain, but we have been unable to fit this component with a single `spdust` component, always finding significant residuals with dust-like morphology at 20–30 GHz when forcing a high prior on ν_p, or at 40–70 GHz when forcing a low prior. For now, therefore, we adopt a two-component spinning dust model in which one component has a free peak frequency, ν_p, per pixel and the other component has a free, but spatially constant, ν_{p2}, for a total of three free spinning dust parameters per pixel and one global parameter. We emphasize that this is a purely phenomenological model, and we attach no physical reality to it. The second component is in effect only a computationally convenient parameterization of the width of the spinning dust peak (see Fig. 4). We therefore show only the sum of the two spinning dust components in the following, evaluated at 30 GHz. However, the set of released foreground data products includes the individual component parameters, allowing external uses to reproduce all results.

As listed in Table 4, we adopt a Gaussian prior of $N(19\,\mathrm{GHz} \pm 3\,\mathrm{GHz})$ on the peak frequency of the primary spinning dust component, while no informative prior is enforced on the spatially uniform secondary component. At first sight, the former prior might look discrepant with respect to other targeted studies of spinning dust, which often report best-fit peak frequencies between 25 and 30 GHz. However, when adding the two spinning dust components, one with $\nu_p \approx 20$ GHz and another with $\nu_p \approx 33$ GHz, the total is indeed a component with a peak frequency around 25 GHz.

Finally, we emphasize that the spinning dust component exhibits significant correlations with both synchrotron and free-free emission, and its individual parameters are sensitive to both instrumental bandpasses and calibration. Thus, the reported parametric best-fit values are associated with large correlated systematic uncertainties, and additional low-frequency observations are required to make the spinning dust model robust. As already mentioned, low-frequency observations from experiments like S-PASS, C-BASS, and QUIJOTE are critically needed to break these degeneracies.

CO and 94/100 GHz line emission – As reported in Planck Collaboration XIII (2014), line emission from carbon monoxide (CO) is strongly detected in the *Planck* 100, 217, and 353 GHz frequency channels, and two sets of individual CO $J = 1 \rightarrow 0$, $2 \rightarrow 1$, and $3 \rightarrow 2$ line maps (so-called "Type-1" and "Type-2" maps, produced by the `MILCA` and `Commander` algorithms, respectively) as well as a frequency co-added line map ("Type-3", also produced with `Commander`) were provided in the 2013 *Planck* data release. In Sect. 5.5.3 we present updated CO maps, based on the full *Planck* mission data set, plus a new general line emission map, which captures a combination of emission lines that are detected with the HFI 100 GHz and WMAP *W* bands. An important contributor to this map is the HCN line at 88.6 GHz, providing about 23% (63%) of the 100 GHz (*W*-band) amplitude towards the Galactic circumnuclear disk (GCD) and Sgr A* (Takekawa et al. 2014). Several other lines (CN, HCO+, CS, etc.) contribute at a level of 5–10% each. In addition, since we account for neither velocity effects nor detailed cloud physics (opacity, local thermal equilibrium state, etc.), there is also a non-negligible amount of CO leakage in this new map. We therefore refer to the new component simply as "94/100 GHz line emission".

Generally speaking, the fact allowing us to separate line emission from other diffuse components is that the bandpass filters of individual detectors have different transmission levels at the line frequency. Therefore, while components with continuous spectra very nearly vanish in detector difference maps within single frequencies, line emission does not. For this reason, we employ individual detector maps in the 2015 temperature analysis, as opposed to co-added frequency maps in the corresponding 2013 analysis. However, for the highest resolution maps, for which neither LFI nor WMAP are able to provide useful information, there is a strong degeneracy between CMB, free-free, and CO $J = 1 \rightarrow 0$ emission. The high-resolution CO maps are therefore produced with dedicated and special-purpose methods, as described in Sect. 5.5.3. Furthermore, the CO $J = 3 \rightarrow 2$ emission map is significantly degenerate with the brighter thermal dust component, and consequently subject to large systematic uncertainties.

We describe the line emission maps parametrically in terms of an amplitude map at the line frequency, $a(p)$, normalized relative to one specific detector map, and with a rigid frequency scaling given by the product of a spatially constant line ratio, h_{ij}, where i corresponds to a spectral line index, and j denotes detector index. $F(\nu)$ denotes some unit conversion factor, converting for example between μK_{RJ} and $K_{RJ}\,km\,s^{-1}$ (see Table 4 for the exact mathematical definition). The same formalism applies whether h_{ij} refers to line ratios between frequencies or only to bandpass ratios within frequencies. For example, in 2013 this formalism was used to construct the so-called CO Type-3 map (Planck Collaboration XIII 2014), which is defined by assuming spatially constant CO $J = 2 \rightarrow 1/J = 1 \rightarrow 0$ and $J = 3 \rightarrow 2/J = 1 \rightarrow 0$ line ratios. In the current analysis, we only assume that the same approximation holds between detectors within single frequencies, i.e., that the ratio between the CO signals observed by the 100-ds1 and 100-ds2 detectors is spatially constant. These assumptions are not strictly correct in either case, both because of real variations in local physical properties such as opacity and temperature, and because of non-zero velocities of molecular clouds that either red- or blueshift the intrinsic line frequency. Since the derivative of the bandpass profile evaluated at the line frequency also varies between detectors, the effective observed line ratio along a given line of sight also varies on the sky. As we shall see in Sect. 5, this effect represents the dominant residual systematic in a few of our frequency channels after component separation.

Thermal Sunyaev-Zeldovich – The last of the main astrophysical components included in the following temperature analysis is the thermal Sunyaev-Zeldovich (SZ) effect, which is caused by CMB photons scattering off hot electrons in clusters (Sunyaev & Zeldovich 1972). After such scattering, the effective spectrum no longer follows a perfect blackbody, but is rather given by the expression[9] listed in Table 4. The only free parameter for this effect is the Compton parameter, y_{sz}, which for our purposes acts as a simple amplitude parameter. We note that the effective SZ spectrum is negative below 217 GHz and positive above this frequency, and this feature provides a unique observational signature. Still, the effect is weak for all but the very brightest clusters on the sky, and the y_{sz} map is therefore particularly sensitive to both modelling and systematic errors. In this paper, we only fit for the thermal SZ effect in two separate regions around the Coma and Virgo clusters, which are by far the two strongest SZ objects on the sky, in order to prevent these from contaminating the other components. While the SZ decrement for the Coma cluster is as large as $-400\,\mu$K below 100 GHz on an angular scale of a few arcminutes (Battistelli et al. 2003; Planck Collaboration Int. X 2013), and for the Virgo cluster a few tens of microkelvin on a few degrees scale (Diego & Ascasibar 2008), it is only a few microkelvin for most other objects after convolution with the large beams considered in this paper. Further, full-sky SZ reconstruction within the present global analysis framework requires significantly better control of systematic effects than what is achieved in the current analysis, in particular at high frequencies. For dedicated full-sky SZ reconstruction, see Planck Collaboration XXI (2014) and Planck Collaboration XXII (2016).

Monopoles and dipoles – In addition to the above astrophysical components, the microwave sky exhibits important signal contributions in the form of monopoles and dipoles. The prime monopole examples are the CMB monopole of 2.7255 K and the average CIB amplitude (Planck Collaboration XXX 2014). The main dipole contribution also comes from the CMB, which has an amplitude of 3.3655 (3.3640) K as measured by LFI (HFI). The difference between the LFI and HFI measurements of $1.5\,\mu$K is within quoted uncertainties (Planck Collaboration I 2016).

Ideally, the CMB dipole contribution should be removed during map making (Planck Collaboration VI 2016; Planck Collaboration VIII 2016), but because the estimated dipole has a non-zero uncertainty, and different dipoles are subtracted from the *Planck* and WMAP sky maps, it is necessary to account for residual dipoles in each individual map. In this paper, we adopt as delta function priors the nominal *Planck* dipole estimates for a small subset of reference frequencies (namely the 30, 100-ds1, 143-ds1, 545, and 857 channels), as well as the parameters derived by Wehus et al. (2016) for the 408 MHz map. That is, the dipoles of these six channels are fixed at their nominal values, and, together, they anchor the dipole solutions for all astrophysical component maps.

Likewise, we adopt the nominal monopole parameters for a subset of frequency channels, anchoring the effective offsets of each component to external values. Specifically, we adopt the HFI CIB monopole predictions, as listed in Table 5 of Planck Collaboration VIII (2016), for the 100-ds1, 143-ds1 and 545-2 monopoles, and the zero-points derived by Wehus et al. (2016) for the WMAP Ka and 408 MHz bands.

Thus the following analysis does not derive independent absolute estimates for either monopoles or dipoles, but relies critically on external priors for these values. If, say, the CIB monopole prediction is significantly updated through additional observations, this error will translate directly into an error in the zero level of our thermal dust map. On the other hand, our analysis does provide an independent internal consistency check among the adopted priors, and, as we shall see, no major anomalies are found.

Other components – Finally, we mention briefly some other subdominant effects that are either neglected or only indirectly accounted for in our model. First, similar to the thermal SZ effect, the kinetic Sunyaev-Zeldovich effect is caused by CMB photons scattering on hot electrons (e.g., Rephaeli 1995; Planck Collaboration XXII 2016, and references therein). However, in this case a non-zero bulk velocity in the electron population is the defining feature. When interacting with moving electrons, the photons effectively receive a Doppler shift proportional to the bulk velocity. In this process, the CMB blackbody spectrum is conserved, but its temperature is slightly changed. The kSZ effect is therefore fully degenerate with the primordial CMB

[9] For simplicity, we adopt the non-relativistic expression for the thermal SZ effect in this paper.

anisotropies when considered pixel-by-pixel, and can only be disentangled using spatial information and cross-correlations. However, this effect is small, and we neglect it in the rest of the paper.

Second, the cosmic infrared background Planck Collaboration XVIII (2011; Planck Collaboration XXX 2014) consists of redshifted thermal dust radiation from distant galaxies. By virtue of being a cosmological signal, it is statistically isotropic in the sky, and can therefore be described analogously to the CMB in terms of a sum of a constant offset at each frequency plus small fluctuations imprinted on top, tracing the column density of the emitting matter integrated over redshift. In this paper, we account for the mean temperature through the monopole parameter of each frequency map, but neglect the spatially varying component. Since the CIB frequency spectrum is very similar to the Galactic thermal dust spectrum, with typical mean greybody parameters of $\beta_{\rm CIB} = 1.4 \pm 0.2$ and $T_{\rm CIB} = (13.6 \pm 1.5)$ K (Gispert et al. 2000), these fluctuations are effectively absorbed by our thermal dust model. Future work will attempt to break this degeneracy by exploiting the different spatial power spectra of the two components, and through the use of external priors.

Third, there has been some discussion in the literature concerning the existence of magnetic dipole emission from dust grains (Draine & Lazarian 1999; Draine & Hensley 2013), with tentative evidence reported in Planck Collaboration Int. XXII (2015). Suggestions have even been made that such emission might contaminate previously published CMB maps at significant levels (Liu et al. 2014). Planck Collaboration XXV (2016) comments briefly on this question, while in this paper we simply observe that the current model is able to reproduce the data with statistically acceptable accuracy without such a component, and it is neglected in the following baseline analysis.

Fourth and finally, extra-Galactic point sources contribute significant power at both low and high frequencies (Planck Collaboration XXV 2016). In the following analysis, in which we fit for foreground parameters pixel-by-pixel, these sources end up in the component map with the most similar frequency spectrum, for instance the free-free or thermal dust emission maps. In an attempt to minimize such contamination, we pre-processed each input map by subtracting catalogues of known resolved sources (Bennett et al. 2013; Planck Collaboration XXVIII 2014) before performing the analysis. However, due to source variability, beam asymmetries, and uncertainties in the actual catalogues, we invariably found worse results with such pre-processing. A more promising approach is to fit for each source jointly with the diffuse components, as for instance described by Bull et al. (2015). This, however, is left for future work.

4.2. Sky components in polarization

Whereas the microwave sky in total intensity exhibits very rich astrophysics, in principle requiring between 10 and 20 different physical components for a proper model (depending on the level of detail required), the same is not true for polarization. At the sensitivity level of current experiments, only three diffuse components have been clearly detected, namely CMB, synchrotron, and thermal dust.

CMB – Thomson scattering between electrons and photons is an intrinsically polarized process. If the incident radiation surrounding a given electron is fully isotropic, no net polarization will be observed from that electron. However, if the radiation forms a local quadrupole, a net non-zero CMB polarization signal results (Zaldarriaga & Seljak 1997; Kamionkowski et al. 1997; Hu & White 1997). Thus, any process that generates quadrupolar structures at the time of recombination or during the epoch of reionization will result in a CMB polarization signal. The scalar fluctuations that are responsible for creating the CMB temperature anisotropies will form so-called "*E*-mode" patterns, in which the polarization direction is either orthogonal or parallel to the wave direction. Inflationary gravitational waves and weak gravitational lensing of CMB *E*-modes produce so-called "*B*-mode" patterns, in which the polarization direction is rotated −45° or +45° with respect to the wave direction. These two are the only known sources of such *B*-modes of primordial or high redshift origin.

Synchrotron – Radiation emitted from relativistic electrons spiraling in a magnetic field is intrinsically highly polarized, with about seven times more energy being emitted in the plane of the electron's motion than in the orthogonal direction. For a perfectly regular magnetic field, the synchrotron polarization fraction may exceed 70% (Pacholczyk 1970), although for realistic fields it is usually significantly less. WMAP found a polarization fraction of about 3% in the Galactic plane and about 20% at high Galactic latitudes (Page et al. 2007). Other analyses report polarization fractions as high as 50% on large angular scales (Kogut et al. 2007; Vidal et al. 2015). The new *Planck* measurements at 30 and 44 GHz complement these observations, and allow us to put independent constraints on this quantity (Planck Collaboration XXV 2016).

Thermal dust – Magnetic fields also have an important effect on aspherical dust grains, in the sense that they tend to align the grains' major axes with the local magnetic field direction. This alignment naturally results in net microwave polarization with a thermal dust spectrum. Furthermore, with the frequency coverage and sensitivity of the HFI channels, *Planck*is ideally suited to measure this signal with very high accuracy, as has already been demonstrated through a series of recent papers, including Planck Collaboration Int. XIX (2015), Planck Collaboration Int. XX (2015), Planck Collaboration Int. XXI (2015), Planck Collaboration Int. XXII (2015), and Planck Collaboration Int. XXX (2016). One important goal of the current paper is to provide direct access to these observations in a computationally convenient form.

Neglected components – Considering the other components that are relevant for intensity analysis, we first note that the free-free emission process is intrinsically independent of direction, and therefore naturally unpolarized, although some polarization may arise due to Thomson scattering on electrons near the edges of strong H II regions. This effect, however, is smaller than 10% for edges of optically thick clouds (Keating et al. 1998), and negligible away from any sharp edges. Averaged over the full sky, free-free emission is observationally constrained to be less than 1% polarized (Macellari et al. 2011).

Next, spinning dust emission is generated by small dust grains, and these generally align weakly with the local magnetic field. However, rotational energy level splitting dissipates energy, and this leads to a low level of grain alignment (Lazarian & Draine 2000). As a result, the polarization fraction may be up to 1–3% between 10 and 30 GHz, but falling to less than 1% at higher frequencies. For a recent review of current constraints, see Rubiño-Martín et al. (2012).

Third, polarized CO emission was first detected by Greaves et al. (1999) at the roughly 1% level near the Galactic centre

and in molecular clouds. This signal may therefore in principle be detected in the very sensitive *Planck* 100 and 217 GHz frequency channels. However, as described in Planck Collaboration VIII (2016), one of the most important systematic effects in the *Planck* polarization data set is temperature-to-polarization leakage, one component of which is precisely leakage of the CO signal. For now, therefore, we conservatively mask any regions with strong CO intensity detections from all polarization maps (see Sect. 6 for further discussion). This issue will be revisited in the future.

Contributions from the CIB, extragalactic point sources (Tucci & Toffolatti 2012), the Sunyaev-Zeldovich effect, etc., are all small compared to the noise level of *Planck*, and neglected in the following.

4.3. Instrumental effects

In addition to astrophysical components, our model includes two important instrumental effects, relative calibration between detectors and bandpass uncertainties.

Relative calibration – A calibration error scales a map up or down in amplitude, affecting all components equally. For astrophysical foregrounds, such errors are therefore strongly degenerate with spectral indices. The CMB, however, is a nearly perfect blackbody across the relevant frequency range, and provides a powerful relative calibration source. In the following, we (arbitrarily) adopt the 143-ds1 channel as our absolute calibration reference. For any channel between 30 and 353 GHz, we then use CMB fluctuations between multipoles $\ell_{\rm min} = 25$ and 100 to determine the relative calibration by means of a simple cross-correlation,

$$\boldsymbol{g}_i = \frac{1}{76}\sum_{\ell=25}^{100}\frac{\sum_{m=-\ell}^{\ell}|a^i_{\ell m}(a^{\rm cmb}_{\ell m})^*|}{\sum_{m=-\ell}^{\ell}|a^{\rm cmb}_{\ell m}|^2}, \quad (15)$$

where $\boldsymbol{s}_{\rm cmb} = \sum_{\ell,m} a_{\ell m} Y_{\ell m}$ is the usual spherical harmonic transform. This equation effectively replaces Eq. (10) in the Gibbs sampling chain for the relevant channels. The cross-correlation coefficient is evaluated over pixels admitted by the PM61 processing mask (Fig. 3), and the multipole range $25 \leq \ell \leq 100$ is choosen to minimize contamination from diffuse foregrounds on the low end and confusion with beam uncertainties on the high end.

Strictly speaking, this estimation step is a violation of the Gibbs sampling algorithm as defined in Eq. (10), since that formally should include all signal components over the full sky, not just the CMB component evaluated over parts of the sky. However, in this special case we trade mathematical rigour for the sake of increased robustness with respect to systematic effects.

The 545 and 857 GHz channels are treated as special cases. As discussed in Sect. 3, these channels are significantly affected by far sidelobe and destriping error contamination. We therefore exclude the 545-1, 857-1, 857-3, and 857-4 channels entirely, and add white regularization noise of 0.01 MJy sr^{-1} to the remaining channels. Unfortunately, this noise addition has the side-effect that any CMB fluctuations at 545 GHz are obscured by random white noise, to the extent that it is no longer possible to calibrate the 545 GHz channel with CMB fluctuations within the usual Gibbs chain. As a partial solution to this problem, we perform a dedicated pre-analysis that is identical to the main analysis, except that no regularization noise is added to the high-frequency channels. The 545-2 calibration is then fixed at the resulting value in the subsequent main analysis, while the other 545-4 and 857-2 calibrations are fitted using the full Gibbs expression, including full-sky (up to the PM99.6 processing mask) and all-component observations. We estimate that the uncertainty on the 545-1 recalibration factor derived in this paper is 1–2%, which translates into a 3–6% uncertainty on the 857 GHz calibration through the thermal dust scaling. Note, however, that the 857 GHz calibration is almost perfectly correlated with the 545 GHz calibration. These two values represent the most significant sources of systematic error in the entire temperature analysis.

Finally, the calibration of the two lowest frequencies (408 MHz and WMAP K-band) are fixed to their nominal values. The estimated calibration uncertainty of the 408 MHz channel is 10% (Haslam et al. 1982), and as a result our synchrotron model also has a 10% calibration uncertainty. We note that the 408 MHz calibration is almost perfectly degenerate with the GALPROP scale frequency, $\nu^{\rm s}_{\rm p}$, a degeneracy that is only partially broken by the presence of free-free emission. For the WMAP K-band, the main problem lies in the considerable model uncertainty of the spinning dust component, which prevents an effective CMB cross-correlation at the required sub-percent accuracy level. For now, we consider the default CMB dipole-based K-band calibration to be more robust than a CMB cross-correlation-based estimate.

Bandpass errors – The bandpass profile of a detector provides the information required to convert between a given foreground spectrum and the actually measured signal, both in terms of unit conversion and effective colour corrections (Planck Collaboration V 2014; Planck Collaboration IX 2014). Therefore, a measurement error in the bandpass profile essentially translates into a spectral-index-dependent multiplicative scale error. As such, bandpass measurement errors are almost perfectly degenerate with calibration errors, except in one crucial aspect. For maps that are calibrated on the CMB dipole, the amplitude of the CMB fluctuations is fully independent of any bandpass assumptions. This fact holds the key to separating bandpass from calibration effects. While calibration errors affect both foreground and CMB components equally, bandpass measurement errors only affect foreground components.

As shown in the following, bandpass measurement uncertainties are important for both LFI and HFI in high-precision component separation. Figure 5 provides a simple illustration of this, in the form of the fractional difference between the 143-ds1 and 143-ds2 detector maps,

$$r = \frac{d^{\rm 143ds\text{-}1} - d^{\rm 143ds\text{-}2}}{d^{\rm 143ds\text{-}1}}. \quad (16)$$

The top panel shows the fractional difference map computed from the observed *Planck* 2015 data and smoothed to 40′ FWHM, and the bottom panel shows the same from the 2015 FFP8 simulation (Planck Collaboration XII 2016), which is based on the nominal bandpass profiles. The effective frequencies for these two channels, based on laboratory measurements, are listed in Table 4 of Planck Collaboration IX (2014), and are (144.22 ± 0.02) and (145.05 ± 0.02) GHz for a spectral index of $\alpha = 2$. The nominal 143-ds2 effective frequency is therefore 0.8 GHz higher than the corresponding 143-ds1 effective frequency, and this holds almost independently of the assumed spectral index. Given these numbers, and recognizing that the 143 GHz channel is dominated by thermal dust, which has an effective spectral index of $\beta \approx 1.4$ at this frequency, one would expect the above fractional ratio to be

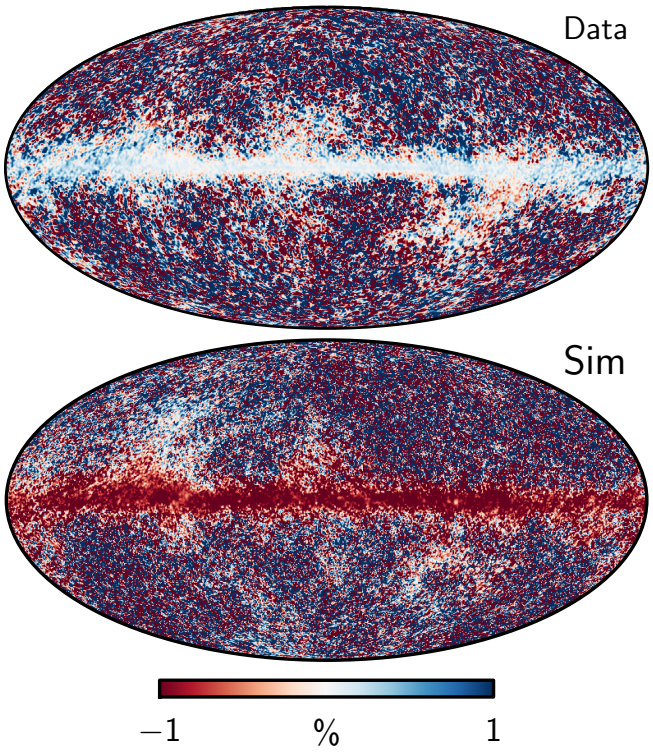

Fig. 5. Fractional 143 GHz difference maps on the form $(\boldsymbol{d}_{\text{143-ds1}} - \boldsymbol{d}_{\text{143-ds2}})/\boldsymbol{d}_{\text{143-ds1}}$, as evaluated from the real data (*top*) and from the FFP8 simulation (*bottom*), both smoothed to 40′ FWHM. The 1% difference observed along the Galactic plane is caused by a mismatch between the measured bandpass profiles (which are used to construct the FFP8 simulations) and those corresponding to in-flight observations. See Sect. 4.3 for further discussion, and Sect. 5.3 for explicit corrections.

$(1 - (145.05/144.22)^{1.4}) \approx -0.8\%$, as is indeed observed in the simulation. However, in the real data, we see that the fractional ratio is approximately +0.2%, strongly suggesting that 143-ds1 in fact has a higher effective frequency than 143-ds2, not lower.

An alternative explanation for this discrepancy between the model and the data might be relative calibration errors. However, a 1% relative calibration error in the 143 GHz channel is strongly ruled out by CMB cross-correlations, since the internal relative calibration of this channel is accurate to about 0.1% (see Sect. 5, Planck Collaboration I 2016, and Planck Collaboration VIII 2016). A second possibility is that the 143 GHz channel might be dominated by some other component than thermal dust, such as free-free emission. However, such a hypothesis can only explain the observed difference for one particular detector combination, while similar differences are observed between many detector maps. Furthermore, it does not match the morphology of the observed fractional difference map. The only viable explanation we have found is indeed bandpass errors with magnitudes at the $\lesssim$1 GHz level. It is worth noting that significant discrepancies among the 143 GHz detector bandpasses were noted already in Planck Collaboration IX (2014), and these qualitative findings are therefore not new.

Fortunately, there is sufficient information in the current data to self-consistently constrain and mitigate these errors. First, by employing detector-set maps instead of full-frequency maps, bandpass errors within frequency bands can be constrained with high signal-to-noise levels, as illustrated in Fig. 5. Second, because the true sky contains multiple foreground components with varying spectral indices, while there is only one true bandpass per detector that applies to all components and all pixels on the sky, even the mean bandpass correction per frequency is constrained to some level, although this dependency is conditional on the overall foreground model. Therefore, the bandpass corrections presented in the following are strongly constrained with respect to relative bandpass shifts *within* frequency bands, but uncertain with respect to frequency shifts *across* frequency bands. Intuitively, it is easy to conclude with high significance that the relative difference between the 143-ds1 and 143-ds2 effective frequencies is +0.2 GHz, not −0.8 GHz, but it is difficult to say with confidence whether both should be shifted jointly by an additional 0.2 or −0.2 GHz. That depends on the spectral index of thermal dust emission, and consequently on the 545 and 857 GHz calibration factors, which are still associated with significant uncertainties.

As for an explicit parameterization of the bandpass errors, we adopt in this paper a simple and purely phenomenological model given by a rigid bandpass translation in frequency space:

$$b(\nu) = b_0(\nu + \Delta_\nu). \tag{17}$$

Here $b_0(\nu)$ denotes the nominal bandpass, $b(\nu)$ is the fitted bandpass, and Δ_ν is the effective frequency shift between the two. We emphasize that this is not to be taken as a physical model of the true bandpass errors, and more realistic models should include information specifically regarding the tails of the bandpasses, the separation between main bandpass modes, and overall large-scale tilts, not only centre frequency shifts.

5. Temperature analysis

5.1. Model motivation

Our baseline *Planck* 2015 astrophysical model, derived from a joint analysis of the *Planck*, WMAP, and 408 MHz observations, includes the following components: (1) CMB; (2) synchrotron emission; (3) free-free emission; (4) two spinning dust emission components; (5) CO line emission at 100, 217, and 353 GHz; (6) 94/100 GHz line emission; (7) thermal dust emission; and (8) thermal SZ emission around the Coma and Virgo clusters. In addition, the model includes monopole, dipole, recalibration, and bandpass corrections for each channel.

Many model variations were considered in the preparatory stages of this analysis, including: (1) broken or smoothly-curved synchrotron frequency spectra; (2) free-free models with fixed power-law indices; (3) one-component spinning dust models, based both on physical `SpDust` templates and phenomenological second-order polynomial frequency spectra; (4) two-component thermal dust models; (5) thermal dust models with flattening at low frequencies; (6) Type-3 CO line emission; (7) no 94/100 GHz line emission component; (8) full-sky SZ reconstruction; (9) no bandpass corrections; and (10) various priors for relevant components. It is impossible to fully describe all of these topics within a single paper, and we do not attempt to do so. Some low-frequency model variations are, however, discussed in Planck Collaboration XXV (2016).

In this paper our focus is the baseline model, which is the simplest sufficient model considered to date, as defined in terms of three criteria. First and foremost, the baseline model has to provide a statistically acceptable fit to the observations over the bulk of the sky, including most of the Galactic plane. Second, it should have the smallest possible number of free degrees of freedom that still result in a statistically acceptable fit to the data. Third and finally, in cases where there are free

choices, physically well-motivated models are preferred over phenomenological models.

Three examples illustrate our approach. First, for synchrotron emission we have found that a broken power-law model, i.e., a power-law model with fixed but different spectral indices above and below some break frequency (say, 3 GHz) provides an equally good χ^2 fit as the GALPROP model do. A straight power-law spectrum, on the other hand, does not fit the data, because the 408 MHz map appears dimmer than expected from a straight extrapolation from 23 GHz to 408 MHz, assuming the spectral index of $\beta \approx -3.0$ to -3.2 required to fit higher frequencies. The reasons for preferring the GALPROP model are therefore not data-driven, but rather that it requires less tuning (e.g., no choice of break frequency, no free spectral indices, very weak dependency on $\nu_{\rm p}^{\rm s}$), and that it is based on a physically well-motivated calculation (Strong et al. 2011; Orlando & Strong 2013). The cost, however, is less flexibility for tracing real spatial variations in the synchrotron spectral index, and thereby possibly greater cross-talk between synchrotron, free-free, and spinning dust. Nevertheless, in the absence of sufficiently strong data to disentangle these variations, we consider this a lesser evil than introducing a very strong statistical degeneracy between synchrotron, free-free, and spinning dust.

A second important example is the spinning dust component, which is currently implemented in terms of two independent SpDust components, one with a free peak frequency, $\nu_{\rm p}$, per pixel, and one with a spatially constant peak frequency, for a total of three free effective spinning dust parameters per pixel. While the introduction of the first component is unavoidable when combining the *Planck* and WMAP observations, the necessity of the second is more subtle. Without it we invariably find highly significant residuals (many tens to a few hundreds of microkelvin in the Galactic plane) in the 60–70 GHz frequency range, with dust-like morphology. This strongly suggests a model problem with either spinning or thermal dust (or both), but so far the only acceptable solution we have found is effectively to "widen" the SpDust spectrum slightly, which is most easily implemented by adding a second independent component. Introducing, say, a flatter thermal dust index at around 100 GHz tends to exacerbate rather than ameliorate the problem. We emphasize, however, that the current two-component spinning dust model is a purely phenomenological model introduced in the absence of physically well-motivated alternatives. We fully anticipate that additional low-frequency data or further theoretical developments will improve this model significantly in the future.

Third, we currently adopt a one-component greybody model with free emissivity index and temperature for thermal dust emission. Experimenting with various two-component alternatives, we find only one absolute requirement on the thermal dust model for frequencies up to 857 GHz, namely that at least three free thermal dust parameters per pixel are required to achieve an acceptable fit to the high-frequency observations. Whether those are $\{A_{\rm d}, \beta_{\rm d}, T_{\rm d}\}$, $\{A_{\rm d}^1, T_{\rm d}^1, A_{\rm d}^2\}$, or even $\{A_{\rm d}^1, \beta_{\rm d}^1, A_{\rm d}^2\}$(!) is not clear from the current data set[10]. On the other hand, it *is* clear that additional parameters are not required to model the current data set. For now, we prefer the one-component model simply because it has fewer global parameters than a corresponding two-parameter model, i.e., it requires no spatially fixed $\beta_{\rm d}$ and $T_{\rm d}$ for a second component, and therefore requires less tuning. This is not to be taken as a statement on the relative physical merits of the two models, however. Additional high-frequency observations are required to distinguish between them.

[10] Superscripts 1 and 2 refer to two independent greybody components.

5.2. Data preview

Before presenting the actual baseline results, it is useful to visually consider a few specific data combinations in order to gain some intuition regarding the power of these data for constraining specific parameters. In Fig. 6, we show four different sky maps, each of which highlights an important and distinct feature in the data. A similar discussion based on an internal linear combination (ILC) method is presented in Sect. 3 of Planck Collaboration XXV (2016).

Starting with the top panel, we plot the effective power-law index of the combined *Planck*, WMAP, and 408 MHz data, when fitting only a single power-law model at low-frequencies, as opposed to fitting individual synchrotron, free-free, and spinning dust components. All other components are defined by the usual baseline model. On the low-frequency side, this approach is thus identical to the 2013 model (Planck Collaboration XII 2014), although the data volume and frequency range are significantly increased. Despite these differences, the 2013 and 2015 low-frequency spectral index maps agree reasonably well, with a mean and standard deviation difference of 0.16 ± 0.14.

The main features in this spectral index map can be broadly characterized into two types of spatial signatures. First, we see many distinct regions (e.g., the Gum nebula, Orion, Zeta Oph, and the Cygnus complex) with a shallow spectral index of $\beta \approx -2$ and morphology as expected from various free-free tracers (e.g., Alves et al. 2015). Second, there are extended dark regions surrounding the Galactic plane, with very steep spectral indices of $\beta \lesssim -3.6$, and morphology similar to that of thermal dust emission. In addition, it is possible to see some weak hints of the North Galactic Spur, a strong synchrotron emission region, but since we adopted a synchrotron-like prior of $\beta \sim N(-3, 0.2)$ for the low-frequency power-law index in this analysis, it is difficult to distinguish this region from the prior-dominated background. The main point, however, is that even with such minimal modelling, there is strong evidence for at least three distinct physical components at low frequencies, namely: synchrotron, with $\beta \approx -3$; free-free, with $\beta \approx -2$; and a dust-like component, with $\beta \lesssim -3.6$. Among all the spectra shown in Fig. 4, only a spinning dust component with $\nu_{\rm p} \lesssim 30$ GHz can reasonably account for the latter.

In the second panel we show the ratio between the 857 and 545 GHz frequency maps, masking all pixels for which the 545 GHz amplitude is smaller than ten times its monopole. The spatial variations seen in this map cannot be explained either in terms of calibration or bandpass errors (because it is a ratio map, and either of those errors primarily affects the scale, not the morphology) or in terms of absolute offsets (because of the high mask threshold). They are robust features of the Galactic thermal dust emission, and must be explained by any Galactic model that include these observations. In fact, within our baseline model, these features can only be explained in terms of a spatially varying dust temperature. To be specific, the thermal dust appears hotter (i.e., has larger 857-to-545 ratio; see Fig. 4) near the Galactic centre than in the outer Galaxy (quadrants 2 and 3). Adopting a spatially constant dust temperature is no longer possible, and the only reason that the corresponding 2013 analysis could produce meaningful results with such an assumption was that it considered frequencies only up to 353 GHz, and also focused primarily on high Galactic latitudes (Planck Collaboration XII 2014).

The third panel shows the straight difference between the 100-ds1 and 100-ds2 maps. Because of the very short lever arm between these two frequencies, essentially all continuous

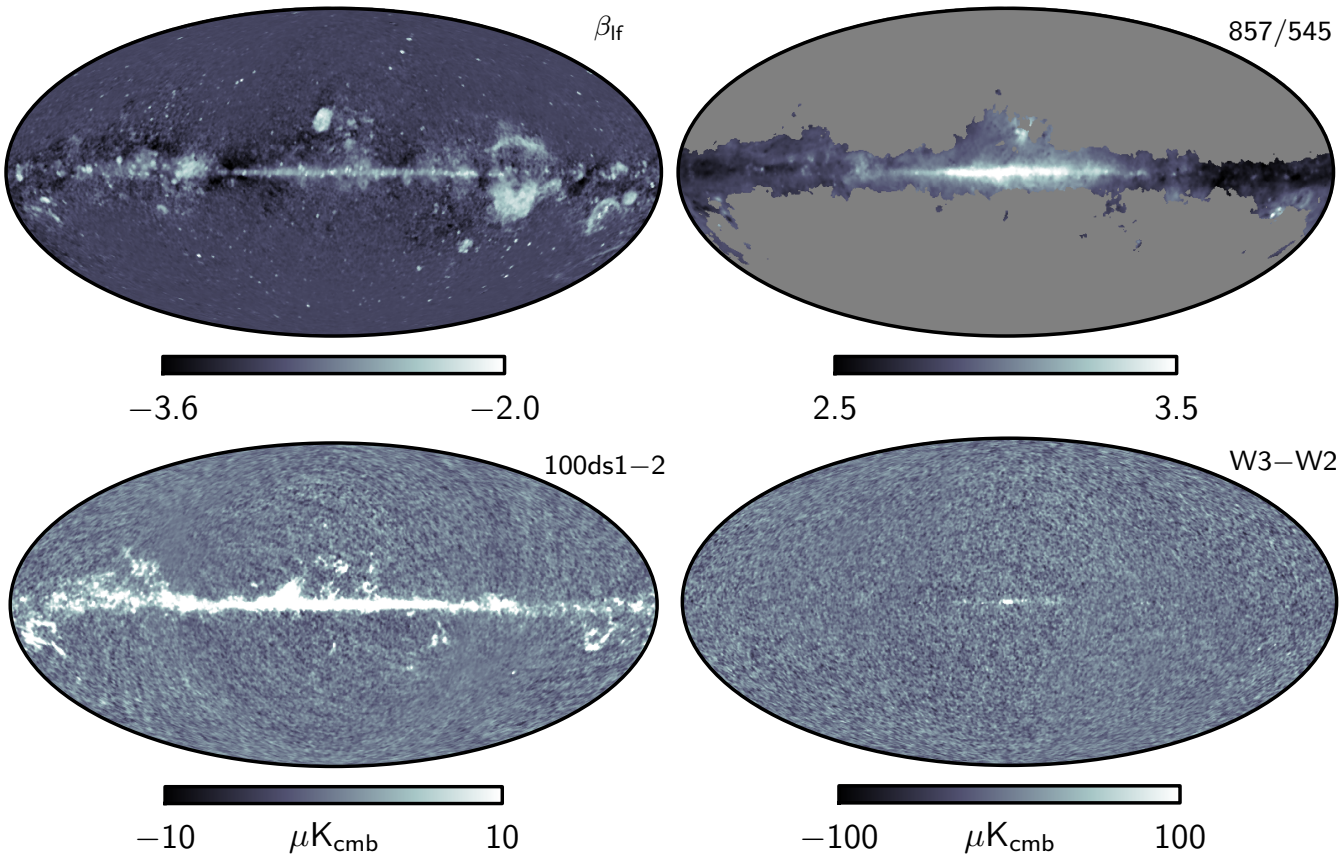

Fig. 6. *Top left*: effective low-frequency foreground spectral index as measured from the combination of *Planck*, WMAP, and 408 MHz, with no attempt to disentangle synchrotron, free-free, and spinning dust emission into separate components. However, higher-frequency components (CMB, CO, thermal dust, etc.) are fitted component-by-component, as in the baseline model. Note the very steep spectral indices, $\beta_{\rm lf} \lesssim -3.6$, near the Galactic plane, with dust-like morphology. These can only be reasonably explained in terms of spinning dust. *Top right*: ratio between the 857 and 545 GHz frequency maps, smoothed to 1° FWHM, highlighting the spatially varying temperature of thermal dust. The mask is defined by any region for which the 545 GHz amplitude is smaller than ten times the 545 GHz monopole. *Bottom left*: difference between the 100-ds1 and 100-ds2 detector maps, smoothed to 1°, demonstrating the presence of CO $J = 1 \rightarrow 0$ emission in these channels. *Bottom right*: difference between the WMAP W3 and W2 differencing assembly maps, smoothed to 1° FWHM. The excess signal near the Galactic centre is due to line emission in the 94 GHz channels. The peak amplitude of the difference map is 740 μK.

emission mechanisms cancel in this difference, leaving only the sharp line emission from CO $J = 1 \rightarrow 0$, as well as instrumental noise. This demonstrates the power of employing detector maps in the following analysis as opposed to frequency maps; using a fine-grained data set vastly increases our ability to extract line emission.

Whereas CO line emission was studied extensively in the *Planck* 2013 release, an additional new 94–100 GHz line feature is included in the current release (see Sect. 4.1). The primary contribution to this component is visualized in the bottom panel of Fig. 6, in terms of the WMAP W3−W2 difference map. The small but bright features near the Galactic centre (the maximum amplitude is 740 μK) are line emission within the *W*-band, as discussed in Sect. 4.1. This line is also covered by the two *Planck* 100 GHz channels. To prevent this additional emission from contaminating the main CO estimates, and to achieve an acceptable fit for the WMAP W-channels, we fit for this additional line emission component at 94/100 GHz.

5.3. Baseline model

We are now ready to present the *Planck* 2015 baseline diffuse astrophysical component model in temperature, as derived from the *Planck*, WMAP, and 408 MHz observations. An overview of the data products delivered through the *Planck* Legacy Archive (PLA)[11] is given in Table 5, including file names and FITS extension numbering, as well as summary statistics in the form of posterior maximum, mean, and rms values.

We start our review by considering data that are smoothed to a common resolution of 1° FWHM, representing the most complete data set and model possible, given the current data set. Processing these observations through the analysis pipeline outlined in Sect. 2, and adopting the baseline model described in Sect. 4.1, we obtain the set of maximum-posterior astrophysical parameter maps shown in the top panels of Figs. 7–19. The bottom panels show the corresponding rms maps found by computing the standard deviation over the ensemble of Gibbs samples. Please note that these rms maps account only for statistical errors from instrumental noise, and not for systematic uncertainties due to modelling errors. They are therefore only meaningful for pixels for which the goodness-of-fit is acceptable. Most importantly, they do not represent the true errors in the Galactic plane, where modelling errors dominate statistical errors.

Instrumental parameters, as well as monopole and dipole coefficients, are listed in Table 6, and Fig. 20 provides a visual comparison of the calibration factors for each *Planck* and WMAP

[11] http://pla.esac.esa.int/pla

Table 5. Summary of full-sky foreground products available from the PLA.

File	FITS extension	Parameter	ν_{ref} [GHz/band]	Posterior outside LM93 P_{max}	Mean	RMS	Unit
Temperature at 1° FWHM, $N_{side} = 256$							
AME	0	A_{sd1}	22.8	93 ± 118	92 ± 118	11 ± 3	μK_{RJ}
		ν_{sd1}	···	19 ± 1	19 ± 1	2.0 ± 0.8	GHz
	1	A_{sd2}	41	14 ± 21	18 ± 22	4.1 ± 2.8	μK_{RJ}
CMB	0	A_{cmb}	···	3 ± 67	3 ± 67	1.5 ± 0.8	μK_{cmb}
CO	0	A_{CO10}	100-ds1	0.3 ± 1.3	0.4 ± 1.3	0.06 ± 0.05	K_{RJ} km s^{-1}
	1	A_{CO21}	217-1	0.22 ± 0.57	0.29 ± 0.57	0.04 ± 0.01	K_{RJ} km s^{-1}
	2	A_{CO32}	353-ds2	0.16 ± 0.21	0.26 ± 0.26	0.05 ± 0.01	K_{RJ} km s^{-1}
dust	0	A_d	545	163 ± 228	163 ± 228	0.66 ± 0.11	μK_{RJ}
		T_d	···	21 ± 2	21 ± 2	1.1 ± 0.7	K
		β_d	···	1.53 ± 0.05	1.51 ± 0.06	0.05 ± 0.03	···
freefree	0	EM	···	15 ± 35	13 ± 35	2.3 ± 2.4	cm^{-6} pc
		T_e	···	7000 ± 11	7000 ± 11	···	K
Synchrotron	0	A_s	0.408	20 ± 15	20 ± 15	1.1 ± 0.2	K_{RJ} [a]
SZ	0	A_{sz}	···	1.4 ± 1.4 [b]	2.0 ± 1.3 [b]	0.8 ± 0.2 [b]	$10^{-6}\, y_{sz}$
xline [c]	0	$A_{94/100}$	100-ds1	0.09 ± 0.06	0.9 ± 0.8	0.7 ± 0.6	μK_{cmb}
Temperature at 7.′5 FWHM, $N_{side} = 2048$							
CO21 [d]	0	A_{CO21}	217-1	0.2 ± 0.8	···	···	K_{RJ} km s^{-1}
ThermalDust [d]	0	A_d	545	0.2 ± 0.8	···	···	μK_{RJ}
		β_d	···	1.54 ± 0.07	···	···	···
Polarization at 40′ FWHM, $N_{side} = 256$							
SynchrotronPol [d]	0	P^e_s	30	12 ± 9	···	···	μK_{RJ}
Polarization at 10′ FWHM, $N_{side} = 1024$							
DustPol [d]	0	P^e_d	353	8 ± 10	···	···	μK_{RJ}

Notes. Each entry in the first column corresponds to one multi-column and (optionally) multi-extension FITS file, named `COM_CompMap_{label}-commander_{nside}_R2.00.fits`. The various columns in each extension list the posterior maximum, mean, and rms maps, in that order, when available. The values reported in Cols. 5 to 7 in this table are the mean and standard deviations of these posterior statistic maps. [(a)] The data file unit is μK_{RJ} but for convenience we list numbers in K_{RJ} in this table. [(b)] Evaluated only over the Coma and Virgo regions. [(c)] This is the 94/100 GHz line emission component. [(d)] Only the full-mission maps are summarized in this table, but the data files also include corresponding maps for half-mission, half-year, and half-ring data splits. [(e)] Data files contains Stokes Q and U parameters, not the polarization amplitude, $P = \sqrt{Q^2 + U^2}$, listed here.

detector map[12]. Global (i.e., spatially uniform) astrophysical parameters are listed in Table 7. The full marginal uncertainties of these parameters are dominated by modelling, not statistical errors. For this reason, the tabulated uncertainties are computed through realistic end-to-end simulations, as implemented in the *Planck* 2015 FFP8 simulations (Planck Collaboration XII 2016). These simulations were analysed blindly as part of the CMB validation efforts (Planck Collaboration IX 2016), using the exact same machinery as used in this paper. Further, they are based on a significantly different foreground model than the baseline model adopted here, and they therefore at least partially account for modelling errors, as well as known systematic and map-making uncertainties. The only differences in the fitted model compared to the present baseline are that it includes only one spinning dust component and no 94/100 GHz line emission or SZ components.

Based on these simulations, we estimate the uncertainties on the calibration and bandpass measurements directly from the simulations, comparing output parameters against known inputs. The monopole and dipole uncertainties are, however, first based on the statistical errors derived from the Gibbs chains, and then rounded up (where necessary) to be no smaller than the corresponding FFP8 simulation uncertainties[13]. Thus they correspond to the maximum of the instrumental and the modelling errors. Furthermore, we reemphasize that the reported monopole and dipole values are conditional with respect to the nominal *Planck*, H I and synchrotron priors, as defined by Planck Collaboration VI (2016), Planck Collaboration VIII (2016), and Wehus et al. (2016).

The uncertainties in the CO line ratios listed in Table 7, which are model-dominated, are also taken from the FFP8 simulations. The 94/100 GHz line ratios, however, are noise

[12] The re-calibration factors listed in Table 6 for 545 and 857 GHz refer to multiplicative factors in native map units, MJy sr^{-1}. When making comparison with similar calibration factors derived from corresponding maps defined in units of μK, one additionally has to account for differences in unit conversion due to bandpass shifts, as listed in Table 3.

[13] Based on the FFP8 simulations we never report monopole (dipole) uncertainties smaller than 1 μK (0.1 μK).

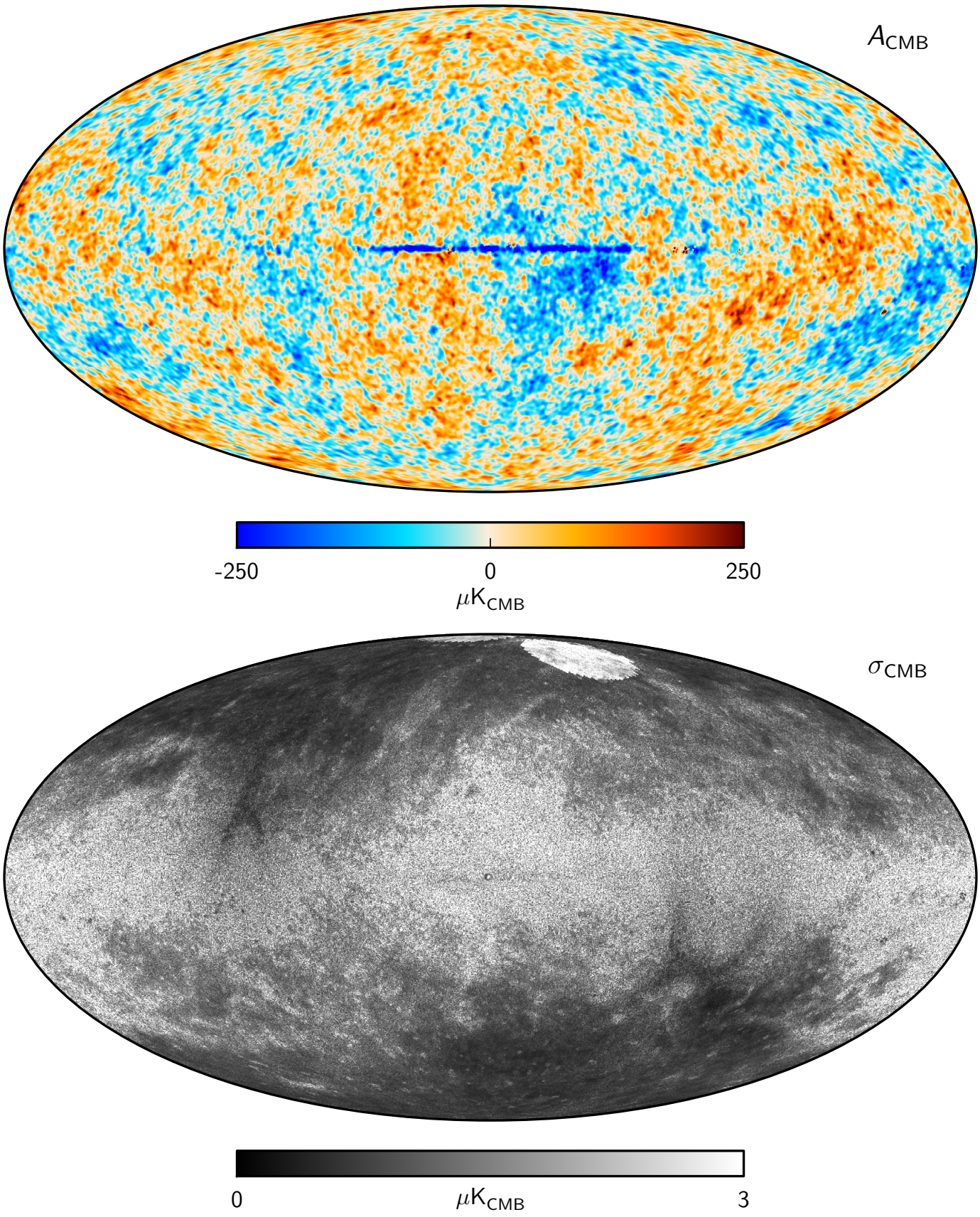

Fig. 7. Maximum posterior (*top*) and posterior rms (*bottom*) CMB intensity maps derived from the joint baseline analysis of *Planck*, WMAP, and 408 MHz observations. The two circular regions close to the North Galactic Pole in the rms map correspond to the Coma and Virgo clusters, for which the thermal SZ efect is fitted together with the primary diffuse components. Note also that the rms map includes statistical errors alone, not modelling errors, and they are therefore only meaningful in regions where the corresponding χ^2 is acceptable; see Fig. 22. Both panels employ linear colour scales.

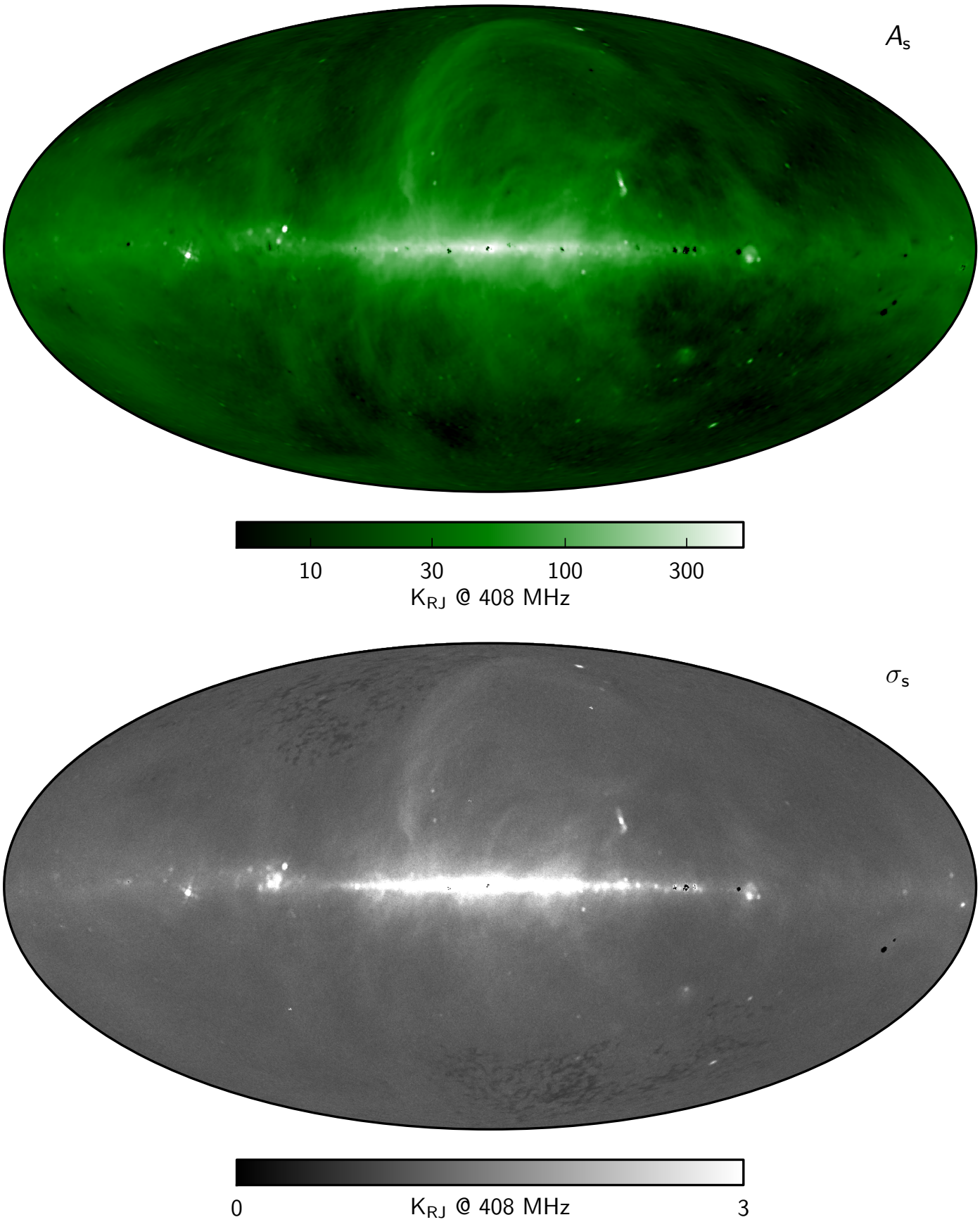

Fig. 8. Maximum posterior (*top*) and posterior rms (*bottom*) synchrotron intensity maps derived from the joint baseline analysis of *Planck*, WMAP, and 408 MHz observations. The *top panel* employs a non-linear high dynamic range colour scale, while the *bottom panel* employs a regular linear colour scale.

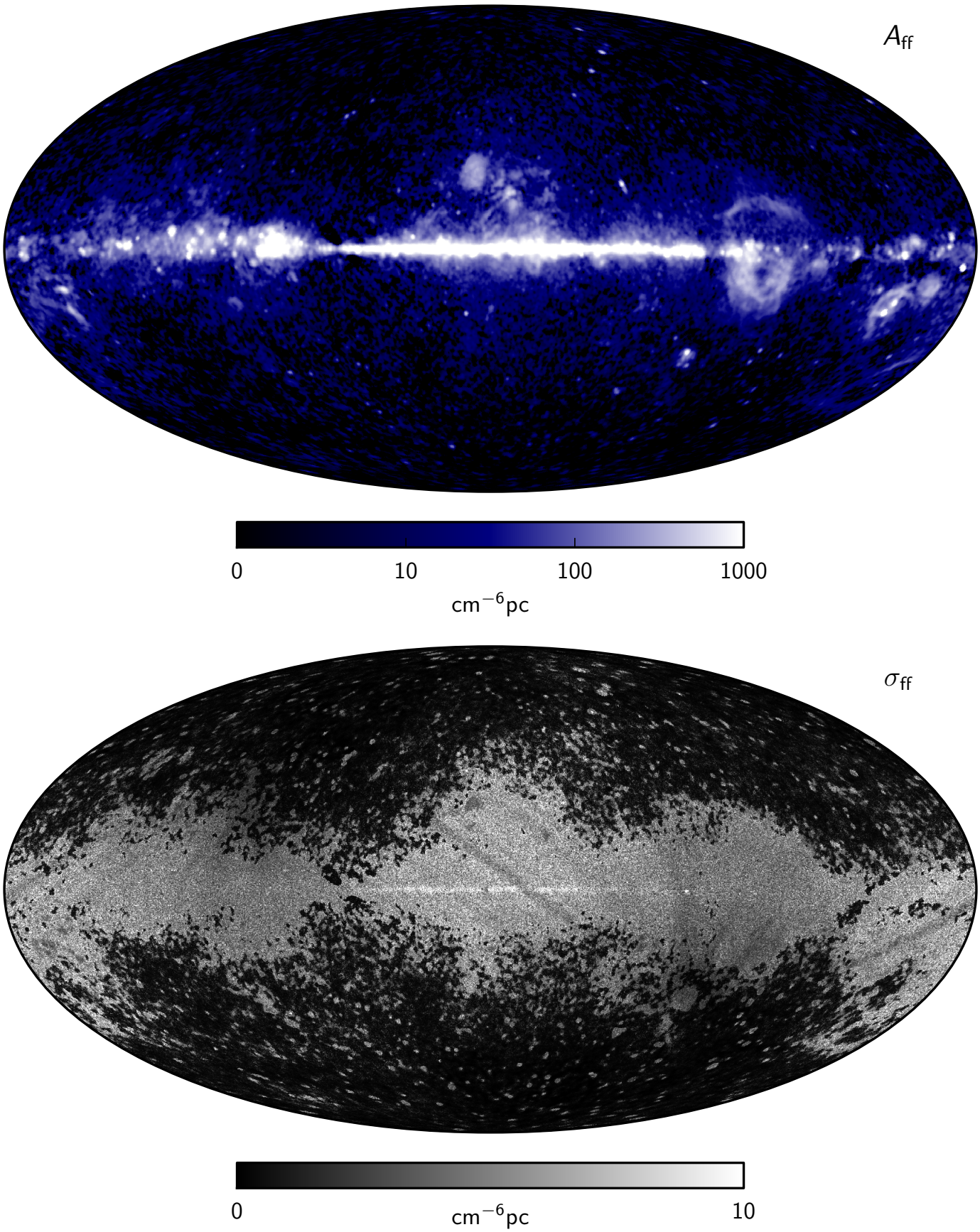

Fig. 9. Maximum posterior (*top*) and posterior rms (*bottom*) free-free emission measure maps derived from the joint baseline analysis of *Planck*, WMAP, and 408 MHz observations. The *top panel* employs a non-linear high dynamic range colour scale, while the *bottom panel* employs a regular linear colour scale.

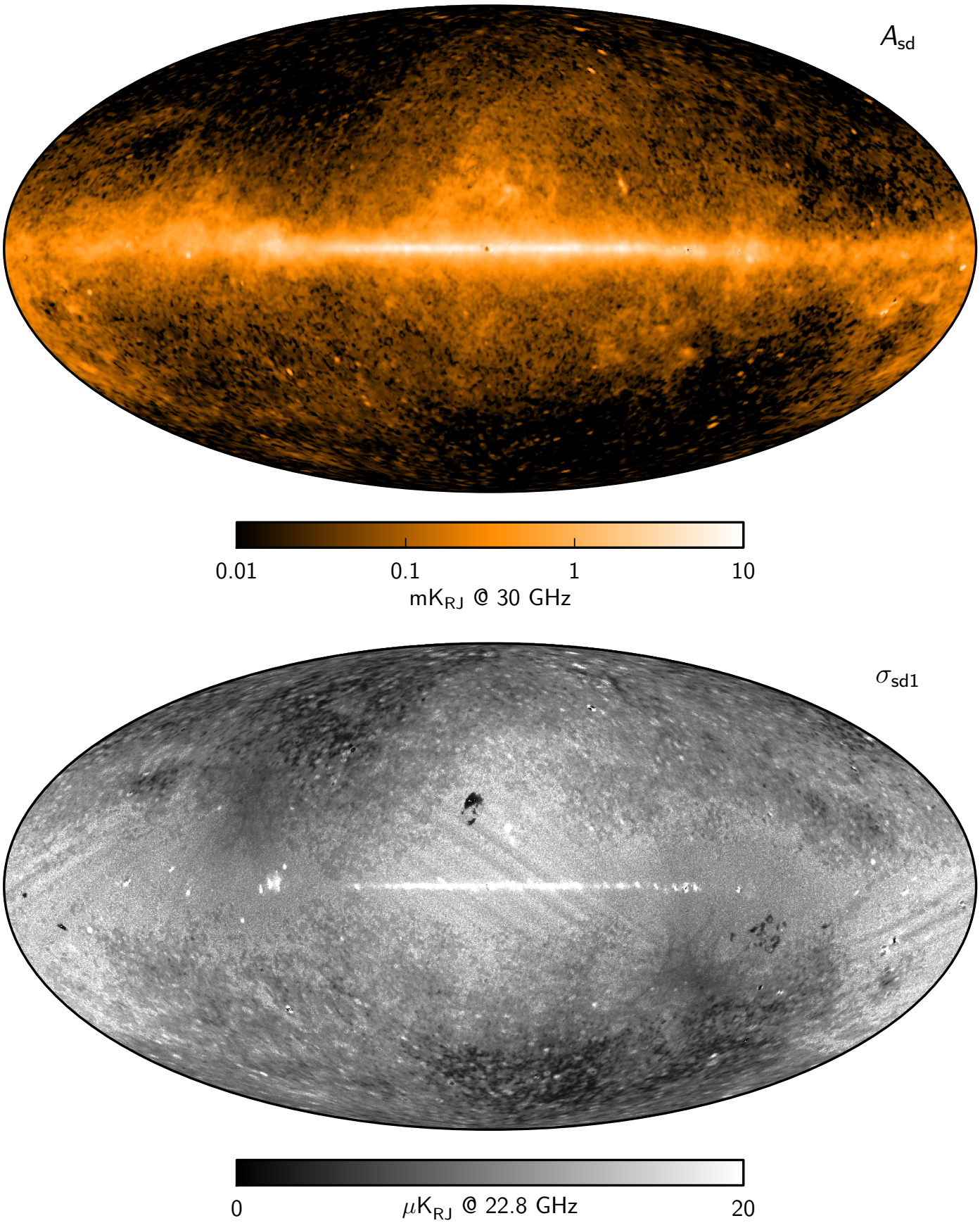

Fig. 10. Maximum posterior (*top*) and posterior rms (*bottom*) spinning dust intensity maps derived from the joint baseline analysis of *Planck*, WMAP, and 408 MHz observations. The top panel shows the sum of the two spinning dust components in the baseline model, evaluated at 30 GHz, whereas the *bottom* shows the standard deviation of only the primary spinning dust component, evaluated at 22.8 GHz. Note that the top panel employs a non-linear high dynamic range colour scale, while the bottom panel employs a regular linear colour scale.

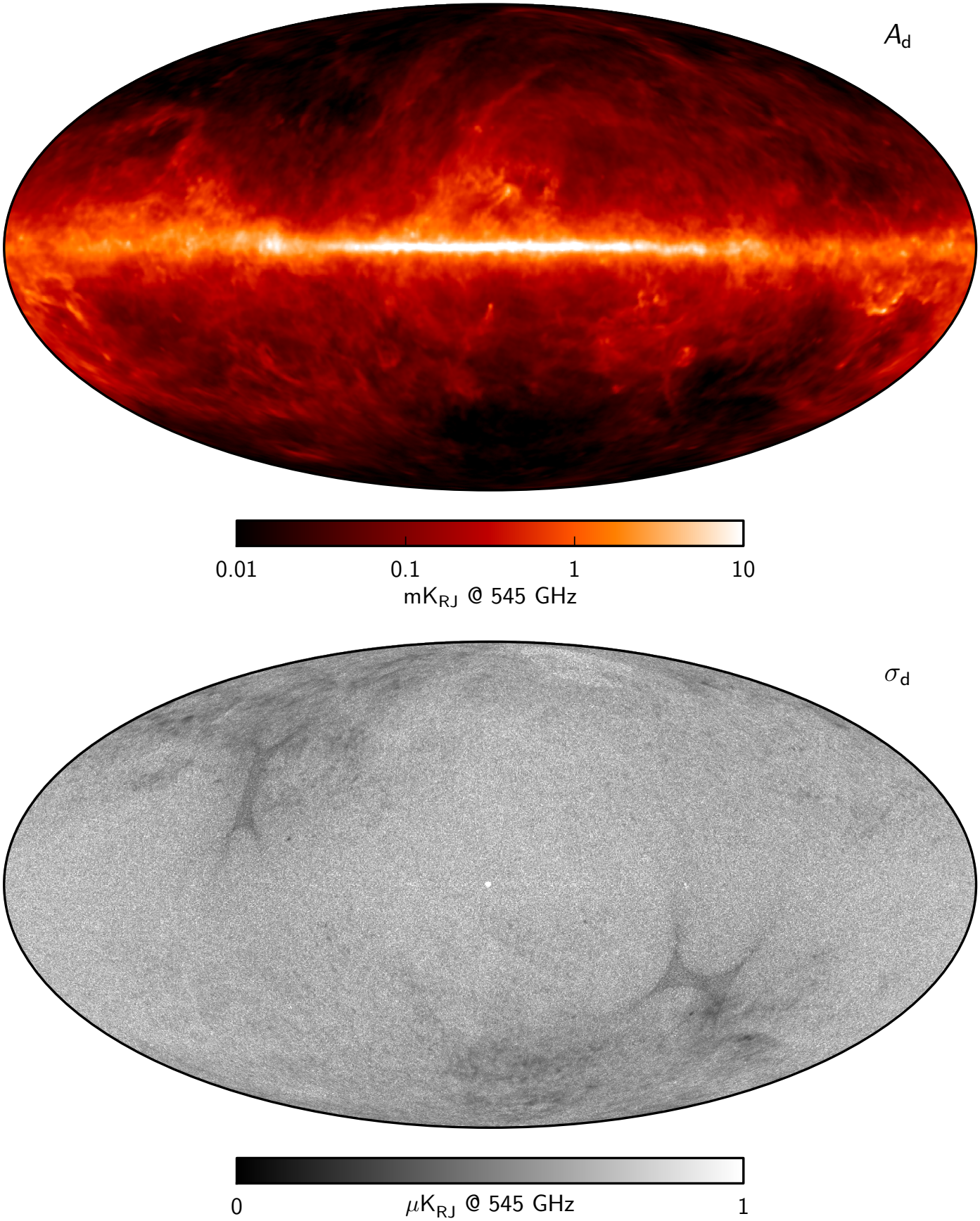

Fig. 11. Maximum posterior (*top*) and posterior rms (*bottom*) thermal dust intensity maps derived from the joint baseline analysis of *Planck*, WMAP, and 408 MHz observations. The top panel employs a non-linear high dynamic range colour scale, while the bottom panel employs a regular linear colour scale.

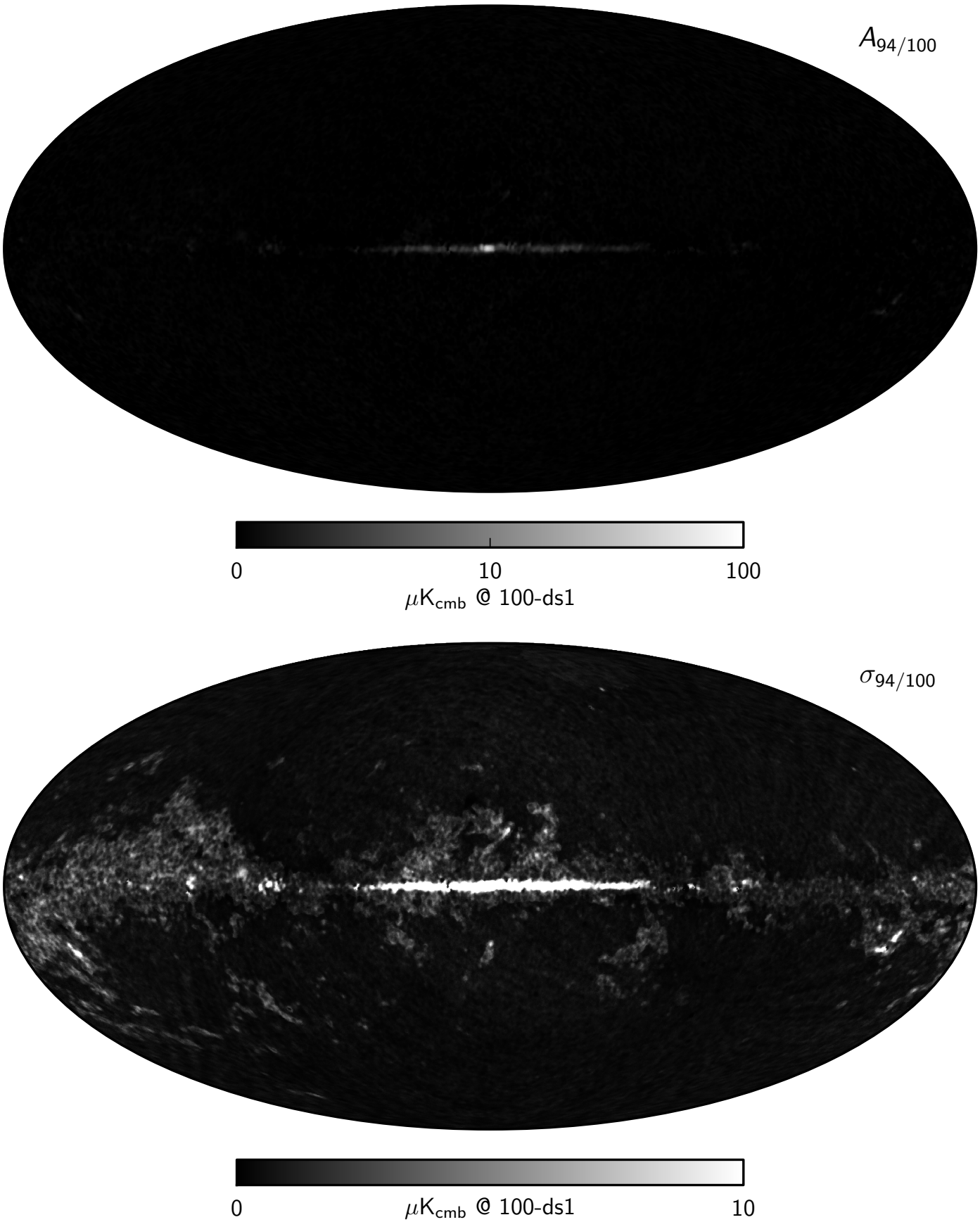

Fig. 12. Maximum posterior (*top*) and posterior rms (*bottom*) 94/100 GHz line emission maps derived from the joint baseline analysis of *Planck*, WMAP, and 408 MHz observations. The top panel employs a non-linear high dynamic range colour scale, while the bottom panel employs a regular linear colour scale.

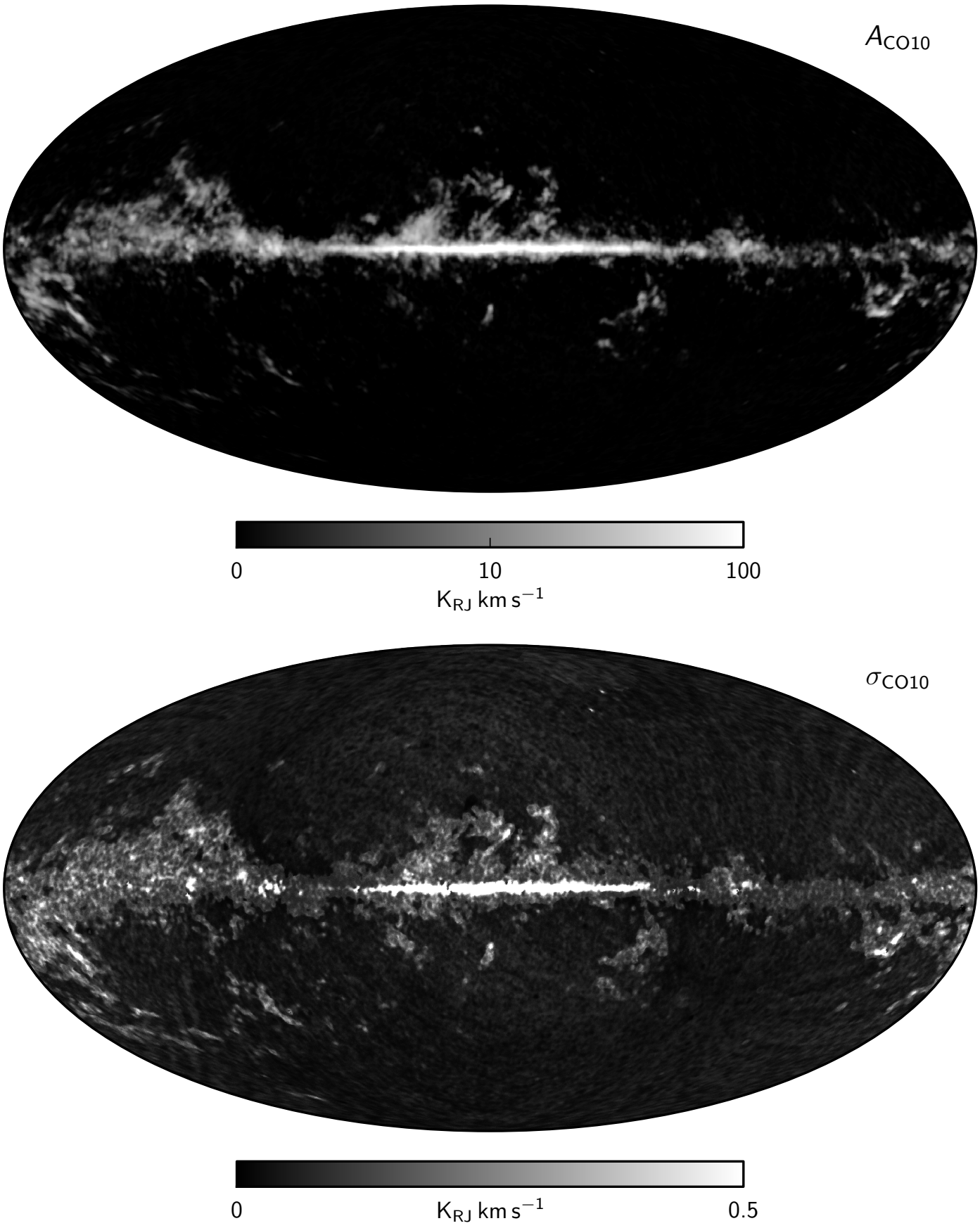

Fig. 13. Maximum posterior (*top*) and posterior rms (*bottom*) CO $J = 1 \rightarrow 0$ line emission maps derived from the joint baseline analysis of *Planck*, WMAP, and 408 MHz observations. The top panel employs a non-linear high dynamic range colour scale, while the bottom panel employs a regular linear colour scale.

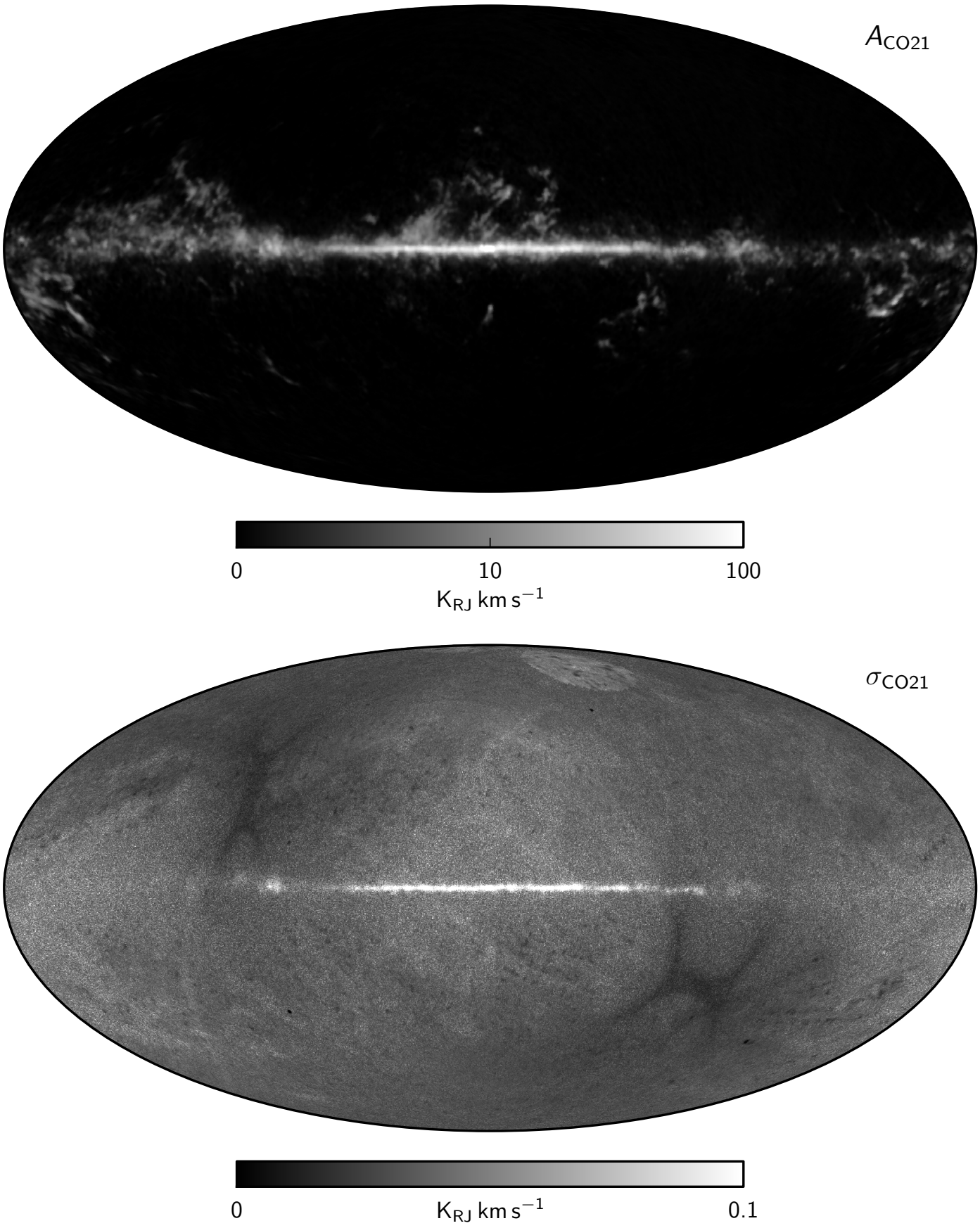

Fig. 14. Maximum posterior (*top*) and posterior rms (*bottom*) CO $J = 2 \rightarrow 1$ line emission maps derived from the joint baseline analysis of *Planck*, WMAP, and 408 MHz observations. The two circular regions close to the North Galactic Pole in the rms map correspond to the Coma and Virgo clusters, for which the thermal SZ effect is fitted together with the primary diffuse components. The top panel employs a non-linear high dynamic range colour scale, while the bottom panel employs a regular linear colour scale.

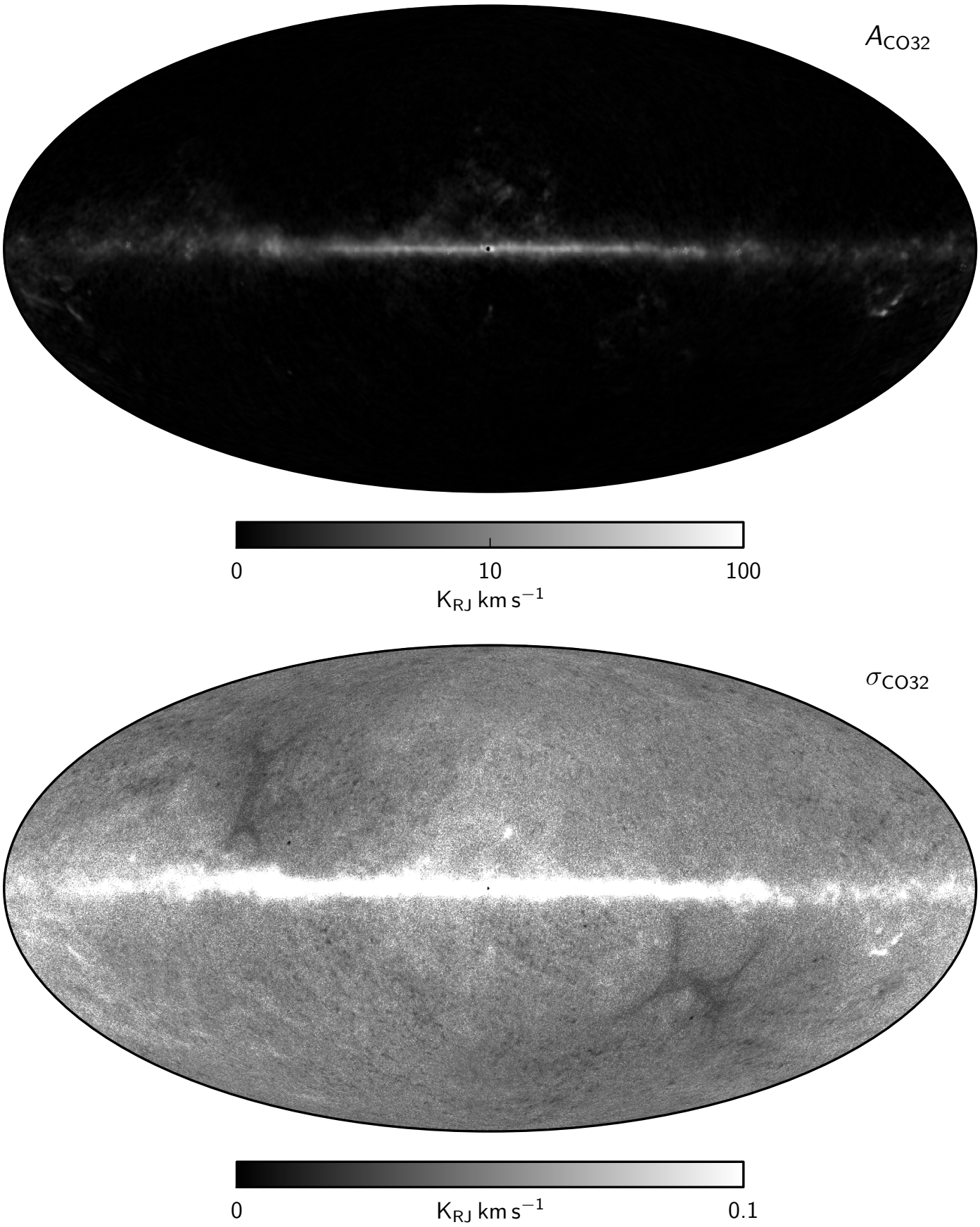

Fig. 15. Maximum posterior (*top*) and posterior rms (*bottom*) CO $J = 3 \rightarrow 2$ line emission maps derived from the joint baseline analysis of *Planck*, WMAP, and 408 MHz observations. The top panel employs a non-linear high dynamic range colour scale, while the bottom panel employs a regular linear colour scale.

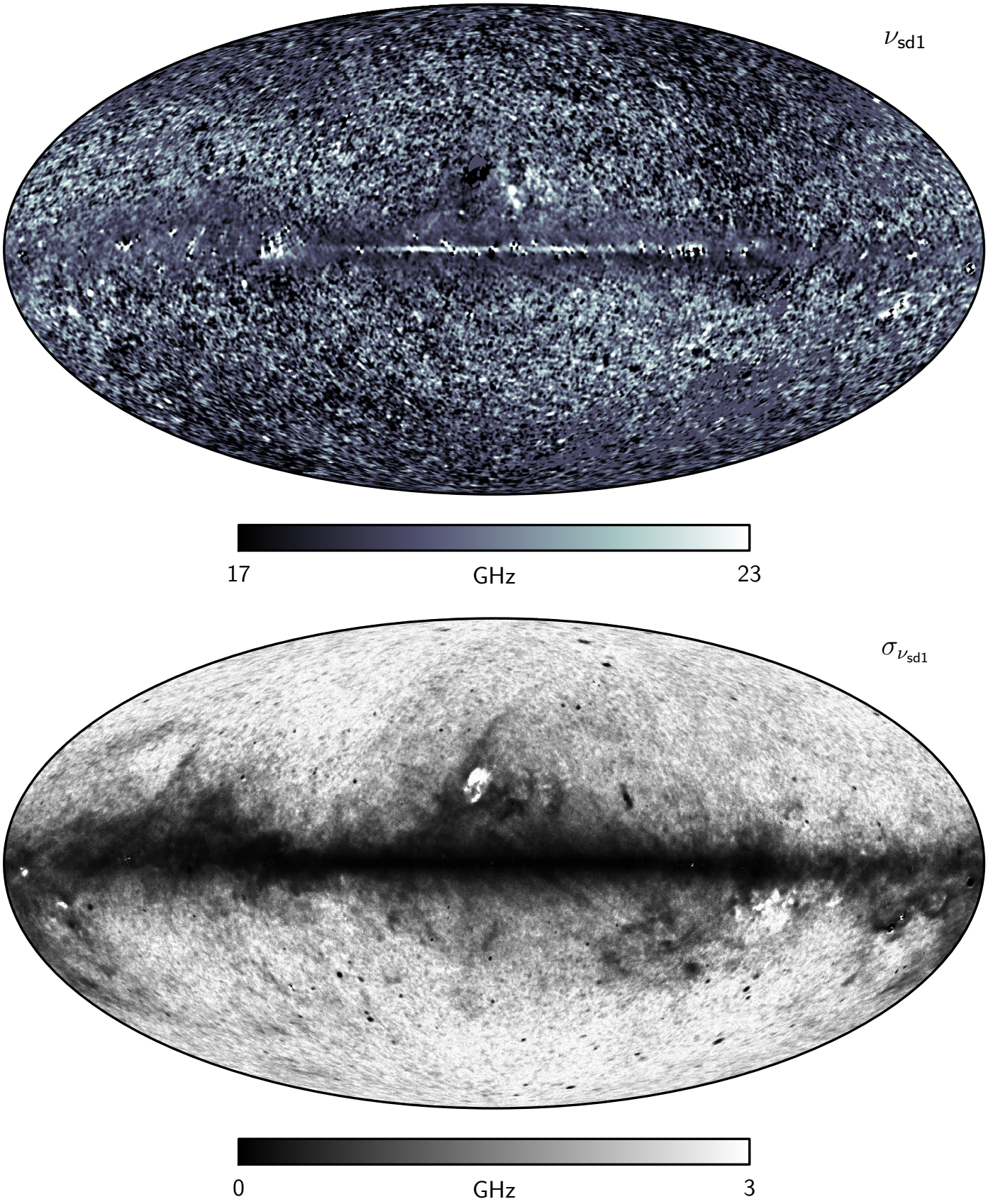

Fig. 16. Maximum posterior (*top*) and posterior rms (*bottom*) spinning dust peak frequency maps derived from the joint baseline analysis of *Planck*, WMAP, and 408 MHz observations. Both panels employ linear colour scales.

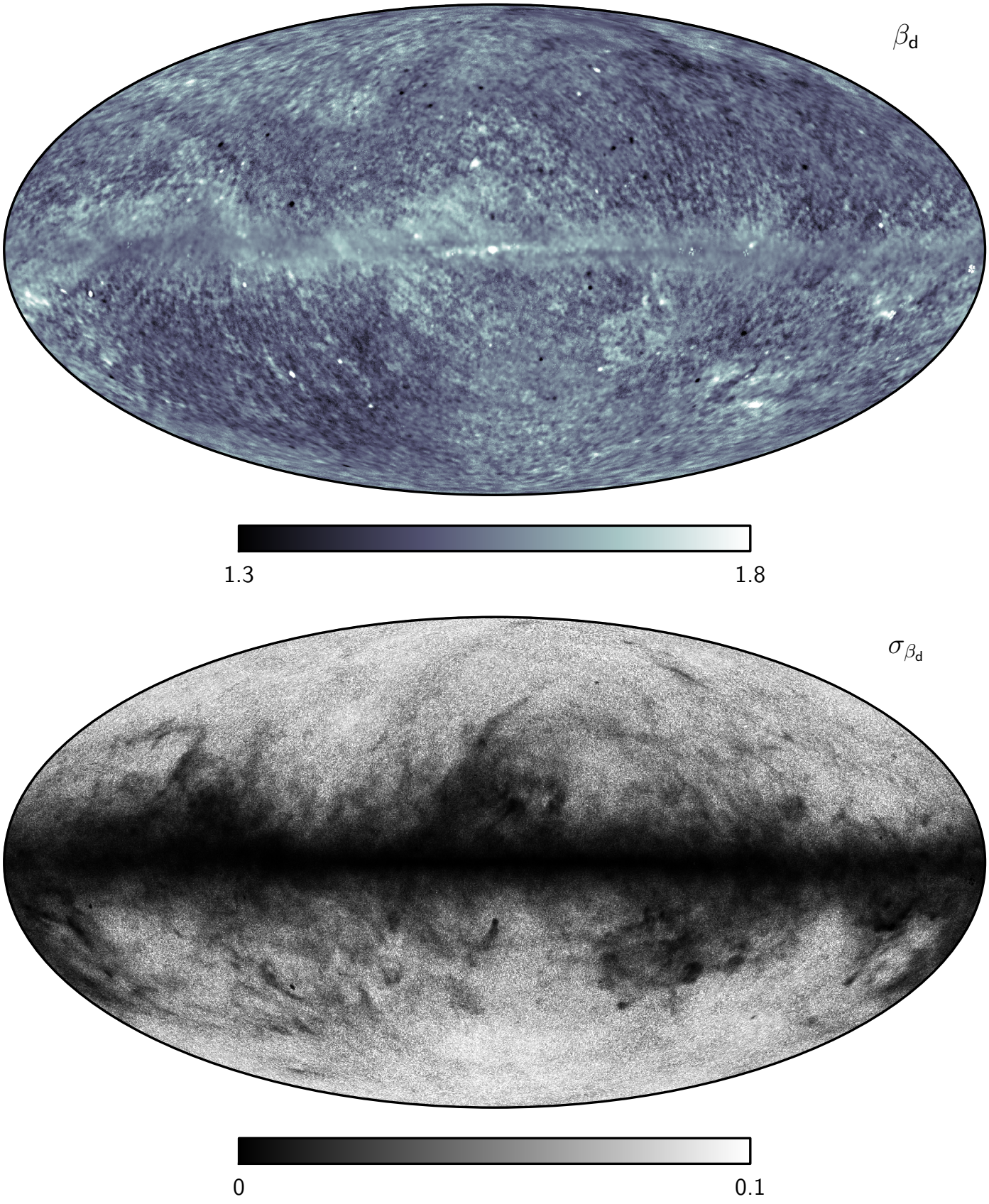

Fig. 17. Maximum posterior (*top*) and posterior rms (*bottom*) thermal dust spectral index maps derived from the joint baseline analysis of *Planck*, WMAP, and 408 MHz observations. Both panels employ linear colour scales.

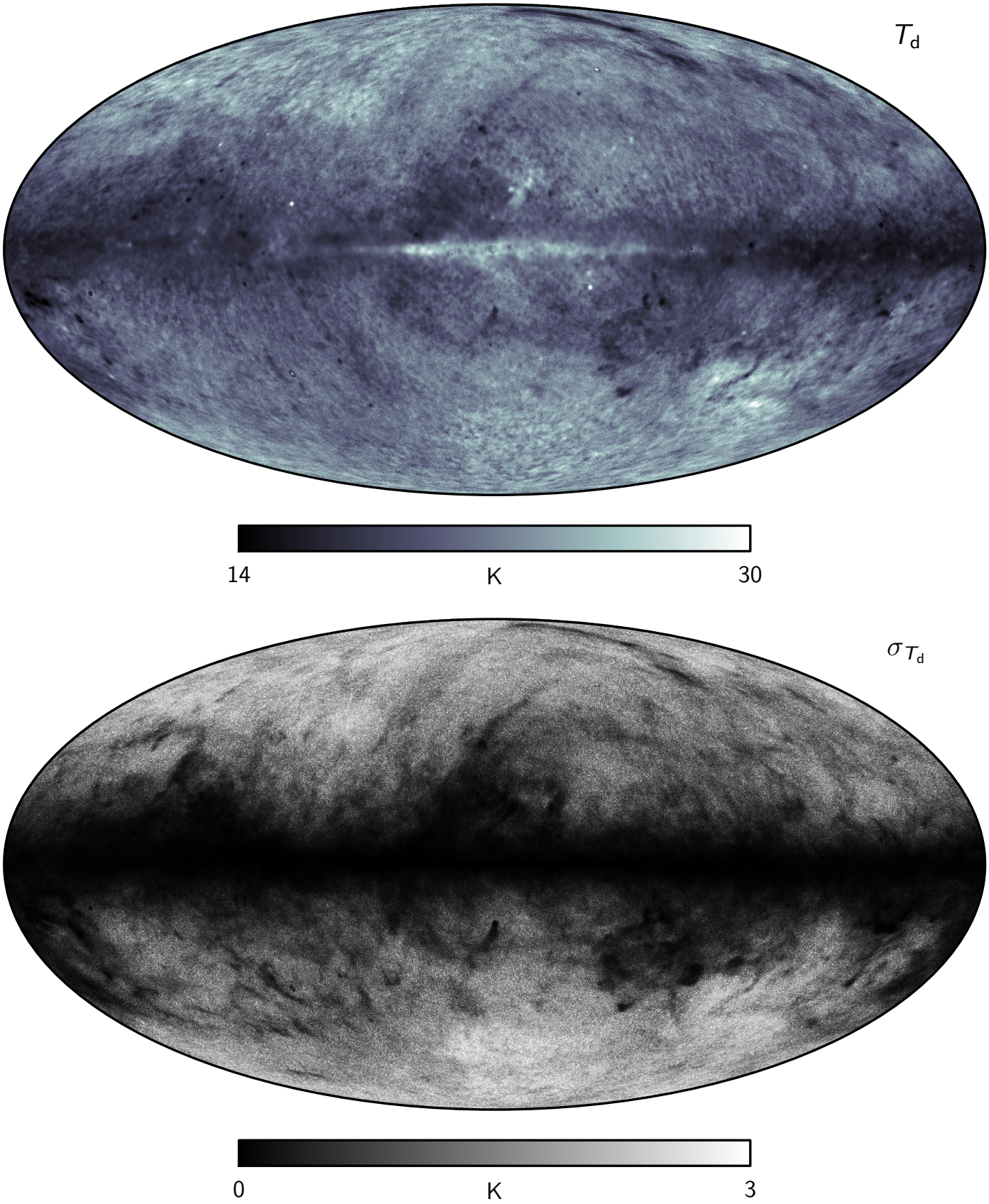

Fig. 18. Maximum posterior (*top*) and posterior rms (*bottom*) thermal dust temperature maps derived from the joint baseline analysis of *Planck*, WMAP, and 408 MHz observations. Both panels employ linear colour scales.

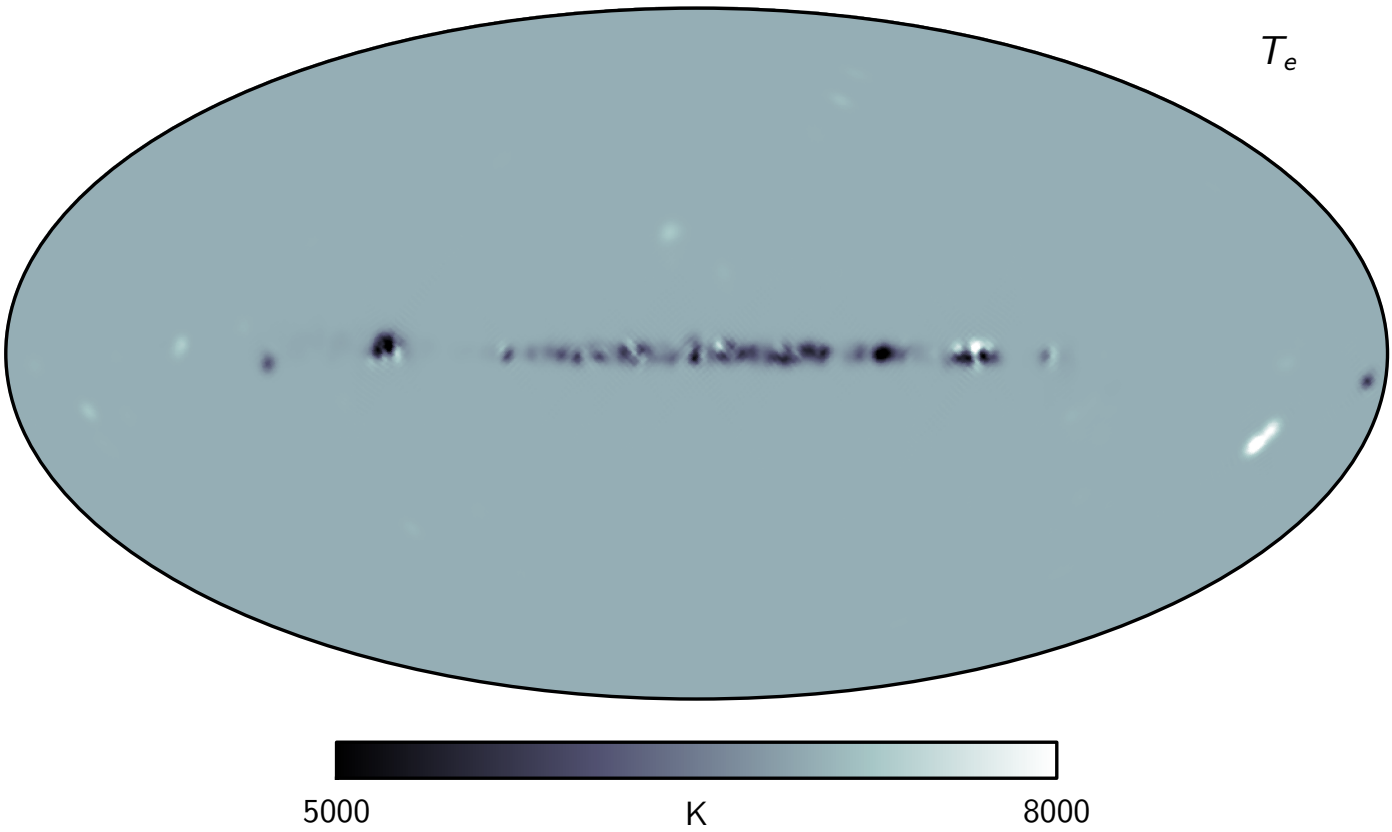

Fig. 19. Maximum posterior (free-free) electron temperature map derived from the joint baseline analysis of *Planck*, WMAP, and 408 MHz observations. The figure employs a linear colour scale.

dominated, and they are therefore taken directly as the standard deviation of the posterior distribution, i.e., from the Gibbs samples. Finally, we do not quote any uncertainties on the peak frequency of the second spinning dust component or the frequency scale factor of the synchrotron GALPROP model. Both of these are completely dependent on other parameters in the model, and the full joint distribution is highly non-Gaussian. As a result, we only quote the maximum-likelihood values for these, and notice that their full marginal uncertainties are very large, possibly up to 50% or more.

5.3.1. Goodness-of-fit

Next, the goodness-of-fit of the model is summarized in Figs. 21–22 and in Table 8. Starting with Fig. 21, residual maps for each channel are shown on the form $(\boldsymbol{d}_\nu - \boldsymbol{s}_\nu)$, and these give the most complete view of the performance of the model out of all the statistics considered in the following. In addition, they provide a direct visual summary of remaining low-level systematics in the data, which should prove useful for future reprocessing of the same data. Overall, we see in these maps that the model provides an excellent fit to all channels at high Galactic latitudes. Please note that the colour scales vary from $\pm 2\,\mu$K at the CMB dominated *Planck* HFI channels, through $\pm 10\,\mu$K for most of the WMAP channels, to ± 1K and ± 0.05 MJy sr^{-1} for the 408 MHz and 545 GHz channels. In fact, the solution is sufficiently free of artifacts that the dominant systematic effect in the 100-ds2 residual map is Galactic rotation projected into the CMB frequencies by the CO $J = 1 \rightarrow 0$ emission line. The same feature is also seen in several other channels, although at slightly lower significance.

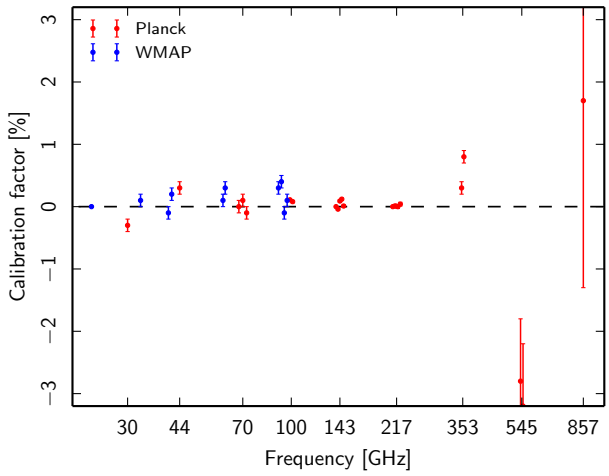

Fig. 20. Detector map and differencing assembly re-calibration factors for *Planck* and WMAP, as reported in Table 6.

The top panel of Fig. 22 shows the corresponding χ^2 map as defined by Eq. (14), but summed only over the accepted frequency channels. The bottom panel shows a histogram of these χ^2 values including all pixels admitted by the PM61 processing mask.

Together, these figures provide a useful qualitative summary of the goodness-of-fit of the baseline model. However, providing a corresponding rigorous statistical description is complicated, because the effective number of degrees of freedom per pixel is not well defined. The usual approach of subtracting the number of free parameters from the number of data points is not

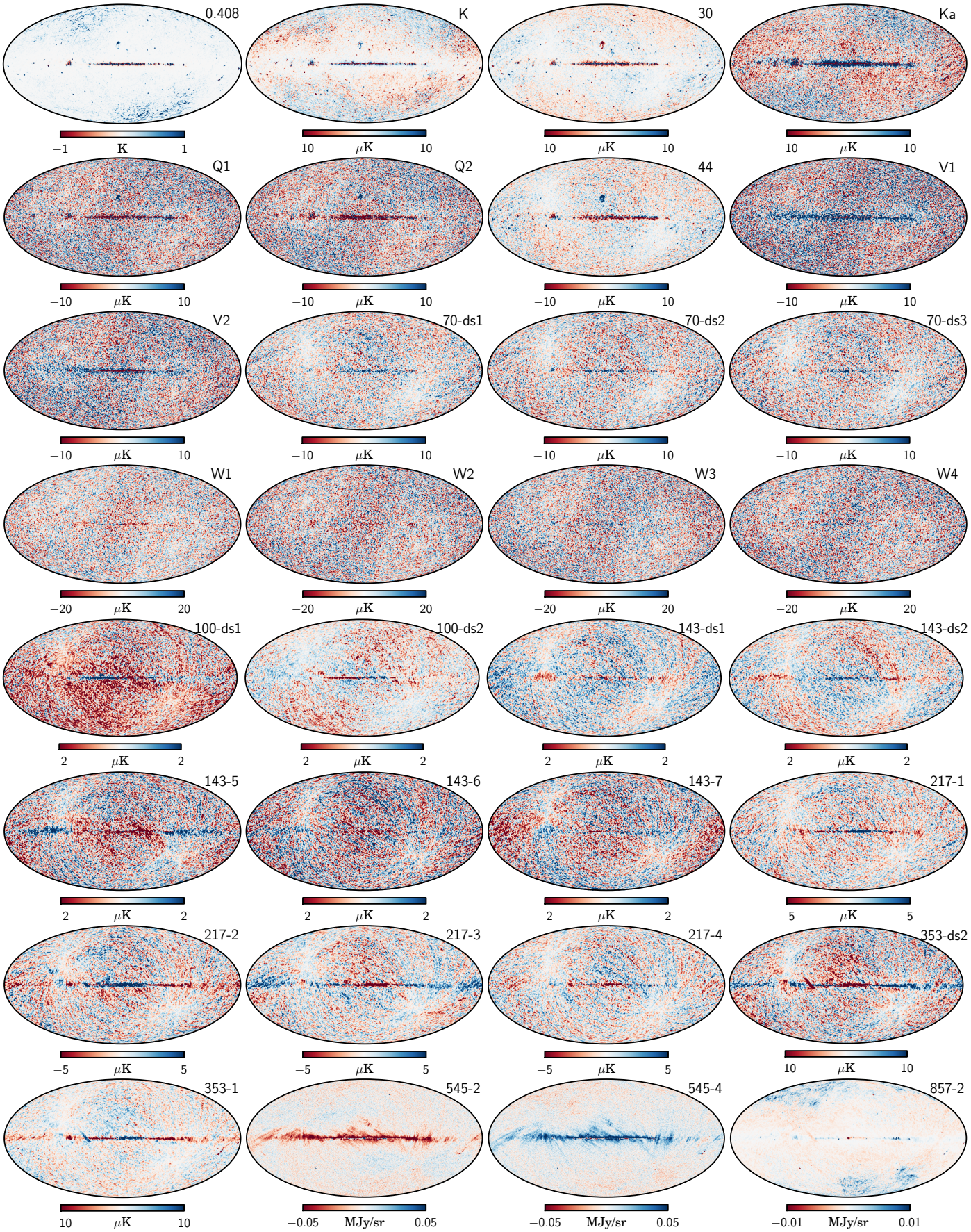

Fig. 21. Residual maps, $\boldsymbol{d}_\nu - \boldsymbol{s}_\nu$, for each detector data set included in the baseline joint *Planck*, WMAP, and 408 MHz temperature analysis. All panels employ linear colour scales. The label in the top left corner of each panel indicates frequency channel.

Table 6. Monopoles, dipoles, calibration factors and bandpass corrections derived within the baseline temperature model.

Survey	Frequency [GHz]	Detector label	Monopole [μK]	X dipole [μK]	Y dipole [μK]	Z dipole [μK]	Calibration [%]	Bandpass shift [GHz]
Planck LFI	30	. . .	-17 ± 1	0[a]	0[a]	0[a]	-0.3 ± 0.1[f]	0.3 ± 0.1
	44	. . .	11 ± 1	0.5 ± 0.2	-0.3 ± 0.1	0.5 ± 0.1	0.3 ± 0.1[f]	0.1 ± 0.1
	70	ds1	16 ± 1	0.5 ± 0.1	-1.1 ± 0.1	1.1 ± 0.1	0.0 ± 0.1[f]	-0.4 ± 1.0
		ds2	16 ± 1	0.5 ± 0.1	-1.0 ± 0.1	1.1 ± 0.1	0.1 ± 0.1[f]	1.1 ± 1.0
		ds3	16 ± 1	-0.1 ± 0.1	-0.9 ± 0.1	0.8 ± 0.1	-0.1 ± 0.1[f]	0.5 ± 1.0
Planck HFI	100	ds1	9[a]	0[a]	0[a]	0[a]	0.11 ± 0.02	-0.5 ± 0.7
		ds2	8 ± 1	0.0 ± 0.1	-0.1 ± 0.1	0.3 ± 0.2	0.08 ± 0.02	-0.4 ± 0.6
	143	ds1	21[a]	0[a]	0[a]	0[a]	0[a]	0.7 ± 0.2
		ds2	21 ± 1	0.0 ± 0.1	0.0 ± 0.1	-0.1 ± 0.1	-0.04 ± 0.02	-0.2 ± 0.2
		5	21 ± 1	-0.5 ± 0.1	0.0 ± 0.1	-0.1 ± 0.1	0.09 ± 0.02	-0.5 ± 0.2
		6	21 ± 1	-0.4 ± 0.1	0.0 ± 0.1	-0.1 ± 0.1	0.12 ± 0.02	0.3 ± 0.2
		7	20 ± 1	-0.2 ± 0.1	0.0 ± 0.1	-0.0 ± 0.1	0.01 ± 0.02	-0.4 ± 0.2
	217	1	68 ± 1	-0.8 ± 0.1	-2.6 ± 0.1	2.9 ± 0.1	0[a]	-0.1 ± 0.1
		2	68 ± 1	-0.7 ± 0.1	-2.8 ± 0.1	3.1 ± 0.1	0.01 ± 0.03	-0.1 ± 0.1
		3	67 ± 1	-1.0 ± 0.1	-2.6 ± 0.1	3.0 ± 0.1	0.00 ± 0.03	0.1 ± 0.1
		4	68 ± 1	-0.4 ± 0.1	-2.7 ± 0.1	3.0 ± 0.1	0.04 ± 0.03	-0.1 ± 0.1
	353	ds2	447 ± 5	-3 ± 1	-6 ± 1	6 ± 1	0.3 ± 0.1	0.3 ± 0.1
		1	449 ± 6	-4 ± 1	-16 ± 1	15 ± 1	0.8 ± 0.1	-0.0 ± 0.1
	545	2	0.370[a]	0[a]	0[a]	-2.8[e]	2.0[e]	
		4	0.36 ± 0.01[c]	0[a]	0[a]	0[a]	-3.2[e]	2.8[e]
	857	2	0.62 ± 0.01[c]	0[a]	0[a]	0[a]	1.7[e]	5.8[e]
WMAP	23	K	-8 ± 1	-4.5 ± 2.0	1.6 ± 0.5	-3.7 ± 0.4	0[a]	0[a]
	33	Ka	3[b]	-0.7 ± 0.6	-4.7 ± 0.2	3.8 ± 0.1	0.1 ± 0.1	0[a]
	41	Q1	2 ± 1	0.5 ± 0.3	-4.6 ± 0.1	3.5 ± 0.1	-0.1 ± 0.1	0[a]
		Q2	2 ± 1	0.4 ± 0.3	-4.8 ± 0.1	3.7 ± 0.1	0.2 ± 0.1	0.3 ± 0.1
	61	V1	1 ± 1	0.2 ± 0.1	-5.5 ± 0.1	4.2 ± 0.1	0.1 ± 0.1	0[a]
		V2	1 ± 1	0.0 ± 0.1	-5.5 ± 0.1	4.2 ± 0.1	0.3 ± 0.1	-0.1 ± 0.1
	94	W1	-5 ± 2	0.3 ± 0.1	-5.3 ± 0.2	4.1 ± 0.2	0.3 ± 0.1	0[a]
		W2	-5 ± 2	0.1 ± 0.1	-5.0 ± 0.1	3.9 ± 0.2	0.4 ± 0.1	-0.7 ± 0.3
		W3	-6 ± 2	0.2 ± 0.1	-6.0 ± 0.2	4.3 ± 0.3	-0.1 ± 0.1	0.3 ± 0.3
		W4	-5 ± 2	-0.0 ± 0.1	-6.1 ± 0.1	5.2 ± 0.2	0.1 ± 0.1	-0.6 ± 0.3
Haslam	0.408	. . .	8.9[b,d]	3.2[b,d]	0.7[b,d]	-0.8[b,d]	0[a]	0[a]

Notes. [(a)] Fixed at reference value. [(b)] Fixed at values derived by Wehus et al. (2016). [(c)] Unit is MJy/sr. [(d)] Unit is K. [(e)] For a detailed discussion of bandpass and calibration uncertainties at 545 and 857 GHz, see Sect. 4.3. [(f)] Adjusted for the well-understood LFI "beam normalization factor" (see Planck Collaboration II 2016).

applicable, because informative priors (most notably the positivity prior) eliminate large parts of the parameter space. A parameter that is prior-dominated therefore does not reduce the number of degrees of freedom by unity, but only a fraction of unity. Second, smoothing the data to a common resolution of 1° FWHM introduces noise correlations between pixels, and these are not accounted for in the noise description. The overall χ^2 distribution will therefore be broader than a corresponding distribution with no correlated noise. To estimate the effective number of degrees of freedom, we therefore fit a scaled χ^2 distribution to the empirical χ^2 distribution, including only the very cleanest parts of the sky, where actual foreground contamination is minimal. We adopt the conservative PM61 mask for this. The resulting best-fit χ^2 distribution reads

$$\chi^2_{20.3}(x) \propto \left(\frac{x}{1.37}\right)^{20.3/2-1} \mathrm{e}^{-\frac{x}{2}}, \tag{18}$$

and we accordingly estimate that the empirical number of degrees of freedom is 20, and the correlated noise scaling factor is 1.37. The former of these suggests that our model effectively contains $32-20 = 12$ free parameters, not 14 as obtained by naively counting free parameters per pixel. In other words, the combined effect of all priors is to remove 2 of 14 degrees of freedom, indicating that the model is indeed highly data driven. he latter number suggests that the white noise approximation underestimates the true noise level by 37%. The 99% confidence χ^2 range from the analytic fit is $11 < \chi^2 < 59$.

The middle panel of Fig. 22 shows the mask obtained by thresholding the χ^2 map smoothed with a 1° Gaussian kernel at a value of 50.[14] This mask is called the 93% likelihood mask (LM93), and constitutes the primary confidence mask for the *Planck* 2015 model. Also, together with the CMB solution in Fig. 7, this mask defines the main inputs to the *Planck* 2015 low-ℓ CMB temperature likelihood (Planck Collaboration XI 2016). We note that this mask removes many bright extragalactic point sources at high Galactic latitudes; the algorithm adopted in this paper treats point sources and diffuse emission identically through pixel-by-pixel fits, and any subsequent analysis of the resulting component maps should take these sources into account either through explicit masking, as done here, or by post-processing fits.

The second column of Table 8 lists the rms of each residual map outside the LM93 mask. The third column lists the ratio between these rms values and the corresponding instrumental noise rms, as listed in Table 1. The fourth column shows the monopole and dipole corrected median fractional

[14] Because of the additional smoothing, $\chi^2_{\mathrm{smooth}} > 50$ corresponds roughly to a 5σ outlier, not 2.5σ as it does in the unsmoothed χ^2 map.

Table 7. Posterior mean and rms values for spatially constant parameters in the temperature model.

Quantity	Detectors or Band	Value
Synchrotron freq scale factor, α	. . .	0.26^b
Spinning dust secondary peak freq, ν_p^{sd2} . . .	. . .	$33.35\,\mathrm{GHz}^b$
CO $J = 1 \rightarrow 0$ line ratio	100-ds1	1^a
	100-ds2	1.02 ± 0.01
CO $J = 2 \rightarrow 1$ line ratio	217-1	1^a
	217-2	1.07 ± 0.01
	217-3	1.15 ± 0.01
	217-4	1.18 ± 0.01
CO $J = 3 \rightarrow 2$ line ratio	353-ds2	1^a
	353-1	1.3 ± 0.1
94/100 GHz line ratio	100-ds1	1^a
	100-ds2	1.4 ± 0.3
	W1	4.6 ± 3.2
	W2	4.2 ± 2.9
	W3	5.3 ± 3.7
	W4	4.3 ± 3.0

Notes. The uncertainties of the synchrotron frequency scaling factor and the secondary spinning dust peak frequency are strongly dominated by modelling errors that are difficult to quantify properly, and are omitted here; see main text for further discussion. The quoted line ratios refer to amplitudes relative to the respective reference band. [(a)] Reference channel. [(b)] Only the maximum-likelihood value is provided; see main text.

residual, $(\boldsymbol{d}_\nu - \boldsymbol{s}_\nu)/(\boldsymbol{d}_\nu - \mathsf{T}_\nu \boldsymbol{m}_\nu)$, this time evaluated inside the LM93 mask. As seen in the third column, the rms values of the residual map are close to the instrumental noise for most channels, indicating an excellent goodness-of-fit, not only in terms the integrated χ^2, but also channel-by-channel.

In accordance with the above discussion, we see that a number of channels have residuals that are lower than the instrumental noise, with the 408 MHz and 857-2 channels being the two most striking examples. This is expected, because the χ^2 only has 20 degrees of freedom, whereas there are 32 individual frequency channels; the normalized mean residuals must therefore sum to less than one per channel. However, a ratio much smaller than unity typically indicates that the corresponding channel has a much higher effective signal-to-noise ratio with respect to some signal parameter than all other channels combined. In our case, the 408 MHz and 857-2 channels strongly dominate the synchrotron and thermal dust amplitudes, respectively. At first sight, one might suspect these values to indicate the presence of worrisome parameter degeneracies, which typically also can result in residuals lower than the instrumental noise. However, from the parameter maps shown in Figs. 7–19, it is visually obvious that the synchrotron and thermal dust emission amplitude maps are not degenerate with any components. Rather than degeneracies, these low residual values indicate that the current data set is *non-redundant* with respect to these two amplitude maps; the 408 MHz map determines almost exclusively the synchrotron amplitude, and the 857-2 map determines almost exclusively the thermal dust amplitude. The main problem with these low residuals is therefore not degeneracies, but rather lack of robustness with respect to systematics; any systematic error that may be present in the 408 MHz and 857-2 channels can and will propagate into the respective foreground amplitude maps. In order to improve on this situation in the future, recovering the currently systematics contaminated 857-1, 857-3, and 857-4 channels is

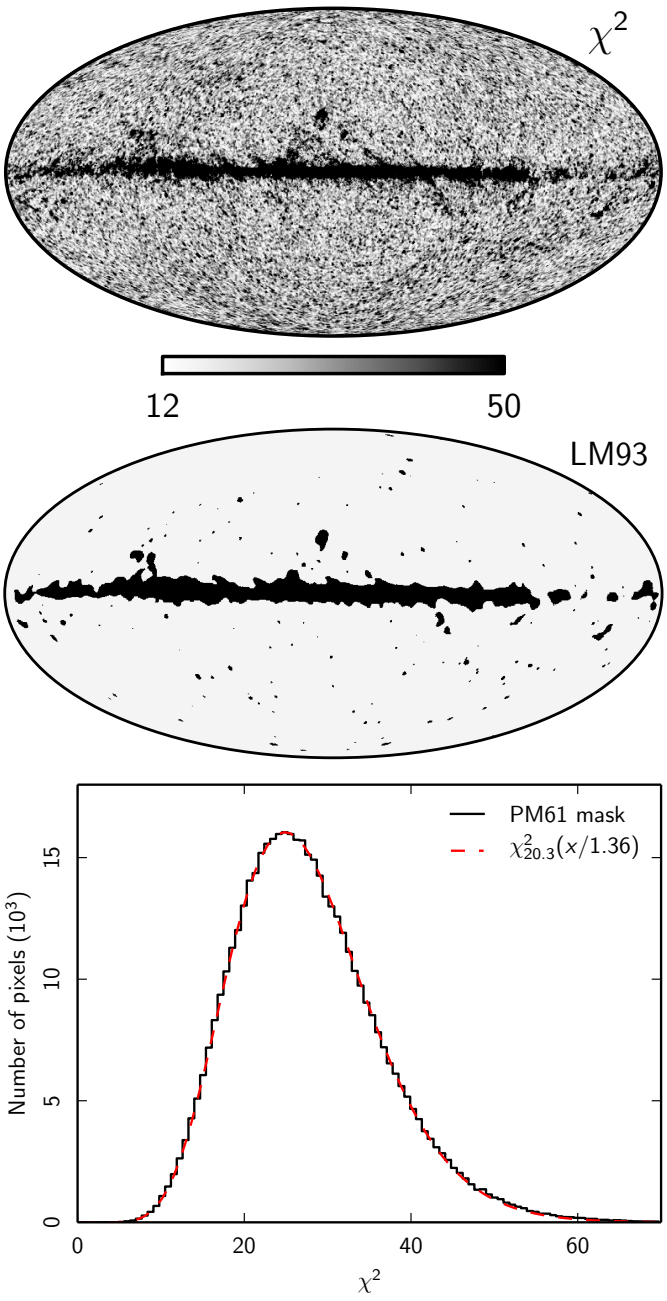

Fig. 22. *Top*: χ^2 per pixel for joint baseline *Planck*, WMAP, and 408 MHz intensity analysis. *Middle*: confidence mask derived by smoothing the χ^2 map to 1° FWHM, and thresholding at a value of $\chi^2_{\mathrm{max}} = 50$. Its primary application is for the low-ℓ 2015 *Planck* temperature likelihood, and it is accordingly denoted LM93 (93% likelihood mask); see Planck Collaboration XI (2016) for further details. *Bottom*: histogram of χ^2 values outside the conservative PM61 mask. The grey dashed line shows the best-fit χ^2 distribution with a variable degree of freedom and scaling, used to account for prior and noise modelling effects; see Sect. 5.3 for further discussion.

imperative on the high-frequency side, and incorporating additional low-frequency observations (between, say, 1 and 20 GHz) is critical on the low-frequency side.

A similar effect is seen for a number of other channels, if not equally strongly. For instance, we see that the WMAP K-band and *Planck* 30 GHz channels have rms ratios of 0.38 and 0.55, respectively, and these dominate the two spinning dust amplitudes, A_{sd1} and A_{sd2}. The 100-ds2 channel has a ratio of 0.76,

Table 8. Goodness-of-fit statistics for the temperature analysis evaluated at 1° FWHM.

Map	Rms outside LM93 [μK]	Rms outside LM93 $\sigma_\nu^{\rm res}/\sigma_\nu^{\rm inst}$	Frac. res. inside LM93 [%]
Planck 30	1.56	0.55	0.08
44	2.51	0.83	0.42
70-ds1	3.67	0.96	0.78
70-ds2	3.88	0.97	0.82
70-ds3	3.98	0.97	0.80
100-ds1	1.00	1.11	0.18
100-ds2	0.61	0.76	0.08
143-ds1	0.72	1.02	0.08
143-ds2	0.68	0.97	0.08
143-5	1.03	1.14	0.15
143-6	1.17	1.06	0.12
143-7	1.04	1.04	0.10
217-1	1.70	0.94	0.06
217-2	1.90	1.00	0.09
217-3	1.68	0.98	0.08
217-4	1.64	0.91	0.05
353-ds2	4.28	0.95	0.03
353-1	2.11	0.60	0.02
545-2	8.89[a]	0.88	0.14
545-4	9.04[a]	0.90	0.13
857-2	1.39[a]	0.13	0.00
WMAP K	2.26	0.38	0.03
Ka	4.52	1.05	0.56
Q1	5.22	0.98	0.64
Q2	5.09	0.99	0.67
V1	6.29	0.98	1.70
V2	5.62	1.02	1.37
W1	7.90	0.89	1.44
W2	9.74	0.96	1.74
W3	9.57	0.90	1.67
W4	10.15	1.00	1.77
Haslam 0.408	0.12[b]	0.10	0.03

Notes. The second column shows the rms residual outside the 93% `Commander` likelihood mask for each channel, while the third column shows the same, but normalized with respect to the instrumental noise rms listed in Table 1. The fourth column lists the median fractional residual in the complementary 7% of the sky, covering the Galactic plane region. [(a)] Unit is kJy sr^{-1}. [(b)] Unit is K.

and defines the CO $J = 1 \rightarrow 0$ amplitude together with 100-ds1. Finally, the 353-1 channel has a ratio of 0.60, and this channel has the greatest pull on the dust emissivity index, $\beta_{\rm d}$.

The single most important conclusion from Table 8, however, is that the baseline *Planck* temperature sky model is an excellent fit to the observed data, in agreement with the visual impression of Fig. 21. The residuals are largely consistent with instrumental noise over 93% of the sky, and the median fractional residual in the complementary 7% of the sky is; smaller than 0.2% for all HFI channels; smaller than 1% for all LFI channels; and smaller than 2% for all WMAP channels.

5.4. High-resolution component maps

We now consider the high-resolution intensity maps derived using the same pipeline as above, but with a reduced data set and astrophysical model. Specifically, we only include channels from 143 GHz and above, all smoothed to a common resolution of 7.′5 FWHM. The signal model includes CMB, thermal dust, and CO $J = 2 \rightarrow 1$ and $3 \rightarrow 2$ emission lines coadded into one map, similar to the Type-3 map in the 2013 data release[15]. We fix all global instrumental parameters on the values listed in Table 6, and the thermal dust temperature, $T_{\rm d}$, to the low-resolution solution, upgraded in harmonic space (to avoid pixelization effects) to a `HEALPix` resolution of $N_{\rm side} = 2048$. The only free spectral parameter per pixel is now the thermal dust emissivity index, $\beta_{\rm d}$.

The resulting amplitude maps are shown in the top panels of Figs. 23–25, while the bottom panels show the so-called half-ring half-difference maps, i.e., half-difference between two maps derived from independent half-ring maps (Planck Collaboration VI 2016; Planck Collaboration VIII 2016); these provide a direct estimate of the instrumental noise present in the full-mission maps. Figure 26 shows the same for the high-resolution dust spectral index.

We note that while the Galactic centre appears negative in the low-resolution CMB solution shown in Fig. 7, it appears positive in the corresponding high-resolution CMB shown in Fig. 23. This qualitative difference demonstrates the importance of modelling errors in the Galactic plane. At high resolution, our model includes only CMB, CO and thermal dust, but no dedicated low-frequency component. Any residual free-free contributions to frequencies at or above 143 GHz is therefore necessarily interpreted as a combination of CMB and CO, both of which have redder spectral shapes than thermal dust. In the low-resolution solution, on the other hand, the main problem lies in the interplay between CO and thermal dust modelling errors and high-frequency calibration uncertainties.

5.5. Comparison with independent data products

To further validate the baseline model presented in Sect. 5.3, we now compare the derived products with similar maps produced either by independent observations or through different analysis techniques, focusing in particular on spinning and thermal dust and CO emission. Synchrotron and free-free (and spinning dust) are addressed separately in a dedicated companion paper, and we refer the interested reader to Planck Collaboration XXV (2016) for full details. A short summary of that analysis includes the following main points.

1. The synchrotron estimates derived by the WMAP team (Bennett et al. 2013) using either Markov chain Monte Carlo (MCMC) or maximum entropy methods (MEM) typically have 50–70% higher amplitudes at high Galactic latitudes compared to that derived in this paper, and this increases to factors of several when including the Galactic plane. This is compensated by about twice as much spinning dust in our model compared to the WMAP models.
2. The free-free model derived in the current analysis correlates well with Hα observations. For instance, the scaling factor between the two maps in the Gum Nebula is $(8.2 \pm 1.3)\,\mu{\rm K\,R^{-1}}$. For comparison, Dickinson et al. (2003) found values ranging between 8.2 and 13.1 $\mu{\rm K\,R^{-1}}$, depending on the exact position within the Gum Nebula.
3. The free-free map also shows good morphological agreement with respect to radio recombination line (RRL) observations (Alves et al. 2015), although the derived amplitude is notably higher in our map. The six brightest objects have a mean relative amplitude ratio of 1.14 ± 0.04, whereas the ten next have an amplitude ratio of 1.36 ± 0.08. Considering that RRLs are in principle a very clean probe of free-free

[15] Although our high-resolution CO map formally is a weighted avarage of $J = 2 \rightarrow 1$ and $J = 3 \rightarrow 2$ line emission, the former vastly dominates, and we therefore refer to the map as CO $J = 2 \rightarrow 1$.

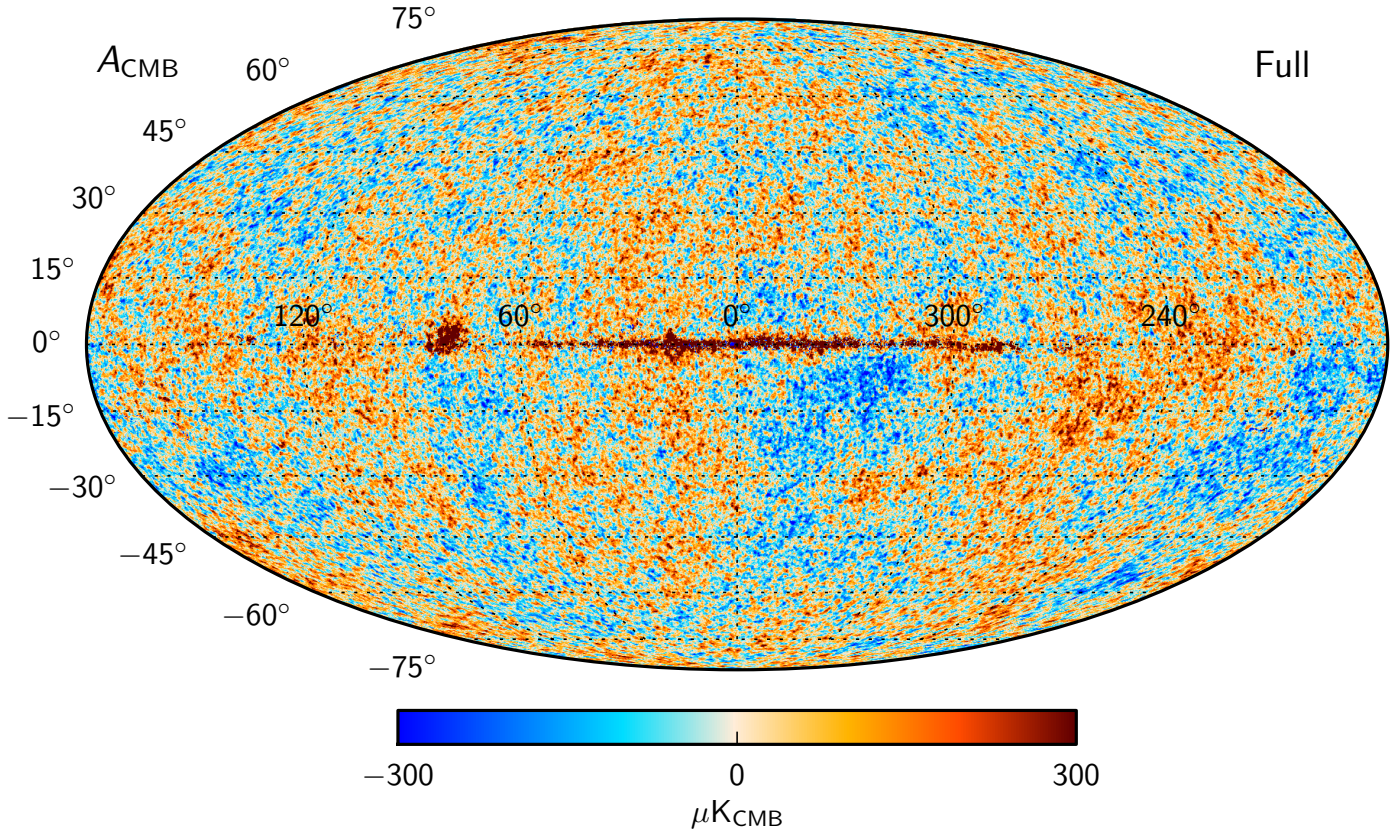

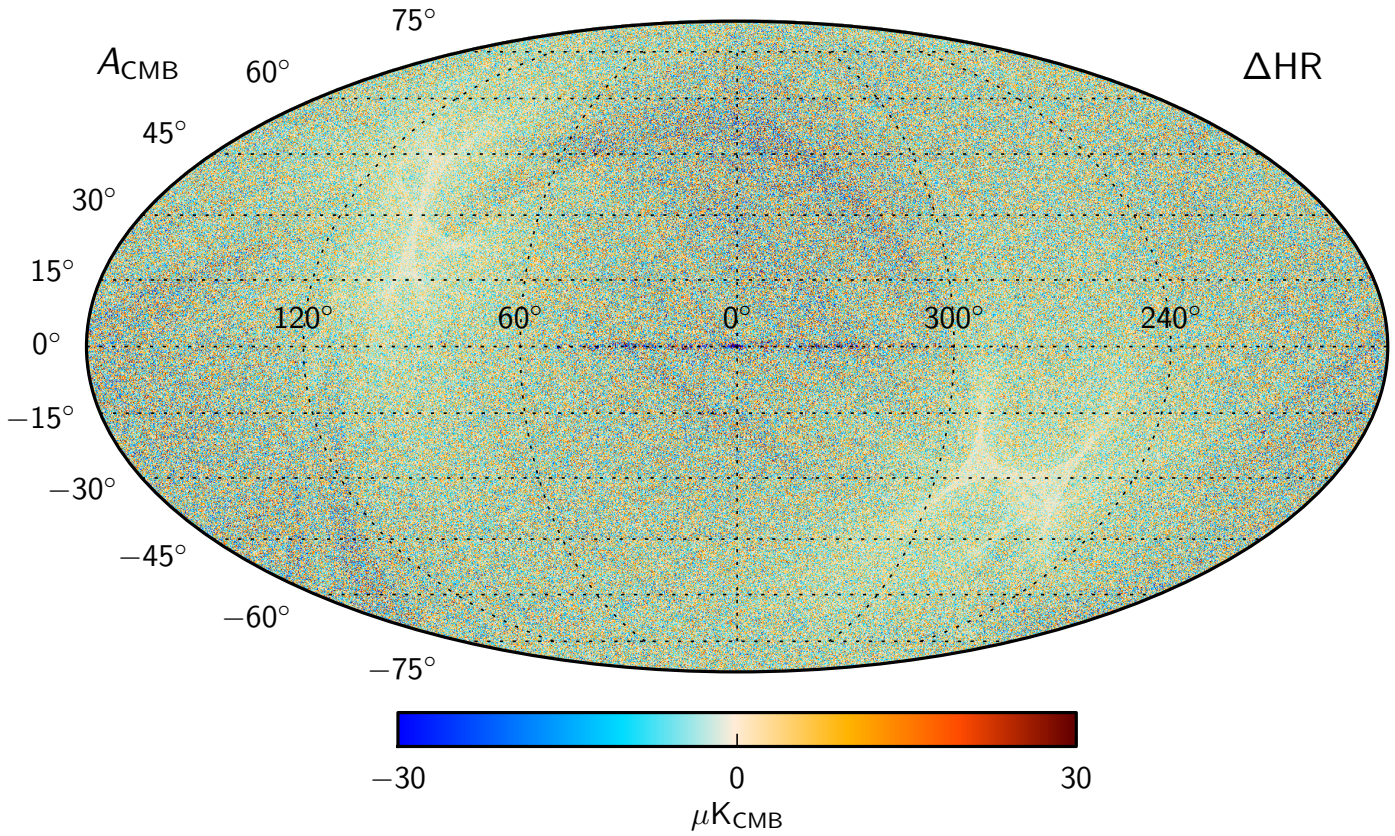

Fig. 23. High-resolution maximum-posterior (*top*) and half-ring half-difference (*bottom*) CMB amplitude maps. The latter provides an estimate of the instrumental noise in the primary map in the top panel. Both panels employ linear colour scales.

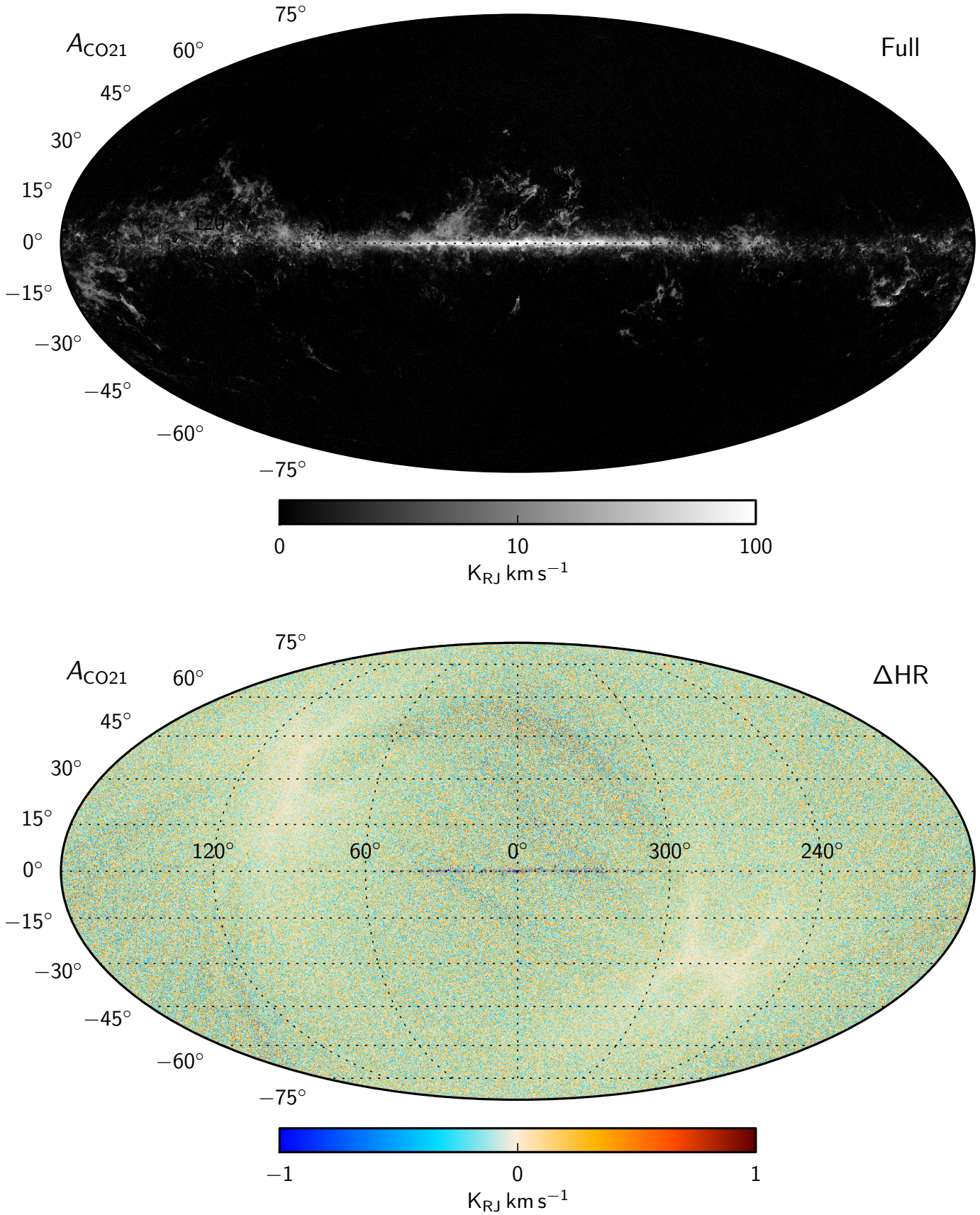

Fig. 24. High-resolution maximum-posterior (*top*) and half-ring half-difference (*bottom*) CO $J = 2 \rightarrow 1$ amplitude maps. The latter provides an estimate of the instrumental noise in the primary map in the top panel. Note that the top panel employs a non-linear high dynamic range colour scale, while the bottom panel employs a regular linear colour scale.

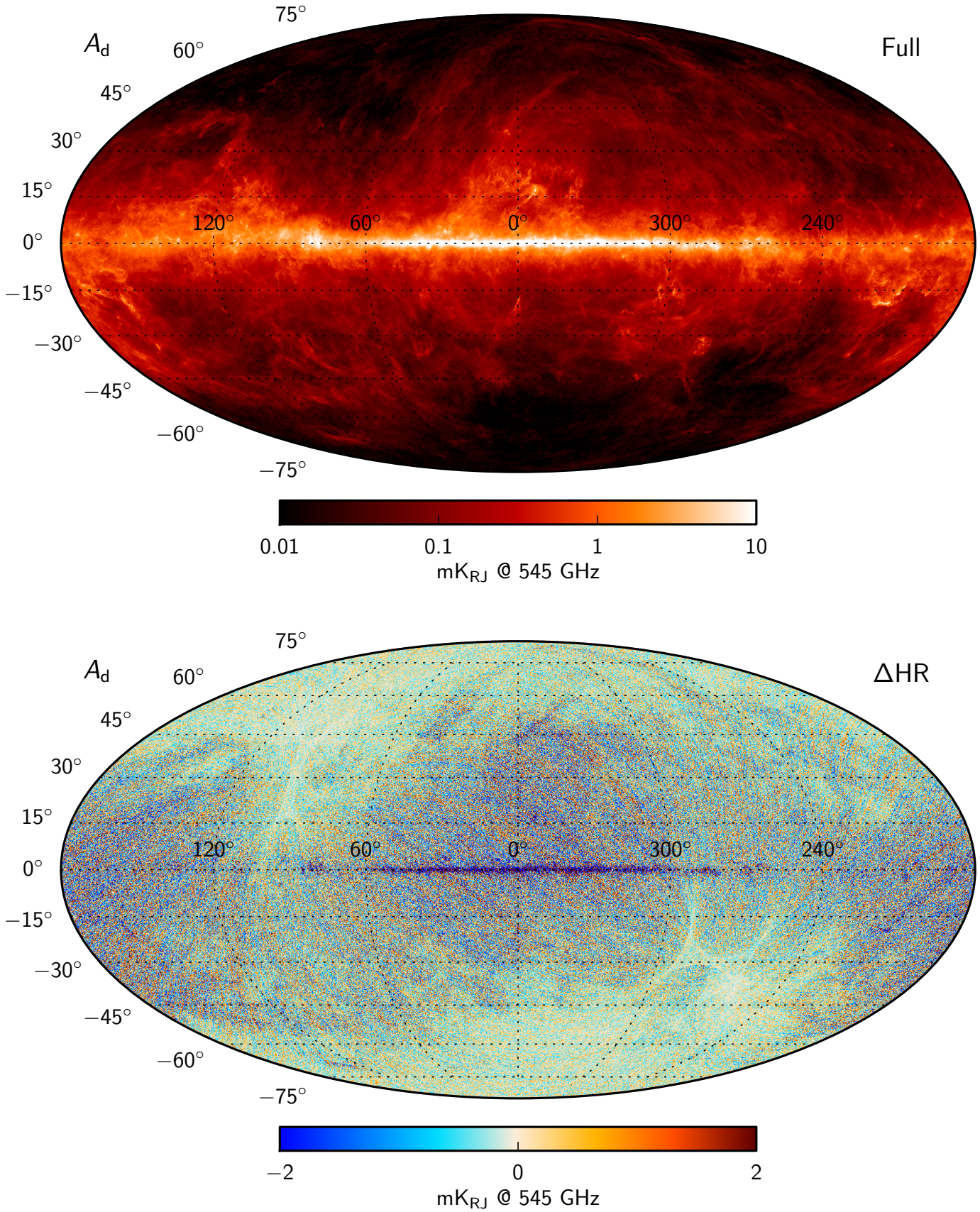

Fig. 25. High-resolution maximum-posterior (*top*) and half-ring half-difference rms (*bottom*) thermal dust amplitude maps. The latter provides an estimate of the instrumental noise in the primary map in the top panel. Note that the top panel employs a non-linear high dynamic range colour scale, while the bottom panel employs a regular linear colour scale.

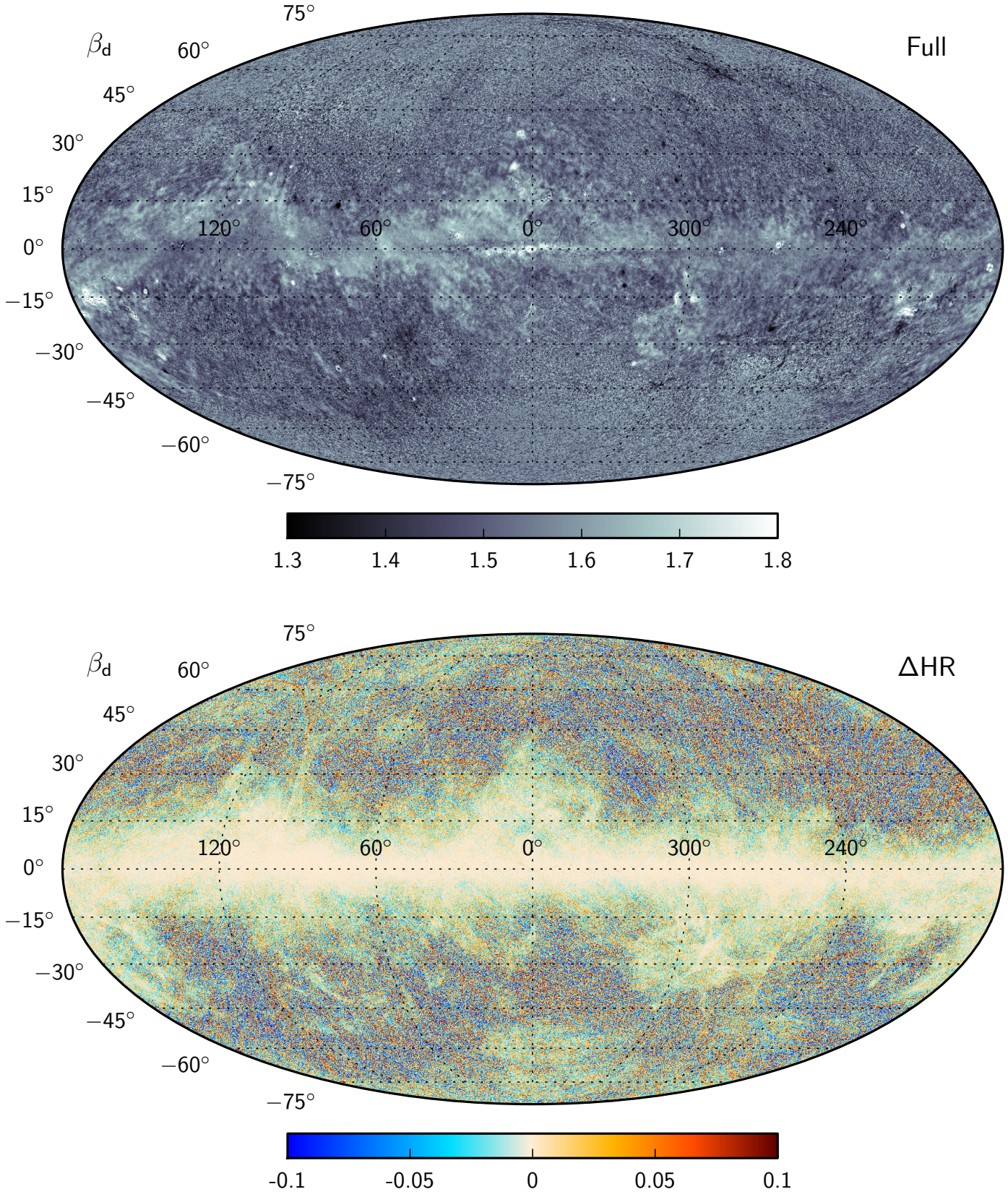

Fig. 26. High-resolution maximum-posterior (*top*) and half-ring half-difference rms (*bottom*) thermal dust spectral index maps. The latter provides an estimate of the instrumental noise in the primary map in the top panel. Both panels employ linear colour scales.

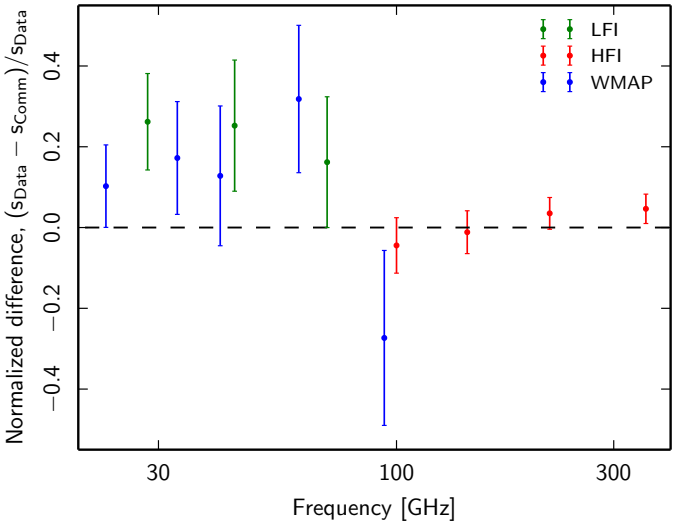

Fig. 27. Fractional difference between the template amplitudes derived when fitting the GASS H I survey data at high Galactic latitudes to: (1) the raw *Planck* and WMAP temperature maps; and to (2) the sum of the spinning and thermal dust models derived by Commander in this paper.

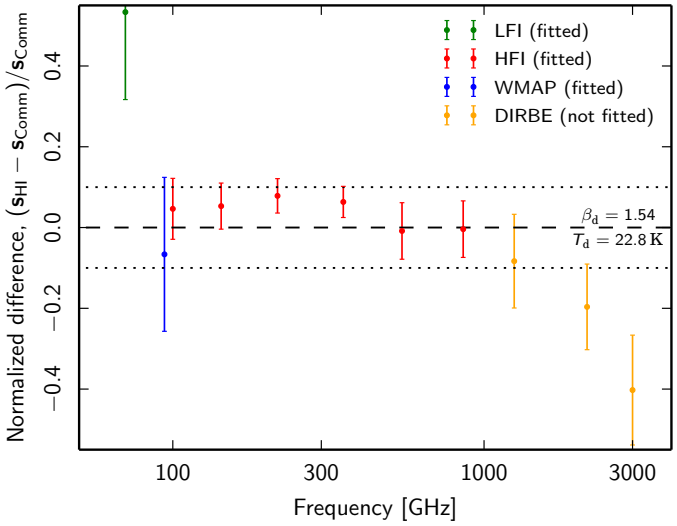

Fig. 28. Fractional difference of the mean thermal dust SEDs as derived by cross-correlation with the GASS H I survey data at high Galactic latitudes, updated with the latest *Planck* 2015 temperature sky maps, (Planck Collaboration Int. XVII 2014) and by Commander in this paper. The dotted horizontal lines indicate fractional differences of ±10 %. For comparison purposes, we also show the extrapolation to the 100, 140, and 240 μm DIRBE frequencies. These observations are not included in the fits performed in this paper; see Sect. 5.5.2 for further discussion.

emission, the most likely explanation for this discrepancy is leakage between synchrotron, spinning dust, CO, and free-free in the current solution. On the other hand, the derived RRL amplitudes also depends sensitively on the assumed electron temperature, and raising $/Te$ by ≈20% would resolve much of the difference. In addition, it is worth noting that other component separation techniques, including FastMEM, CCA, and both the 9-yr WMAP MCMC and MEM analyses, all derive free-free amplitudes consistent with the Commander result (Planck Collaboration Int. XXIII 2015).

5.5.1. Dust template amplitude consistency by H I cross-correlation

We next perform an internal consistency test of the Commander dust model in the range from 23 to 353 GHz, as defined by the sum of the SpDust2 components described in Sect. 4.1 and thermal dust, by cross-correlating our dust model against GASS H I observations (McClure-Griffiths et al. 2009; Kalberla et al. 2010) covering 18% of the high Galactic latitude sky near the South Galactic pole, following the procedure of Planck Collaboration Int. XVII (2014). In particular, we compare the resulting template amplitudes against the corresponding amplitudes derived directly from cross-correlation with the raw *Planck* and WMAP sky maps.

Figure 27 shows the fractional difference between the resulting template amplitudes for each frequency band. Overall, the agreement is satisfactory with typically 20% differences in the 20–70 GHz range, in which spinning dust provides a larger contribution to the frequency spectrum than thermal dust. At higher frequencies, where thermal dust emission starts to dominate, the agreement improves further to around 5%, and to within 1 σ in terms of statistical uncertainties.

5.5.2. Dust SED consistency by H I and internal *Planck* cross-correlations

Next, we consider the robustness and consistency of the thermal dust SED model, as parametrized in terms of the two greybody parameters, β_d and T_d. Specifically, we compare the new SED estimates derived in this paper with corresponding estimates derived by H I cross-correlation at high latitudes in Planck Collaboration Int. XVII (2014), and by internal *Planck* cross-correlations at intermediate Galactic latitudes in Planck Collaboration Int. XXII (2015), both of which have been updated with the latest *Planck* 2015 sky maps.

Figure 28 compares the mean thermal dust SED derived from H I–CMB cross-correlation and the Commander estimates at high Galactic latitudes in terms of the fractional difference, $(s_{HI} - s_{Comm})/s_{Comm}$. The two sets of best-fit thermal dust spectral parameters are $(\beta_d, T_K)_{Comm} = (1.54, 22.8\,K)$ and $(\beta_d, T_K)_{HI} = (1.54, 21.4\,K)$, respectively, and the two models agree point-by-point to 5–10% between 100 and 857 GHz. At 70 GHz the difference is 50%, and this is due to different spinning dust modelling; as already shown in Fig. 27, the sum of spinning and thermal dust agree to 20% in this range between the two methods. Note also that 70 GHz is very close to the foreground minimum, and these numerically large relative differences therefore correspond to small absolute differences.

This test provides a robust estimate of residual systematic errors in the Commander thermal dust model from potential zero-level and dipole uncertainties in the high-frequency HFI channels arising from zodiacal light emission and CIB residuals, as discussed in Sect. 3. Because the H I analysis is insensitive to such errors, we take the 1–2 K difference between the two as an estimate of the systematic uncertainty on the Commander thermal dust temperature at high Galactic latitudes.

At frequencies above 857 GHz we also plot the extrapolation of the new Commander model into the *COBE*-DIRBE wavelengths of 240, 140, and 100 μm (Hauser et al. 1998). Here we clearly see that the current model breaks down beyond the *Planck* frequencies, with a fractional difference of 40% between the Commander model and the DIRBE 100 μm observations. Including the DIRBE channels in the fit would of course reduce these fractional residuals dramatically, but only at a very significant cost of increasing the residuals at lower frequencies

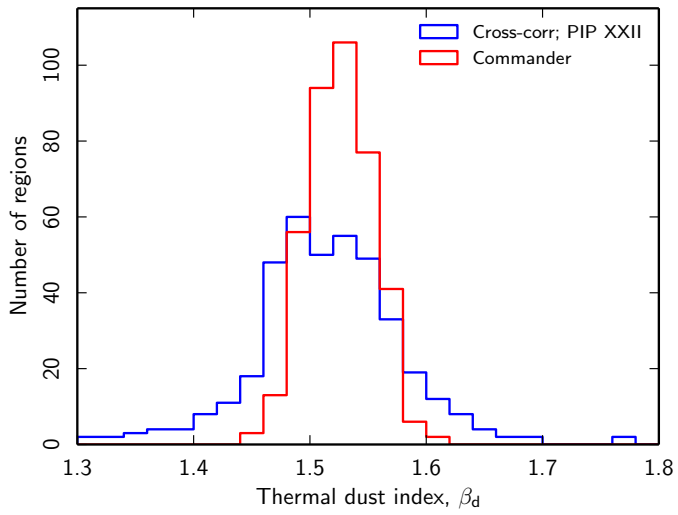

Fig. 29. Comparison of the thermal dust spectral index, β_d, estimated by internal *Planck* map cross-correlations over HEALPix $N_{side} = 8$ pixels in Planck Collaboration Int. XXII (2015) and those presented in this paper. The best-fit Gaussian distributions to the two histograms have mean and standard deviations of $\beta_d^{Comm} = 1.53 \pm 0.03$ and $\beta_d^{cross\text{-}corr} = 1.51 \pm 0.06$, respectively.

between 70 and 353 GHz. The simple one-component greybody thermal dust model adopted in this paper is not able to simultaneously fit this entire frequency range, because of both intrinsic complexity of the dust particle population and because of residual systematics and calibration uncertainties in the DIRBE and high-frequency *Planck* data. Integration of these channels requires substantial additional work, and is beyond the scope of the current paper. For a first analysis of similar type, see Planck Collaboration Int. XXIX (2016).

Next, we turn to intermediate Galactic latitudes, for which the signal-to-noise ratio is higher, but also the astrophysical composition is richer. In this case we therefore compare our results with the outputs from the internal *Planck* template cross-correlation analysis of Planck Collaboration Int. XXII (2015). In short, this analysis estimates the SED parameters by cross-correlating the *Planck* 353 GHz channel with lower frequencies over circular patches of 10° radius. Figure 29 compares the histogram of β_d derived using this method with the corresponding Commander estimates over the same sky region. The agreement is very good, and with averages and dispersions of $\beta_d^{Comm} = 1.53 \pm 0.03$ and $\beta_d^{cross\text{-}corr} = 1.51 \pm 0.06$, respectively. When interpreting the widths of these distributions, it is useful to return to the thermal dust spectral index maps shown in Figs. 17 and 26. These maps are quite uniform, and, indeed, at the current level of leakage between thermal dust, CO, compact objects and residual offsets, there is little convincing evidence for true spatial variation in β_d in the results presented here. If this conjecture is true, the widths of the histograms shown in Fig. 29 are primarily expressions of analysis uncertainties in the form of instrumental noise, parameter degeneracies and systematic errors, rather than true spatial variation.

5.5.3. CO line emission

Finally, we compare the CO $J = 1 \rightarrow 0$, $2 \rightarrow 1$ and $3 \rightarrow 2$ maps derived in Sects. 5.3 and 5.4 with independently derived maps and products. As described in Planck Collaboration XIII (2014), *Planck* has implemented a multi-algorithm approach to CO extraction, configuring the MILCA (Hurier et al. 2013) and Commander algorithms for dedicated CO reconstruction. In 2013, this resulted in three different types of CO maps. In short, the Type-1 CO maps are built from individual bolometer maps within single frequencies, and as such are only weakly dependent on foreground extrapolations, but this insensitivity comes at a high cost in terms of instrumental noise. The Type-2 maps are built per CO line from a small sub-set of frequencies, carefully selected to be optimal for CO extraction. Since more than one frequency is involved, a more elaborate foreground model is required, such as explicit modelling of CMB, dust and free-free, although several simplifications are imposed, such as the assumption of constant dust temperature and spectral indices. Finally, the Type-3 map corresponds to a maximum signal-to-noise CO extraction in which a complete foreground model is fitted with Commander, as described in this paper, but with only a single CO amplitude per pixel and otherwise only spatially fixed line ratios accounting for scaling between frequencies.

In the present release, the MILCA-based Type-1 and Type-2 maps have been updated with the latest data, while the Commander-Ruler-based Type-3 map from 2013 has been superseded by the high-resolution Commander-only $J = 2 \rightarrow 1$ map presented in Sect. 5.4. In addition to these high-resolution maps, we of course also provide the low-resolution line maps discussed in Sect. 5.3. Table 9 summarizes the CO-related data products provided in the current release, including angular resolution, instrumental noise, and analysis assumptions.

We start by comparing the maps derived with MILCA and Commander, both with each other and with the CO $J = 1 \rightarrow 0$ survey presented by Dame et al. (2001). The full-sky $J = 1 \rightarrow 0$ and $2 \rightarrow 1$ maps are shown in Figs. 30 and 31, while zoom-ins of the Orion region are shown in Fig. 32. All maps are smoothed to a common resolution of 15′ in these plots, except the Dame et al. survey, which has an intrinsic resolution of about 20′. For reference, the 2013 Type-3 map is shown in the bottom panel of Fig. 30.

The first three panels of Fig. 33 show T–T correlation plots between each of the three CO line maps and the Dame et al. survey, all smoothed to a common resolution of 1° FWHM; the fourth panel shows similar correlations between the high- and low-resolution *Planck* products. Please note that all axes are linear, and this figure therefore highlights the very brightest CO objects on the sky. The main points to take away from these scatter plots, and the maps in Figs. 31 and 32, are the following.

1. The Type-2 and low-resolution Commander $J = 1 \rightarrow 0$ maps agree very well internally, and also correlate strongly with the Dame et al. survey. However, they both show an overall multiplicative scaling factor of about 1.4 relative to Dame et al. This level of amplitude difference is similar to what was observed in the 2013 release (Planck Collaboration XIII 2014), and is due to a combination of bandpass uncertainties in the *Planck* observations and the overall 10% calibration uncertainty in the Dame et al. survey. The Type-1 $J = 1 \rightarrow 0$ map shows bigger differences with respect to the Dame et al. survey, both in the scatter plot and the Orion zoom-in. Possible explanations include the presence of a second significant line emission mechanism, such as ^{13}CO $J = 1 \rightarrow 0$ (at 110 GHz), or, possibly, thermal dust leakage.
2. In the CO $J = 2 \rightarrow 1$ case, the Type-2 map shows some evidence of contamination, both in the form of significant curvature in the scatter plot (top right panel of Fig. 33), and as notable diffuse emission along the Galactic plane in the Orion region and full-sky map. The agreement between the

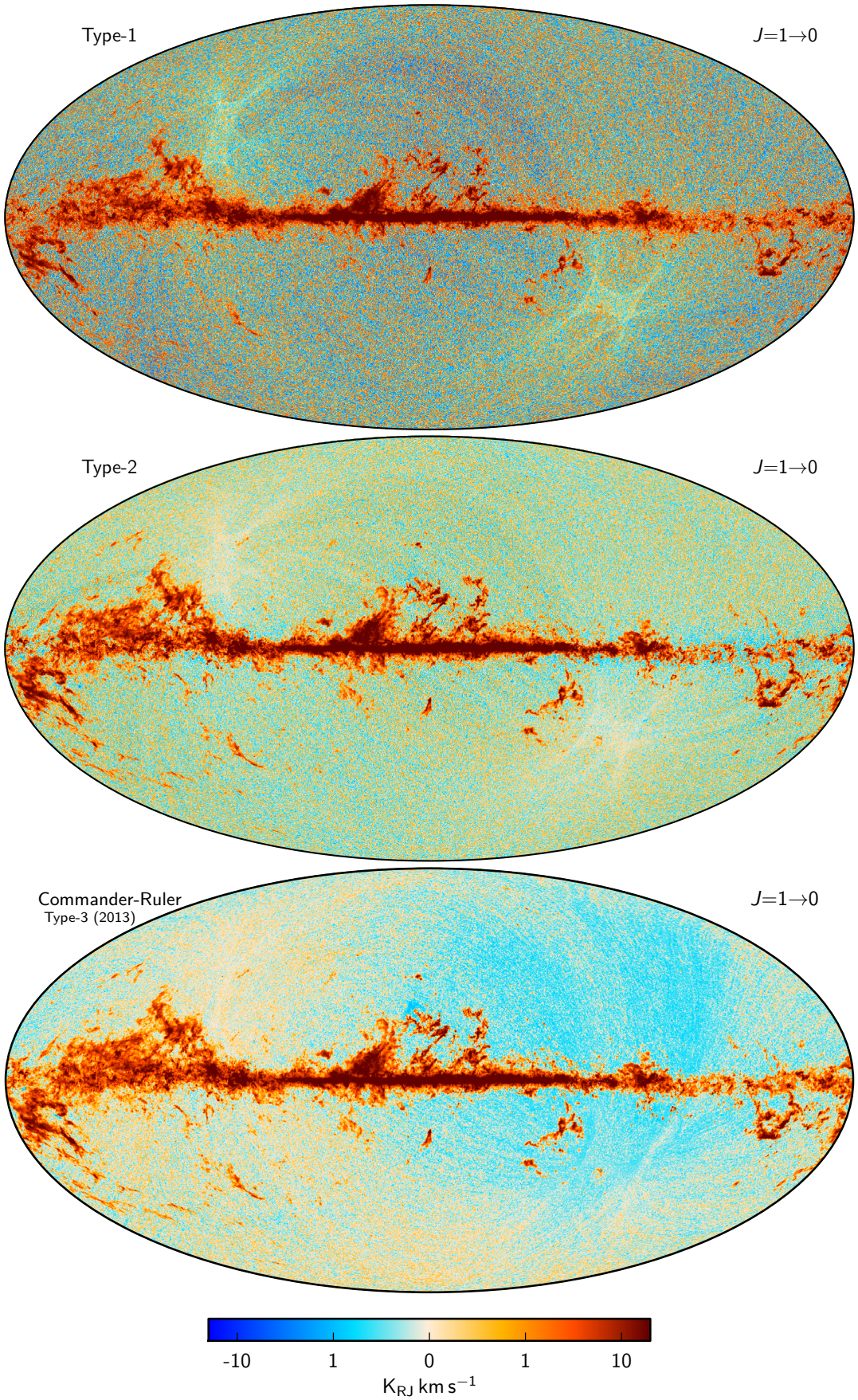

Fig. 30. High-resolution CO $J = 1 \rightarrow 0$ maps derived from the 2015 *Planck* sky maps with two different algorithms, denoted Type-1 (*top row*) and Type-2 (*middle row*); and derived from the 2013 *Planck* sky maps with `Commander-Ruler` (*bottom row*). Details can be found in Planck Collaboration XIII (2014). All maps are smoothed to a common resolution of 15′ FWHM.

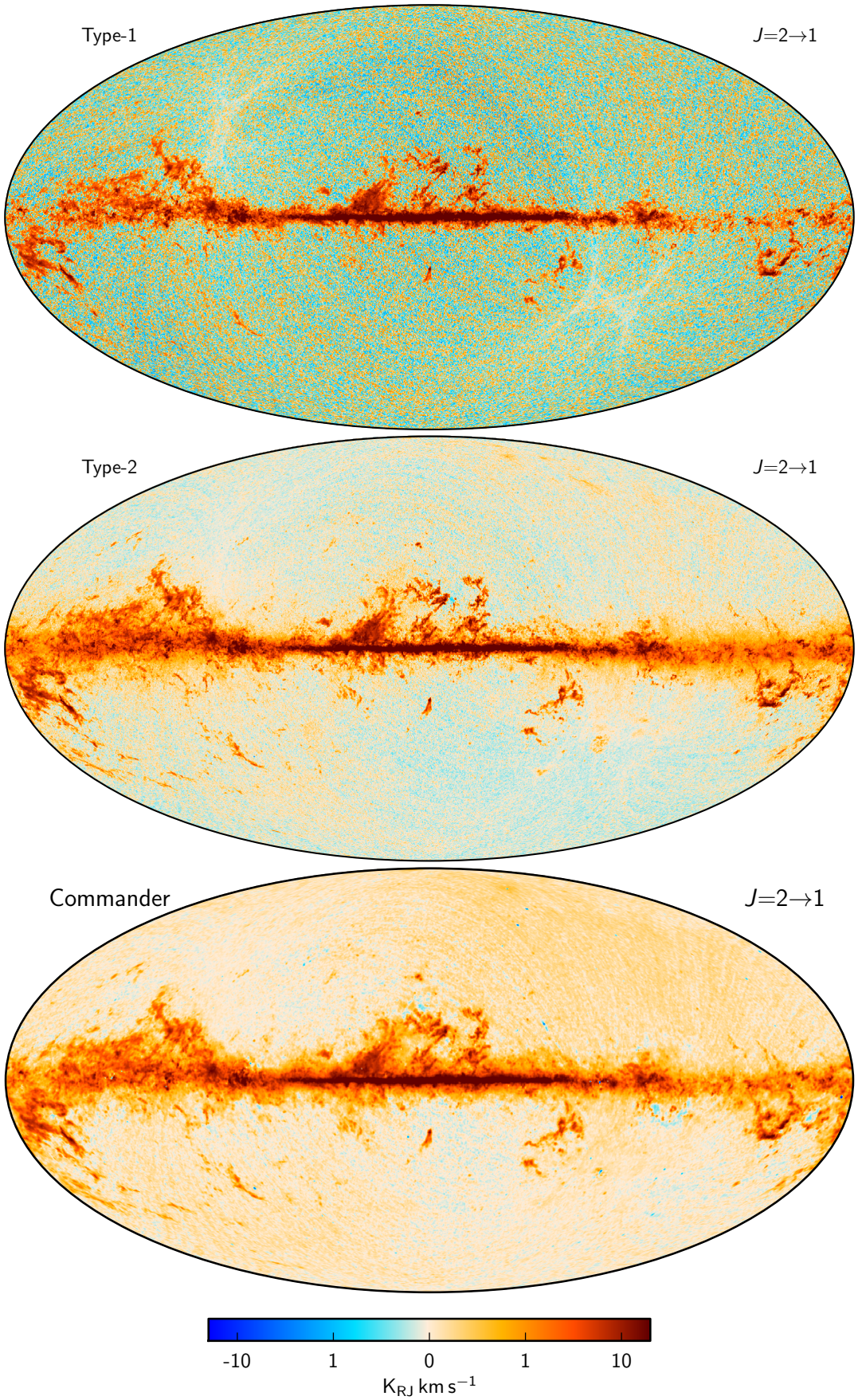

Fig. 31. High-resolution CO $J = 2 \rightarrow 1$ maps derived from the 2015 *Planck* sky maps with three different algorithms, denoted Type-1 (*top row*), Type-2 (*middle row*) and `Commander` (*bottom row*), see Planck Collaboration XIII (2014) for details. All maps are smoothed to a common resolution of 15′ FWHM.

Table 9. Summary of main CO product characteristics.

Map	Algorithm	CO line	Resolution [arcmin]	Noise rms [K_{RJ} km s^{-1}]		Analysis details	
				15′ *FWHM*	60′ *FWHM*	Frequencies [GHz]	Model
Type 1	MILCA	$J=1\rightarrow0$	9.6	1.4	0.34	100 (bol maps)	CO, CMB
	MILCA	$J=2\rightarrow1$	5.0	0.53	0.16	217 (bol maps)	CO, CMB, dust
	MILCA	$J=3\rightarrow2$	4.8	0.55	0.18	353 (bol maps)	CO, dust
Type 2	MILCA	$J=1\rightarrow0$	15	0.39	0.085	70, 100, 143, 353	CO, CMB, dust, free-free
	MILCA	$J=2\rightarrow1$	15	0.11	0.042	70, 143, 217, 353	CO, CMB, dust, free-free
	Commander	$J=1\rightarrow0$	60	···	0.084	0.408–857	Full; see Sect. 5
	Commander	$J=2\rightarrow1$	60	···	0.037	0.408–857	Full; see Sect. 5
	Commander	$J=3\rightarrow2$	60	···	0.060	0.408–857	Full; see Sect. 5
Type 3	Commander	$J=2\rightarrow1^{a}$	7.5	0.090	0.031	143–857	CO, CMB, dust
	Commander-Ruler	$J=1\rightarrow0^{b,c}$	5.5	0.19	0.082	30–353	CO, CMB, dust, low-freq

Notes. [(a)] Formally a weighted average of CO $J=2\rightarrow1$ and $J=3\rightarrow2$, but strongly dominated by CO $J=2\rightarrow1$. [(a)] Formally a weighted average of CO $J=1\rightarrow0$, $J=2\rightarrow1$ and $J=3\rightarrow2$, but strongly dominated by CO $J=1\rightarrow0$. [(c)] Only published in 2013.

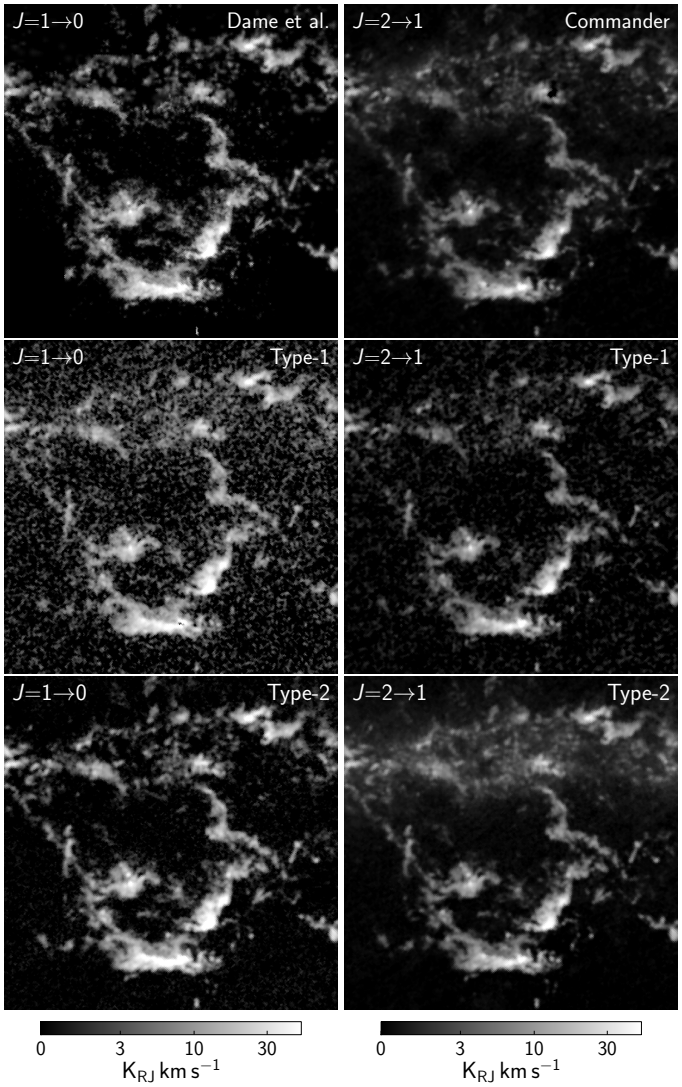

Fig. 32. 30° × 30° zoom-in of various CO emission line maps in a Galactic gnomonic projection; the Galactic north pole points up in each panel. All maps smoothed to 15′ FWHM and centred on the Orion region, with Galactic coordinates $(l, b) = (201°, -9°)$.

Type-1 and Commander maps is, however, good, and both show tight correlations with the Dame et al. survey.

3. For the CO $J=3\rightarrow2$ map, the scatter with respect to Dame et al. is substantial for both Type-1 and Commander, and in particular the latter shows clear evidence of curvature in the T–T plot due to contamination from thermal dust.
4. A significant residual dipole aligned with the CMB dipole may be seen in the 2013 Type-3 map, and similar residuals are also present in the 2013 Type-1 and Type-2 maps. These dipole residuals have been greatly suppressed in the new 2015 maps, due to the new estimation of the CMB dipole directly from the *Planck* sky maps, as described in Planck Collaboration I (2016).

Figure 34 shows histograms of the various high-resolution maps, each map being smoothed to a common resolution of 15′ FWHM and re-pixelized at a HEALPix level of $N_{side} = 512$. As already noted, here we clearly see that the Type-1 maps have significantly larger instrumental noise (wider histograms near zero) than the corresponding Type-2 and Commander maps. However, we also see that the three maps converge well at intermediate amplitudes between, say, 3 and 200 K_{RJ} km s^{-1}, for both $J=1\rightarrow0$ and $2\rightarrow1$.

Next, in Fig. 35 we compare the Type-2 and Commander $J=2\rightarrow1$ maps with targeted CO $J=1\rightarrow0$ high-latitude observations published by Hartmann et al. (1998) and Magnani et al. (2000). The same test was performed for the *Planck* 2013 CO maps, and full details regarding methodology and data processing can be found in Planck Collaboration XIII (2014). The top panel shows a T–T scatter plot between each of their 133 detected objects and the corresponding objects in our maps. The correlation is strong for both Type-2 and Commander, and with comparable effective line ratios in the two cases. The bottom panel shows histograms including positions for which Hartmann/Magnani et al. did not find any significant CO detections, and, correspondingly, our maps also do not exhibit any detections at these positions; both histograms are consistent with noise.

Finally, as in the 2013 analysis (Planck Collaboration XIII 2014), we have also cross-correlated the Type-1, Type-2, and Commander $J=2\rightarrow1$ maps against the CO $J=2\rightarrow1$ AMANOGAWA-2SB survey (Yoda et al. 2010; Handa et al. 2012), and find very good morphological agreement among all

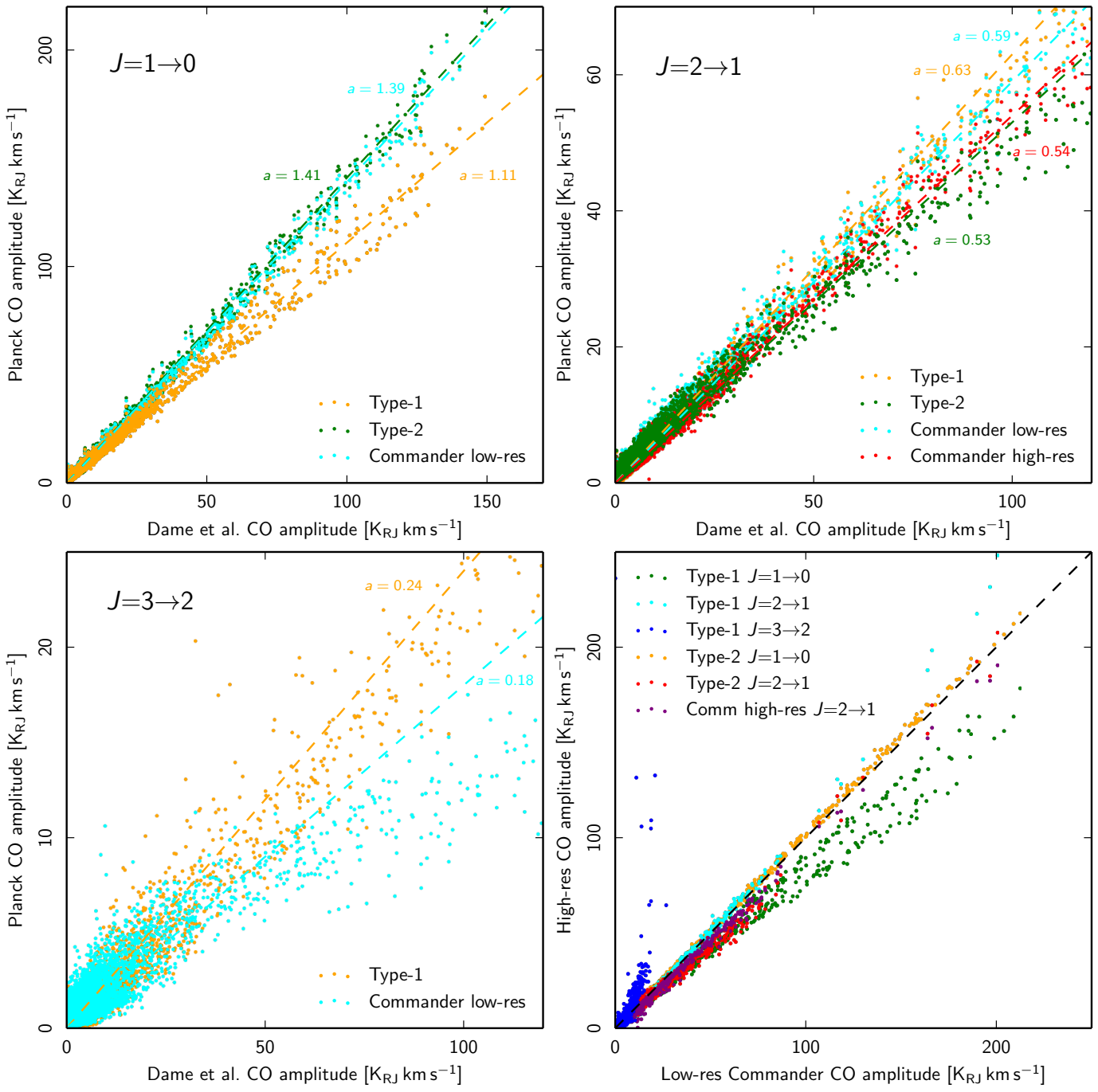

Fig. 33. T–T scatter plots between Type-1, Type-2, `Commander` CO maps and the Dame et al. (2001) CO $J = 1 \rightarrow 0$ map, smoothed to 1° FWHM and pixelized with a `HEALPix` resolution parameter $N_{\rm side} = 64$. The panels show correlations for $J = 1 \rightarrow 0$ (*top left*), $J = 2 \rightarrow 1$ (*top right*) and $J = 3 \rightarrow 2$ (*bottom left*) line maps; the *bottom right panel* show correlations between the baseline 1° FWHM `Commander` CO maps and the (smoothed) Type-1, Type-2 and the high-resolution `Commander` $J = 2 \rightarrow 1$ map.

maps. The best-fit slopes are 0.95, 0.82 and 0.86 for the Type-1, Type-2, and `Commander` maps, respectively. Thus, while the Type-1 CO $J = 2 \rightarrow 1$ map is more noisy than the other two, it is also less affected by dust and free-free contamination, and it is a robust estimation of CO $J = 2 \rightarrow 1$ in the Galactic plane. From this test, we also estimate that the overall re-calibration factors for the Type-2 and `Commander` CO $J = 2 \rightarrow 1$ maps are 15–20%.

Combining all of these results, we make the following recommendations. First, the `Commander` CO $J = 2 \rightarrow 1$ map supersedes the 2013 Type-3 map as the primary "CO detection" map, and is also our preferred CO $J = 2 \rightarrow 1$ map. The main advantages of this map as compared to the Type-2 map are higher angular resolution (7.′5 versus 15′ FWHM), slightly lower noise (0.09 versus 0.11 $\mathrm{K_{RJ}\,km\,s^{-1}}$), and a tighter correlation with respect to the Dame et al. survey (see Fig. 32). However, in specific regions where the signal is such that the noise level of the Type-1 CO $J = 2 \rightarrow 1$ map becomes less of an issue, i.e., in the Galactic plane, the Type-1 map is a better alternative in terms of overall calibration and contamination. For a dedicated $J = 1 \rightarrow 0$ analysis, we recommend the Type-2 map, which has higher angular resolution than the corresponding `Commander` map (15′ versus 1° FWHM), with similar correlation properties with respect

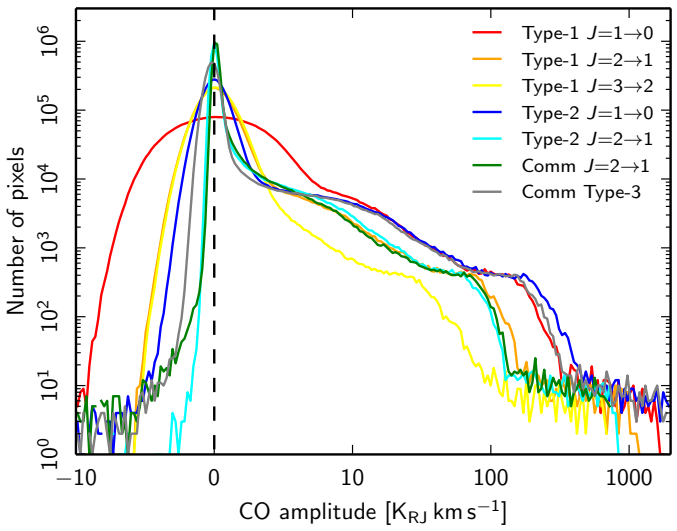

Fig. 34. Pixel histograms of high-resolution CO line emission maps, all smoothed to a common resolution of 15′ FWHM and re-pixelized at `HEALPix` resolution $N_{\rm side} = 512$.

to Dame et al. Finally, for CO $J = 3 \rightarrow 2$ we recommend the Type-1 map, due to a significantly stronger correlation with respect to Dame et al. than the corresponding `Commander` map.

6. Polarization analysis

We now turn our attention to the 2015 *Planck* measurements of polarized foregrounds. As described in Sect. 3, and summarized in Table 1, we employ full co-added frequency maps for this analysis, in order to maximize the signal-to-noise ratio, and we fit only CMB, synchrotron, and thermal dust emission amplitudes, fixing all calibration and spectral parameters to their temperature counter-parts (see Sect. 4.2). The main data products are summarized in the bottom two sections of Table 5.

From an algorithmic point of view, the polarization analysis is essentially identical to the temperature analysis, with the same summary statistics and goodness-of-fit statistics applying equally well to the Stokes Q and U parameters as to the temperature (i.e., Stokes I). We therefore proceed in the same manner as for the temperature case, and first present the main data products, then discuss internal goodness-of-fit tests. However, in this case we additionally discuss the EE and BB angular power spectra for synchrotron and thermal dust emission, recognizing the high importance of these quantities in current cosmology. Finally, we consider external validation.

6.1. Baseline model

We start by presenting the full-sky Stokes Q and U parameter maps for polarized CMB, synchrotron, and thermal dust in Fig. 36, and a 20° × 20° zoom-in of the south ecliptic pole in Fig. 37; corresponding CMB maps of the north ecliptic pole, including decompositions into E and B mode polarization, are shown in Planck Collaboration IX (2016). We note that the CMB map has been high-pass filtered with a cosine-apodized harmonic space filter, removing all structures below $\ell = 20$, in order to suppress large-scale instrumental systematics. Additionally, the Galactic plane has been replaced with a constrained Gaussian realization in order to avoid ringing effects during filtering (see Planck Collaboration IX 2016 for further details).

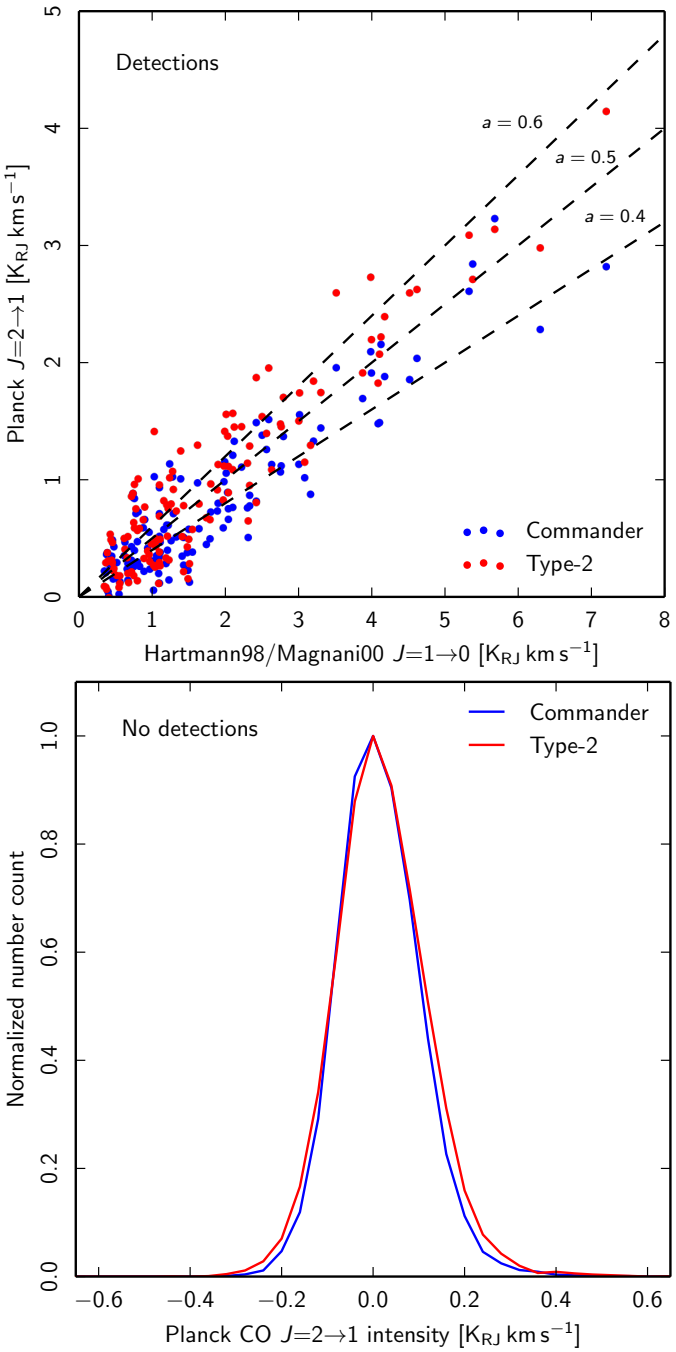

Fig. 35. Comparison of *Planck* CO $J = 2 \rightarrow 1$ maps with the high Galactic latitude CO detections published by Hartmann et al. (1998) and Magnani et al. (2000; *top*), and corresponding amplitude histograms including only positions in which no detections were found in the same surveys (*bottom*).

Figures 38 and 39 show the polarization amplitude and direction, as defined by direct and naive estimators,

$$P = \sqrt{Q^2 + U^2} \tag{19}$$

$$\psi = \frac{1}{2}\,\mathrm{atan}(U, Q). \tag{20}$$

We note that the former of these is a quadratic estimator, and therefore biased by instrumental noise, and the latter is also a nonlinear function. More sophisticated approaches are applied and described in Planck Collaboration Int. XIX (2015), which

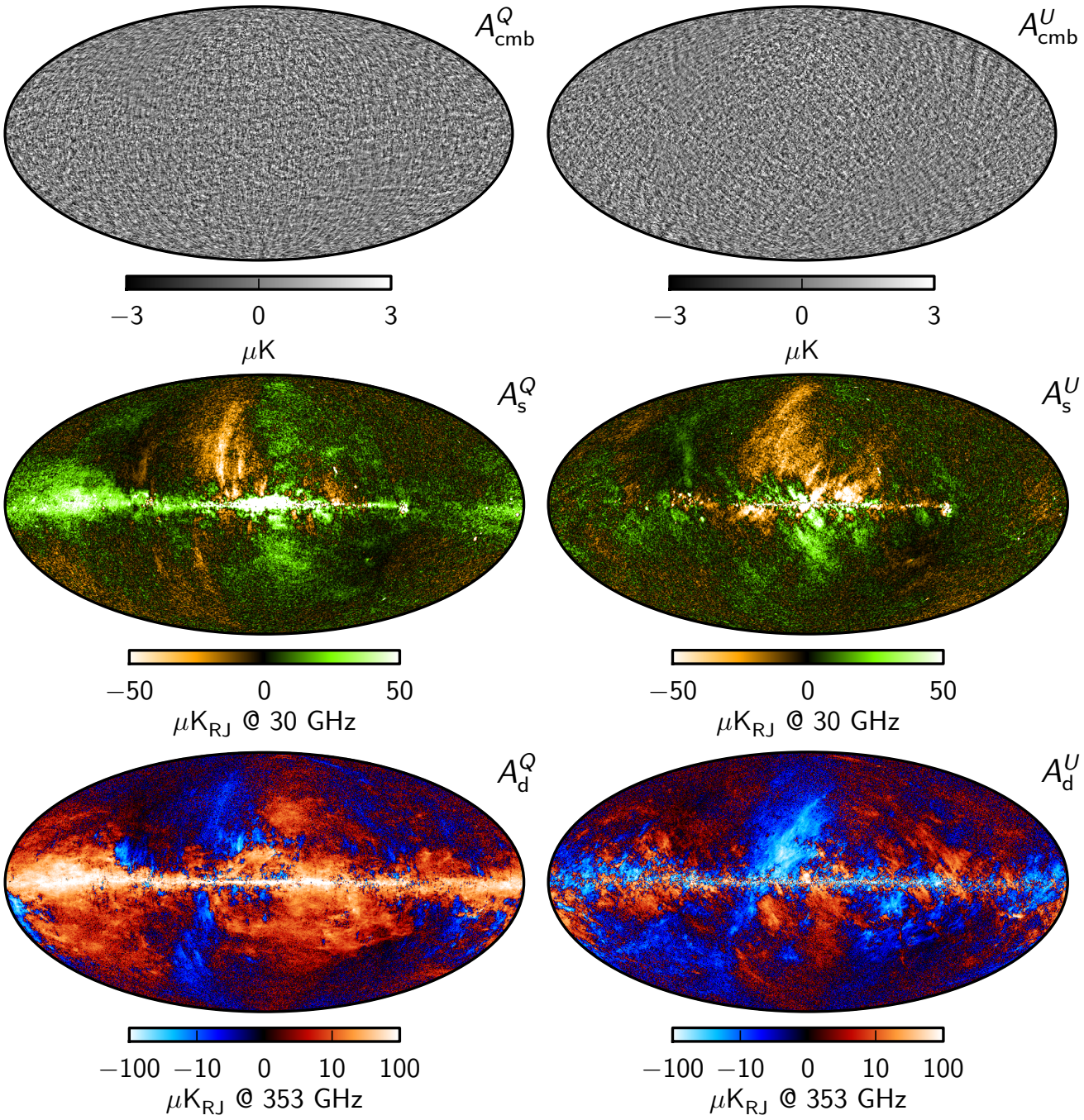

Fig. 36. Maximum posterior amplitude polarization maps derived from the *Planck* observations between 30 and 353 GHz. *Left and right columns* show the Stokes Q and U parameters, respectively, while rows show, *from top to bottom*, CMB, synchrotron polarization at 30 GHz, and thermal dust polarization at 353 GHz. The CMB map has been highpass-filtered with a cosine-apodized filter between $\ell = 20$ and 40, and the Galactic plane (defined by the 17% CPM83 mask shown in Fig. 41) has been replaced with a constrained Gaussian realization (Planck Collaboration IX 2016).

properly accounts for this bias. However, in this paper the main purpose of these quantities is visual interpretation, rather than quantitative model comparisons, and the naive estimators are then useful for providing information regarding both the underlying physical structures and the instrumental noise levels. Specifically, the noise level at a given position on the sky can be inferred from the polarization amplitude maps in Fig. 38 by comparing the intensity of any region to the deep fields near the ecliptic poles, where the *Planck* signal-to-noise ratio is maximum.

Considering first the CMB maps in Fig. 37, it is clear that *Planck* measures primordial polarized anisotropies with high signal-to-noise ratio at 10′ FWHM angular scales. Furthermore, it is also visually obvious that the CMB signal is strongly dominated by primordial E-modes, in the form of a clear +-type pattern in Stokes Q and a ×-type pattern in Stokes U; see Sect. 4.2 for further discussion.

Of course, this particular region of the sky is more deeply observed than any other region on the sky (except the north ecliptic pole), and the apparent high signal-to-noise level seen in the middle of the panel is not representative of the full sky. However, due to very sharply defined features in the *Planck* scanning strategy in this region, the signal seen near the bottom left corner of these plots is indeed representative, within a factor of a few.

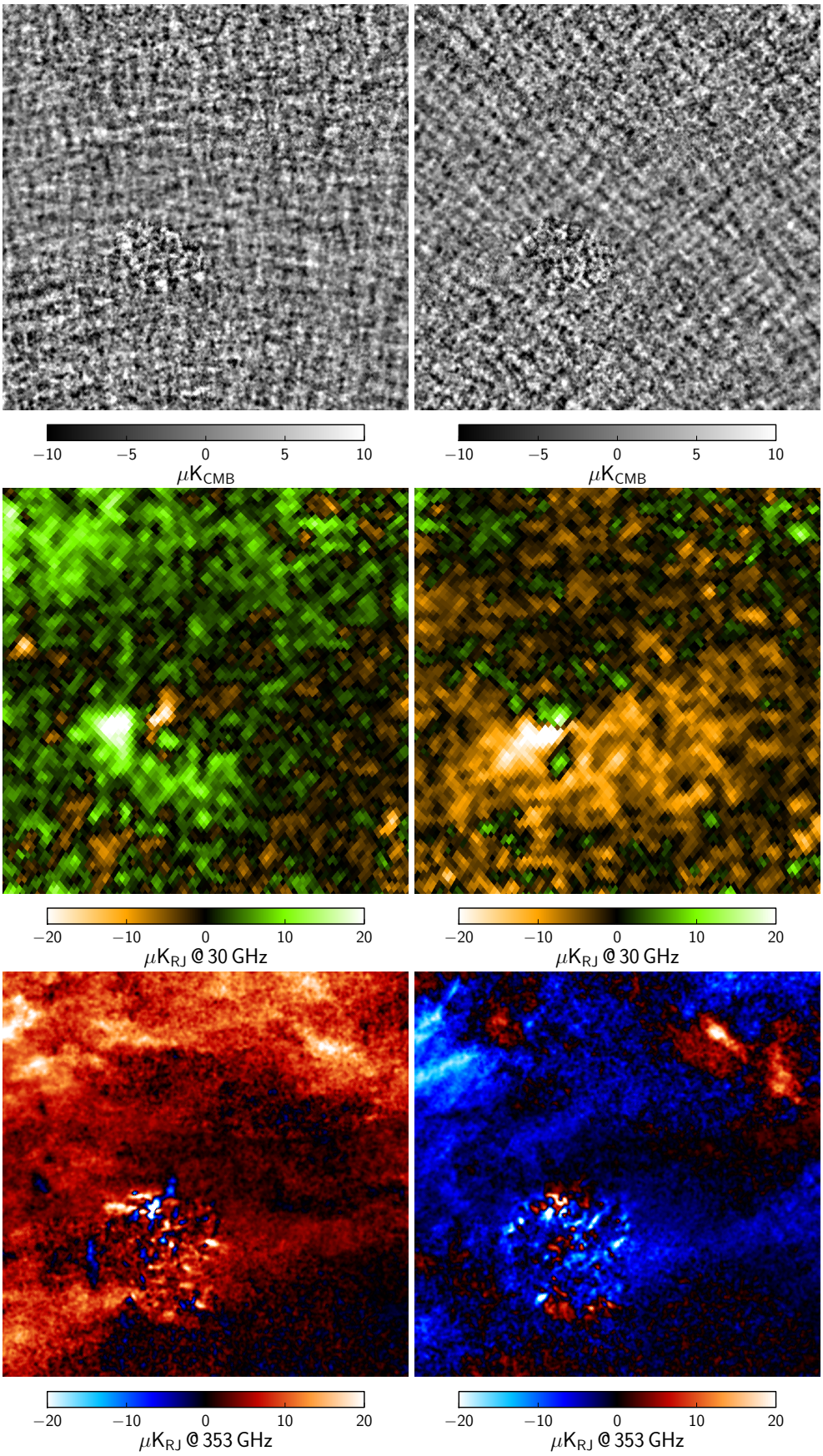

Fig. 37. 20° × 20° polarization zooms centred on the south ecliptic pole with Galactic coordinates $(l, b) = (276°, -30°)$ of CMB (*top row*), synchrotron (*middle row*), and thermal dust emission (*bottom row*). *Left and right columns* show Stokes Q and U parameters, respectively. The object in the lower left quadrant is the Large Magellanic Cloud (LMC).

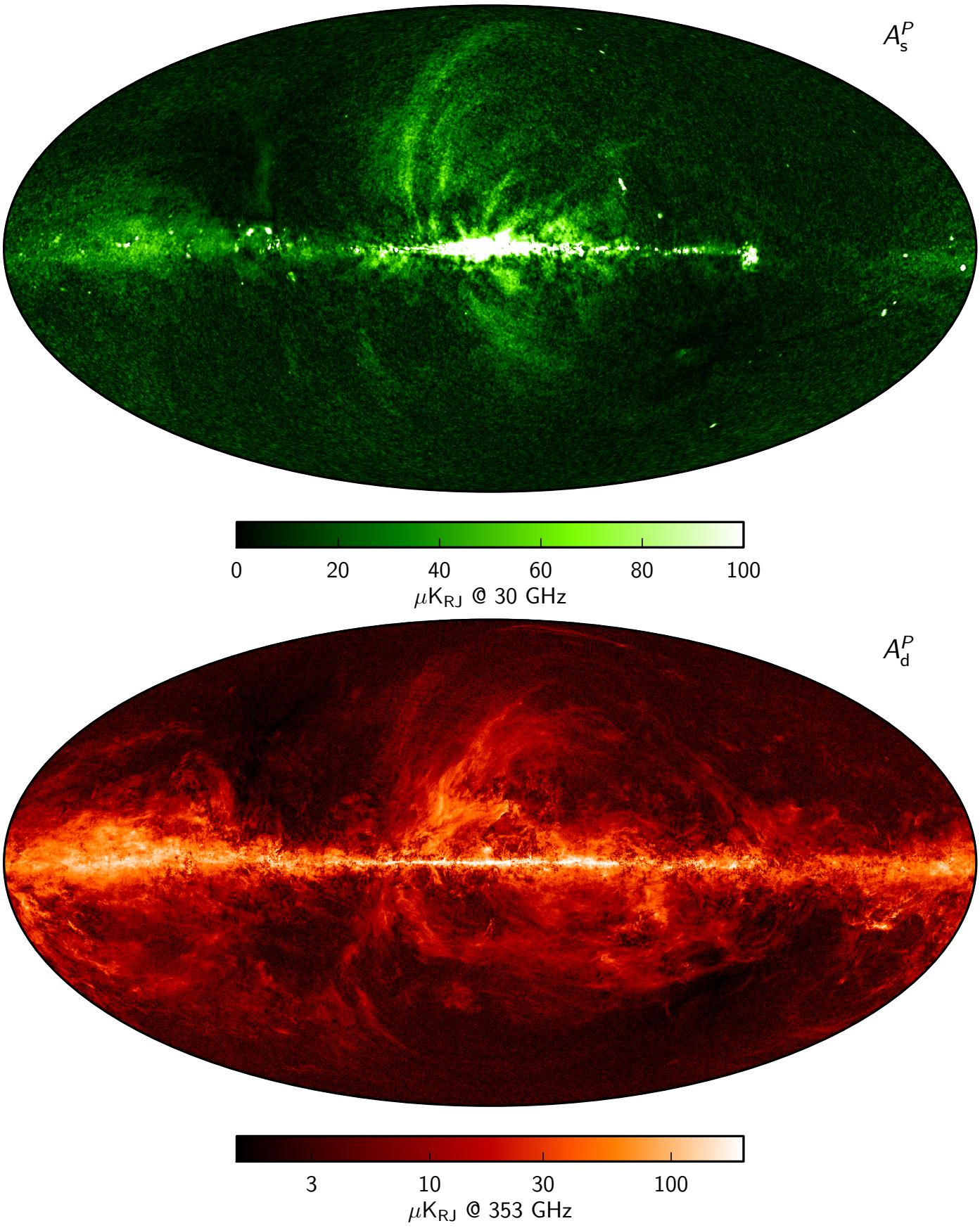

Fig. 38. *Planck* polarization amplitude maps, $P = \sqrt{Q^2 + U^2}$. The *top panel* shows synchrotron emission at 30 GHz, smoothed to an angular resolution of 40′, and the *bottom panel* shows thermal dust emission at 353 GHz, smoothed to an angular resolution of 10′.

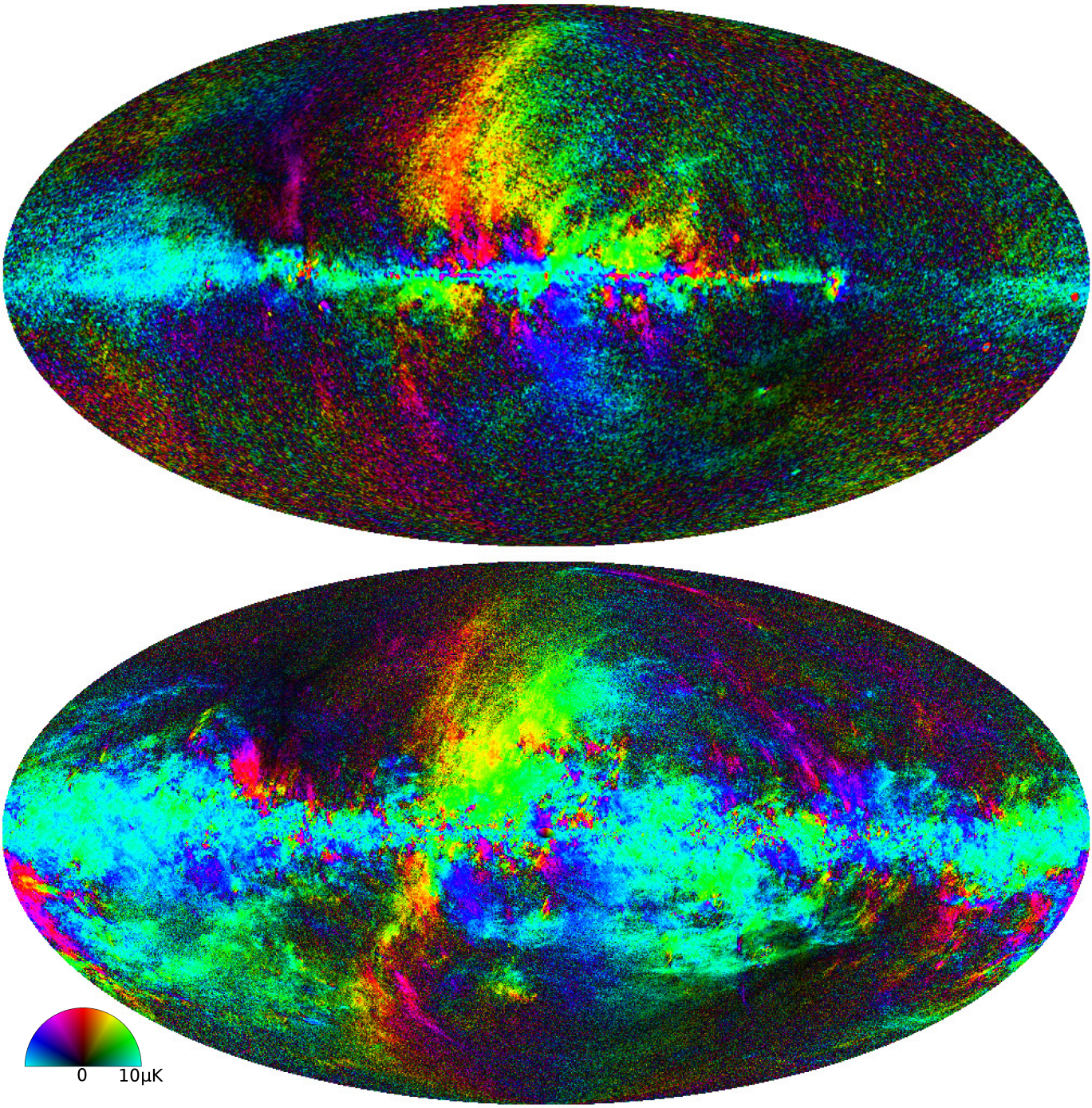

Fig. 39. *Planck* polarization angle maps for synchrotron emission, smoothed to 40′ FHWM (*top*) and thermal dust emission, smoothed to 10′ FWHM (*bottom*). Light blue and red colours indicate polarization angles aligned with meridians ($\psi = 0°$) and parallels ($\psi = 90°$), respectively, while yellow and purple indicate polarization angles rotated by −45 and +45° with respect to the local meridian in the `HEALPix` polarization angle convention. Colours are saturated at $10\,\mu K_{RJ}$.

In the same region, we also clearly see the Large Magellanic Cloud (LMC) in both synchrotron and thermal dust emission (see Planck Collaboration XXV 2016 for a detailed analysis of the LMC), but only very weakly in the CMB maps. Indeed, the primary signature of the LMC is a slight increase in variance rather than a systematic bias. This is quite reassuring in terms of CMB reconstruction fidelity, since the LMC represents one of the richest astrophysical objects on the sky.

In this respect it is worth recalling that we fix all calibration and spectral parameters (thermal dust index and temperature and synchrotron spectrum) in the polarization analysis to those derived in the temperature analysis. Several attempts have been made at re-estimating these parameter independently from the polarization observations, but we find that the resulting parameters invariably become significantly biased by the same large-scale systematics that are responsible for the remaining large-scale residuals in the CMB map (Planck Collaboration II 2016; Planck Collaboration VIII 2016; Planck Collaboration IX 2016). However, other analyses that explicitly exploit spatial correlations (e.g., template fitting) to suppress such systematics have been able to produce robust results, and yield only small differences between the temperature and polarization spectral

indices. For instance, Planck Collaboration Int. XXII (2015) reports full-sky estimates of $\beta_d = 1.51 \pm 0.01$ for intensity and $\beta_d = 1.59 \pm 0.02$ for polarization, corresponding to a difference of only 3.6σ even after averaging over most of the sky. Thus, assuming identical temperature and polarization spectral indicies is a very good approximation at the precision level of the current data, considering the additional stability with respect to instrumental systematic errors it provides.

6.1.1. Goodness-of-fit

We now consider the statistical goodness-of-fit of this simple baseline model, following the same procedure as for the temperature analysis. First, Fig. 40 shows the residual maps $\boldsymbol{d}_\nu - \boldsymbol{s}_\nu$, for each of the seven *Planck* frequency maps, all smoothed to a common resolution of 40′ FWHM angular scale. Please note that the colour range is linear between $\pm 5\,\mu$K, and the same in all panels. As expected, we see that 143 GHz is the most sensitive frequency channel, followed by the 100 and 217 GHz channels. In addition to instrumental noise, these channels also exhibit large-scale patterns tracing the *Planck* scanning strategy at the $\lesssim 0.5\,\mu$K level. Although small in an absolute sense, it is important to recall that the expected peak-to-peak amplitude of a cosmological signal from reionization corresponding to an optical depth of, say, $\tau \approx 0.07$ is also about $0.5\,\mu$K (Planck Collaboration XI 2016). As a result, we do not consider the CMB polarization map presented here suitable for cosmological parameter estimation on large angular scales. Instead, the *Planck* 2015 low-ℓ polarization likelihood relies only on the 30, 70, and 353 GHz data, for which instrumental systematics are subdominant (Planck Collaboration VI 2016; Planck Collaboration VIII 2016; Planck Collaboration XI 2016).

Next, the top panel of Fig. 41 shows the corresponding χ^2 map, co-adding over both frequencies and Stokes parameters. Compared to the temperature case, it is here much easier to determine the appropriate number of degrees of freedom, since no spectral parameters are fitted to the data, and no positivity priors are imposed on the amplitudes. Specifically, there are in total 14 data points (two Stokes parameters in seven frequencies) and 6 free parameters (two Stokes parameters in three components), resulting in a net 8 degrees of freedom. The nominal 95% confidence region for this number of degrees of freedom is $\chi^2 = (2, 17)$.

As usual, the Galactic plane is the most significant feature in the χ^2 map. Furthermore, when comparing this χ^2 map (and the individual frequency residual maps) with the various component amplitude maps derived in the temperature analysis, we find strong correlations between the χ^2 map and the CO emission maps. This is expected from the mapmaking analyses presented in Planck Collaboration XI (2016), and, as already noted, a general recommendation regarding these maps is to reject any pixels with significant CO intensity contribution, because of temperature-to-polarization leakage. The `Commander` polarization mask (CPM) is accordingly defined as the product of the (smoothed and thresholded) χ^2 map shown in the top panel of Fig. 41, and the low-resolution Commander CO $J = 1 \rightarrow 0$ intensity map thresholded at $0.5\,\mathrm{K_{RJ}\ km\,s^{-1}}$. The resulting mask is shown in the middle panel of Fig. 41, and excludes 17% of the sky.

The bottom panel of Fig. 41 shows a histogram of the χ^2 values outside the CPM83 mask, with the best-fit χ^2 distribution with variable number of degrees of freedom and width, fully analogous to the temperature case in Sect. 5.3. In this case, the best-fit distribution has 7.9 degrees of freedom, in excellent agreement with the theoretical expectation of 8, while the width rescaling factor that accounts for correlated noise and smoothing is 1.15, indicating that the white noise approximation underestimates the noise by 15% due to correlations.

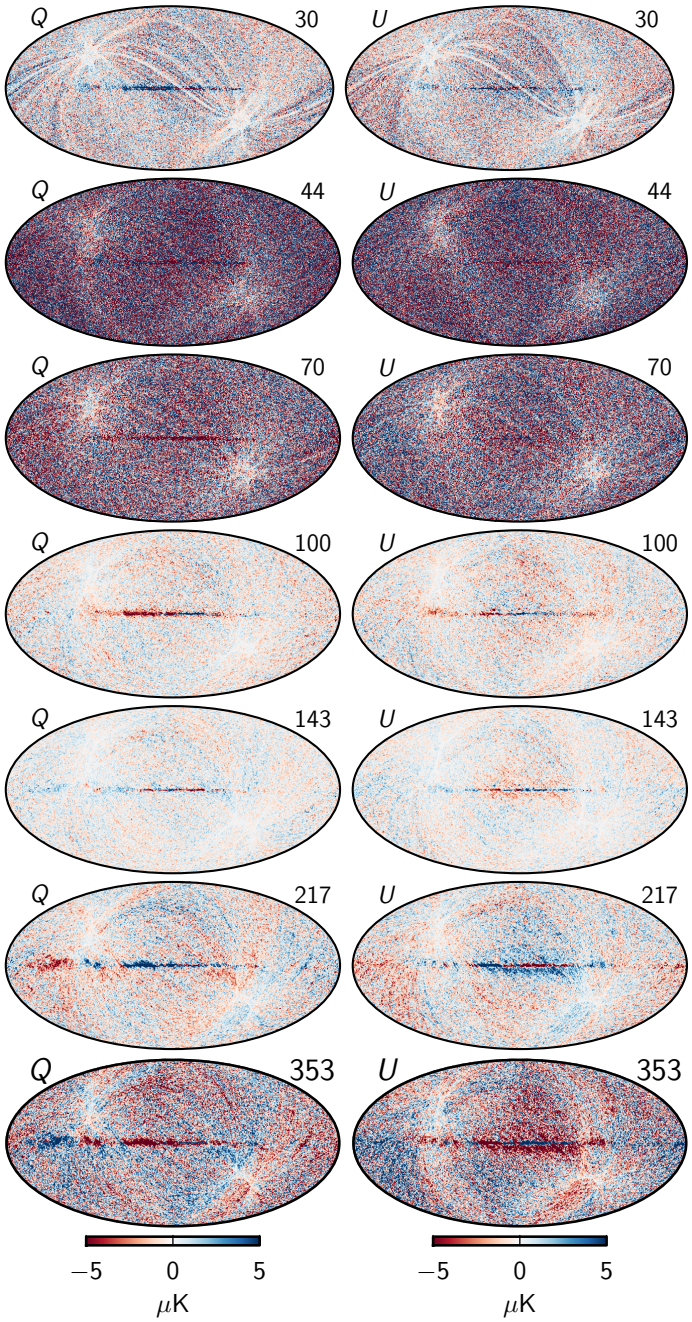

Fig. 40. Polarization residual maps, $\boldsymbol{d}_\nu - \boldsymbol{s}_\nu$. Each row corresponds to one frequency map, with 30 GHz in the *top row* and 353 GHz in the *bottom row; left and right columns* show the Stokes Q and U parameters, respectively. All panels employ the same linear colour scale.

Table 10 lists the rms of the residual maps for each frequency, analogous to Table 8 for temperature, averaged over the two Stokes Q and U parameters. The third column in this table shows the ratio between these rms values and instrumental noise; again, we observe good agreement with expectations. As for the temperature case, the values for the 30 and 353 GHz channels are significantly lower than unity, because these two frequencies dominate the synchrotron and thermal dust amplitude parameters, respectively.

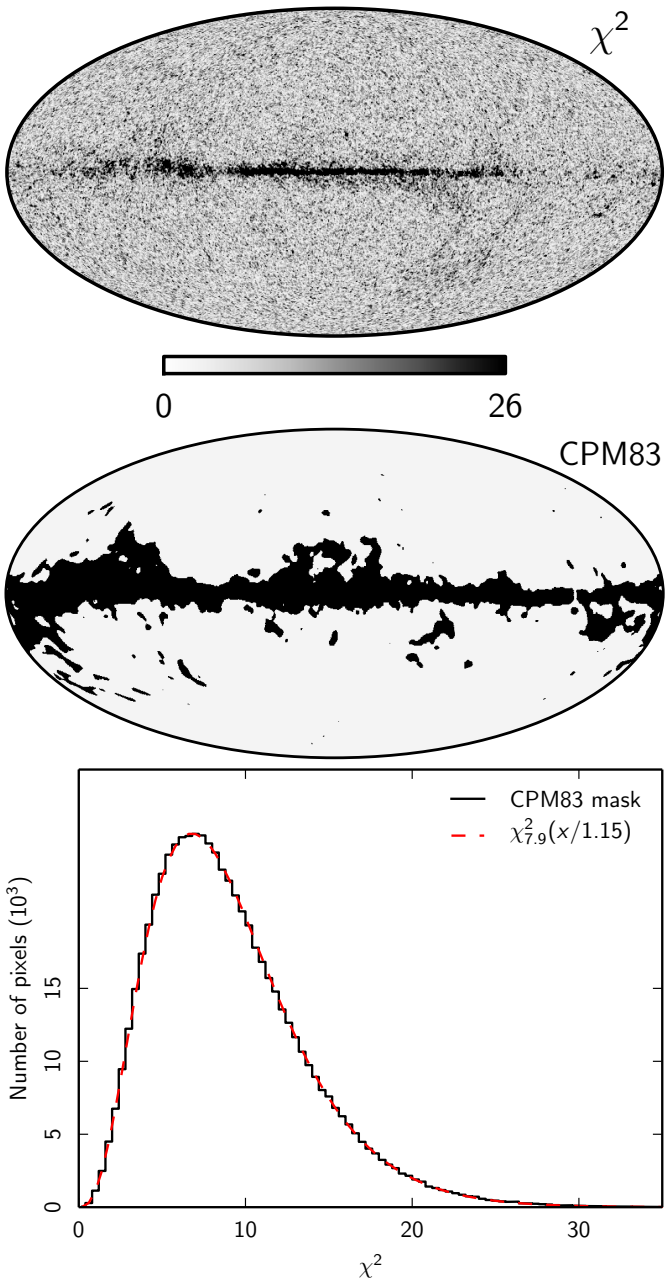

Fig. 41. *Top*: χ^2 per pixel for the polarization analysis of *Planck* observations between 30 and 353 GHz, summed over Stokes Q and U parameters. *Middle*: `Commander` polarization mask (CPM), defined as the product of the CO $J = 1 \rightarrow 0$ emission map thresholded at 0.5 K_{RJ} km s^{-1}, and the smoothed χ^2 map thresholded at a value of 26. This mask retains a total of 83% of the sky. *Bottom*: histogram of χ^2 values outside the conservative CPM83 mask. The grey dashed line shows the best-fit χ^2 distribution with a variable degree of freedom and scaling, used to account for noise modelling effects.

Table 10. Goodness-of-fit statistics for polarization analysis.

Frequency [GHz]	Rms outside CPM83	
	$\sigma_\nu^{\rm res}$ [μK]	$\sigma_\nu^{\rm res}/\sigma_\nu^{\rm inst}$
30	2.12	0.28
44	7.59	1.01
70	4.85	1.01
100	1.18	0.90
143	0.90	0.81
217	1.52	0.95
353	2.93	0.42

Next, we assess the impact of temperature-to-polarization leakage from the CMB temperature monopole and dipole and from Galactic temperature emission by computing the synchrotron and thermal dust amplitude maps when adopting two different HFI leakage models. The first is simply the default template set adopted for the *Planck* 2015 release, corresponding to the results already discussed, while the second is the experimental template set described in Planck Collaboration VIII (2016) and Planck Collaboration XI (2016). From the resulting amplitude maps, we perform the following steps: first compute the polarization amplitude, P; smooth this to 3° FWHM for synchrotron and 1° FWHM for thermal dust; and finally compute the difference, $P_2 - P_1$, and fractional difference, $(P_2 - P_1)/P_1$, maps. These are shown in Fig. 42. Here we see that the absolute polarization amplitude difference between the two leakage models is around 1 μK_{RJ} for both synchrotron and thermal dust at high Galactic latitudes, increasing to a few tens of μK_{RJ} in the Galactic plane. Accordingly, the fractional residuals are $\lesssim$10% at high Galactic latitudes, and they increase to about 30% in the central Galactic plane.

Finally, we comment on the polarization fractions that may be derived from these maps. First of all, we emphasize that the delivered products are maps of the Stokes Q and U parameters, not of polarization amplitude and polarization angle and fractions. This choice is primarily driven by the fact that the Stokes parameters are linear, and therefore have much simpler noise properties than the corresponding nonlinear parameters. Second, when computing polarization fractions, P/I, it is of utmost importance to recognize and account for the considerable uncertainty in this quantity with respect to the zero-level of the corresponding temperature map. To make this point concrete, we show in the top panel of Fig. 43 the naive polarization fraction derived directly from the delivered `Commander` thermal dust intensity and polarization maps. This map saturates the colour scale over extended regions in the southern Galactic hemisphere, nominally suggesting a polarization fraction well above 20%. However, as discussed both in Sect. 3 and Planck Collaboration VIII (2016), there is an offset in the zero-level of the zodiacal light emission of 34 μK in the current 353 GHz temperature data. Correcting for this offset results in the polarization fraction shown in the lower panel of Fig. 43, which shows significantly smaller values. Further, the raw statistical uncertainty of the 353 GHz Galactic emission zero level from H I cross-correlation alone is 23 μK (Planck Collaboration VIII 2016). The conclusion is therefore that any analysis that relies directly on the polarization fraction, as opposed to the much more stable polarization amplitude, needs to account for the significant uncertainties in the Galactic emission zero-level at 353 GHz.

6.2. Synchrotron and thermal dust angular power spectra

One of the most important goals of modern CMB cosmology is to detect primordial B-mode polarization on large angular scales, a direct observable signature of inflationary gravitational waves. The main obstacles in this search are the polarized synchrotron and thermal emission signals discussed above. In order to quantify the magnitude of this problem, we compute in this section their angular power spectra, and compare them to the expected

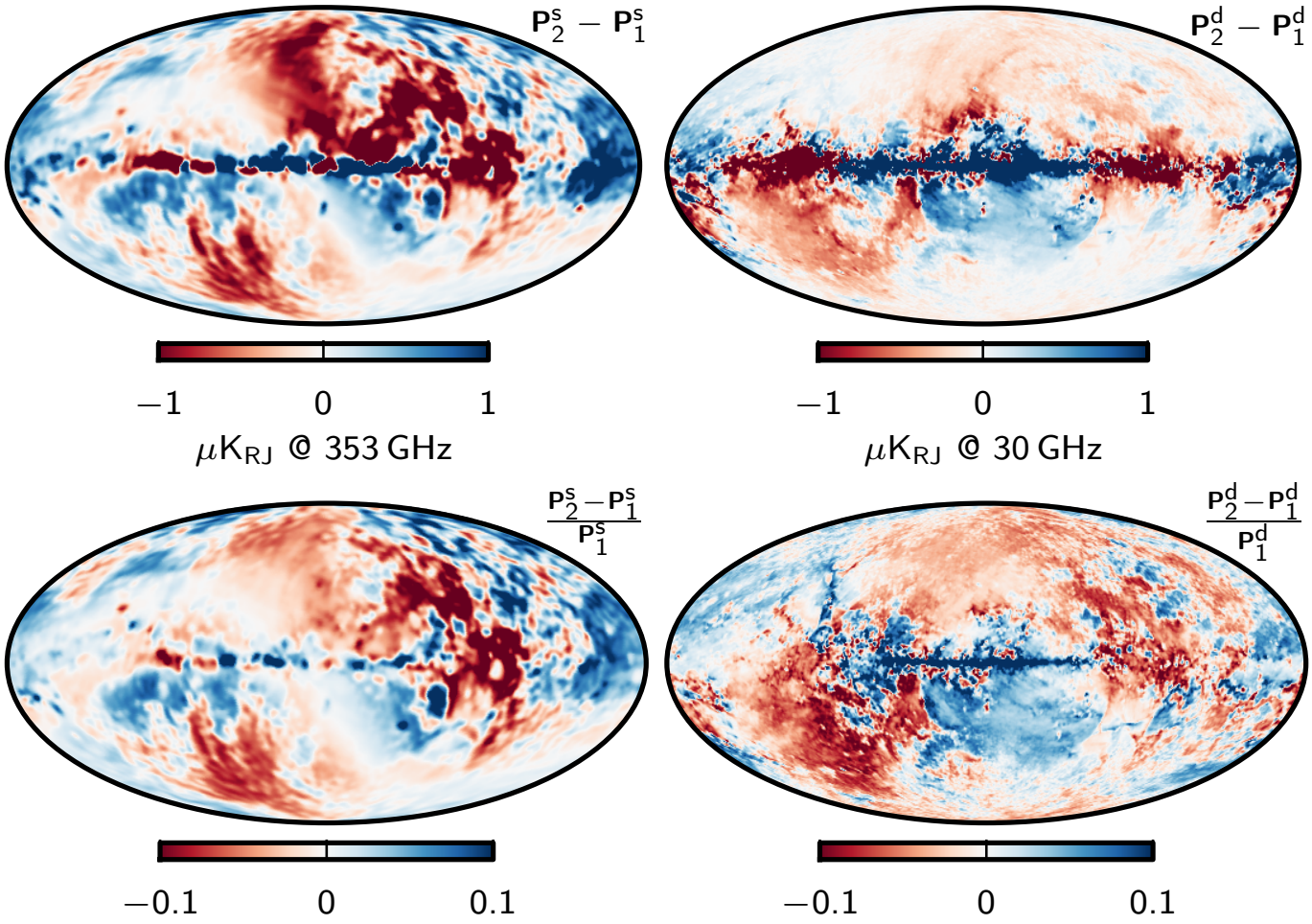

Fig. 42. Difference maps (*top*) and fractional difference maps (*bottom*) between the synchrotron (*left*) and thermal dust (*right*) polarization solutions derived with two different HFI temperature-to-polarization leakage templates. The synchrotron polarization amplitude maps are smoothed to 3° FHWM before computing absolute and fractional differences, and the thermal dust polarization amplitude maps are smoothed to 1°. Maps labelled by a subscript "1" correspond to the default leakage templates used in the *Planck* 2015 release, and maps labelled by a subscript "2" correspond to the experimental leakage templates; see Planck Collaboration VIII (2016) for further discussion.

primordial CMB spectrum. A more comprehensive analysis of the same type, but based only on the 353 GHz frequency channel, was recently published in Planck Collaboration Int. XXX (2016).

We employ the same cross-spectrum power spectrum estimator as used in Planck Collaboration Int. XXX (2016), but introduce two specific changes. First, we adopt the so-called common mask from the CMB component separation analysis presented in Planck Collaboration IX (2016), rather than the CO mask employed in the original paper, and second, we consider three different mask apodization scales (1, 2, and 5° FWHM) as opposed to only 5° FWHM as in Planck Collaboration Int. XXX (2016).

The *EE* and *BB* spectra resulting from the evaluation using 1° FWHM apodization are shown in the left and right panels of Fig. 44, respectively, both plotted in terms of $D_\ell = C_\ell\,\ell(\ell+1)/2\pi$ in thermodynamic units. Red data points show the angular power spectra for thermal dust emission at 353 GHz, and green points show synchrotron emission at 30 GHz. Each spectrum is binned with $\Delta\ell = 25$, and the plotted uncertainties are the standard deviation of the single-ℓ spectrum values within each bin. Black solid lines indicate the best-fit ΛCDM spectrum (Planck Collaboration XI 2016), and (in the *BB* panel only) the dashed black line shows the spectrum for a tensor-to-scalar ratio of $r = 0.05$. Dotted coloured lines indicate the best-fit power-law fit, $D_\ell = q\,(\ell/80)^\alpha$, to each foreground spectrum, where the pivot scale of $\ell_0 = 80$ is chosen to match that used in Planck Collaboration Int. XXX (2016). The corresponding best-fit parameters are tabulated in Table 11 for all three apodization scales, and including multipoles in the range $\ell = (10, 150)$ for synchrotron and $\ell = (10, 300)$ for thermal dust emission. No synchrotron results are shown for the 5° FWHM apodization scale. In this case, the effective sky fraction is too small to allow a robust estimate of the synchrotron spectrum.

For thermal dust emission these parameters may be compared to the results presented in Planck Collaboration Int. XXX (2016), although a few caveats are in order. In particular: (1) the masks used in the two analyses are different, and the mask adopted in this paper effectively removes more sky around bright point sources after apodization; (2) the map considered in the present analysis is the `Commander` thermal dust map, whereas the original analysis considered the raw 353 GHz map; (3) the multipole ranges adopted for the parameter fits are slightly different; and (4) we make the fit to the single-ℓ power spectrum, not the binned spectrum.

Nevertheless, we see that the results derived here are in good agreement with those found in Planck Collaboration Int. XXX (2016). In particular, when considering the same apodization scale of 5° FWHM, we recover an identical *BB*/*EE* ratio of

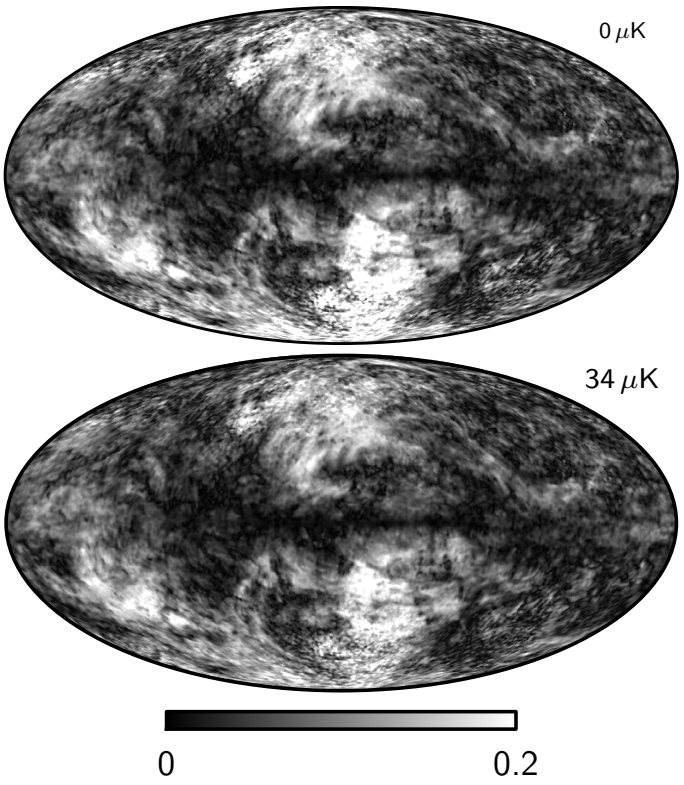

Fig. 43. Thermal dust polarization fraction for Galactic emission zero-level corrections of 0 μK (*top*) and 34 μK (*bottom*). A value of 34 μK corresponds to our current best estimate of the residual zodiacal light offset in the 353 GHz channel (Planck Collaboration VIII 2016). The statistical uncertainty on the Galactic emission zero-level from H I cross-correlation is 0.0067 MJy sr^{-1} or 23 μK_{CMB}.

Table 11. Best-fit power-law parameters to the angular power spectra of synchtrotron (at 30 GHz) and thermal dust emission (at 353 GHz) as a function of mask apodization.

	Synchrotron		Thermal dust	
	q [μK^2_{CMB}]	α	q [μK^2_{CMB}]	α
Common mask; apod = 1° FWHM; f_{sky}^{eff} = 0.73				
EE	3.7 ± 0.2	−0.44 ± 0.07	354 ± 6	−0.53 ± 0.02
BB	1.3 ± 0.2	−0.31 ± 0.13	208 ± 4	−0.59 ± 0.02
BB/EE . . .	0.36 ± 0.06		0.59 ± 0.01	
Common mask; apod = 2° FWHM; f_{sky}^{eff} = 0.68				
EE	3.2 ± 0.2	−0.49 ± 0.08	285 ± 5	−0.53 ± 0.02
BB	1.1 ± 0.2	−0.02 ± 0.17	161 ± 3	−0.62 ± 0.02
BB/EE . . .	0.34 ± 0.07		0.56 ± 0.01	
Common mask; apod = 5° FWHM; f_{sky}^{eff} = 0.55				
EE			188 ± 3	−0.44 ± 0.02
BB			99 ± 2	−0.51 ± 0.03
BB/EE . . .			0.53 ± 0.01	
CO mask; apod = 5° FWHM; f_{sky}^{eff} = 0.73; Planck Int. XXX (2014)				
EE			328 ± 3	−0.43 ± 0.02
BB			· · ·	−0.46 ± 0.02
BB/EE . . .			0.53 ± 0.01	

Notes. The parameters are defined by the model $D_\ell = q\,(\ell/80)^\alpha$, and the fits include multipoles between ℓ = 10 and 150 for synchrotron, and between ℓ = 10 and 300 for thermal dust emission. All uncertainties are statistical, and do not account for systematic or modelling uncertainties. The last case is reproduced from Table 1 in Planck Collaboration Int. XXX (2016).

0.53 ± 0.01, and the EE power-law index agree to 0.5σ. For BB, the spectral index difference is slightly larger, but still within 2σ. The power spectrum amplitudes, on the other hand, are different because of the different effective sky fractions of the two corresponding apodized masks.

Comparing the different apodization scales, we note both that the BB/EE ratio increases slightly, and that the power-law indices steepens slightly, as the mask smoothing scale increases. This is due to thermal dust emission being a highly non-isotropic and non-Gaussian field, as discussed in Planck Collaboration Int. XXX (2016). It is not surprising that its statistical properties may vary between the Galactic plane and the high Galactic latitudes. In addition, there is an algorithmic uncertainty in the form of so-called E-to-B leakage, due to ambiguous polarization modes near the mask edge. This leakage is far stronger for foregrounds than for CMB, simply because the foreground field by construction is at its maximum near the mask boundary. As a result, it is important to specify the properties of the analysis mask when summarizing the power spectrum of a foreground field, as demonstrated in Table 11.

Overall, however, the mask dependence on the angular power spectrum is modest, and D_ℓ provides a useful summary for foreground fields as well as for the CMB field. Indeed, one of the interesting results reported by Planck Collaboration Int. XXX (2016) was the asymmetry between the B- and E-mode thermal dust power spectra, with a power ratio of $BB/EE \approx 0.5$. This has strong implications for the underlying astrophysics, and indicates the presence of significant filamentary structures on intermediate angular scales. In this paper, we find that the same holds also for synchrotron emission, with an even stronger asymmetry of $BB/EE \approx 0.35$. Thus, polarized synchrotron emission appears to be more strongly aligned along filamentary structures than thermal dust.

We also find similar power-law indices for synchrotron emission as for thermal dust, with $\alpha \approx -0.4$. However, the uncertainties are relatively larger, because of the lower signal-to-noise ratio of the 30 GHz channel compared to the 353 GHz channel.

These power-law fits can be used to model the total foreground level as a function of both multipole moment and frequency. This is illustrated in Fig. 45 for the 1° FWHM apodization case in terms of iso-contour plots of the following amplitude ratio,

$$f = \sqrt{\frac{D_\ell^{\rm s}(\nu) + D_\ell^{\rm d}(\nu)}{D_\ell^{\rm CMB}}} \tag{21}$$

$$= \sqrt{\frac{q_{\rm s}\left(\frac{\ell}{80}\right)^{\alpha_{\rm s}} \frac{s_{\rm s}(\nu)}{s_{\rm s}(30\,{\rm GHz})} + q_{\rm d}\left(\frac{\ell}{80}\right)^{\alpha_{\rm d}} \frac{s_{\rm d}(\nu)}{s_{\rm d}(353\,{\rm GHz})}}{D_\ell^{\rm CMB}}}, \tag{22}$$

where subscripts "s" and "d" refer to synchrotron and thermal dust. The frequency spectra, $s_{\rm s}(\nu)$ and $s_{\rm d}(\nu)$, are the synchrotron (GALPROP) and thermal dust (one-component greybody) spectra defined in Table 4 converted to thermodynamic units, with parameters defined by the average parameters listed in Table 5. This function is thus simply a model of the foreground-to-CMB amplitude ratio as a function of multipole and frequency.

Considering first the EE case shown in the left panel of Fig. 45, we note several interesting features. First, the horizontal ripples seen at $\ell \gtrsim 100$ correspond to the CMB acoustic oscillations. Next, we see that the foregrounds-to-CMB ratio is smaller than unity for all multipoles above $\ell \gtrsim 40$ for frequencies around 70 GHz, and smaller than 10% for $\ell \gtrsim 200$. Also, recall that the

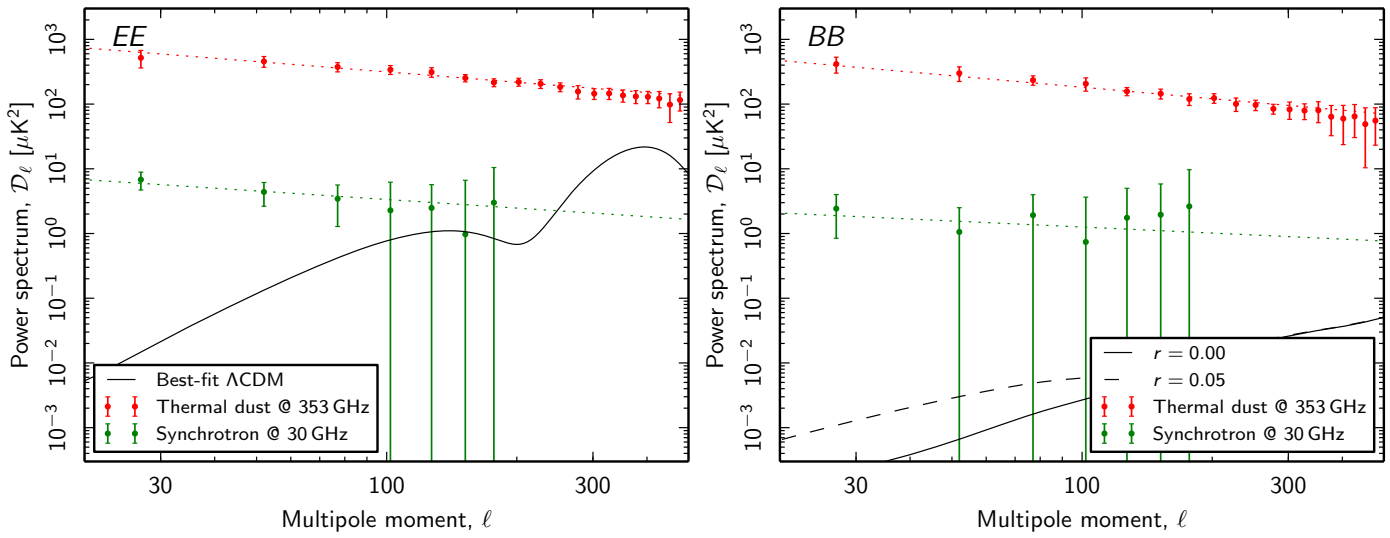

Fig. 44. Angular *EE* (*left panel*) and *BB* (*right panel*) power spectra for polarized synchrotron (at 30 GHz) and thermal dust emission (at 353 GHz), evaluated with 1° FWHM apodization and including a total effective sky fraction of 73% of the sky. The dashed lines show the best-fit power-law models to each case, and the solid black lines shows the best-fit ΛCDM power spectrum as fitted to temperature observations only (Planck Collaboration XI 2016; Planck Collaboration XIII 2016). The dashed black line in the *BB* panel shows the spectrum for a model with a tensor-to-scalar ratio of $r = 0.05$.

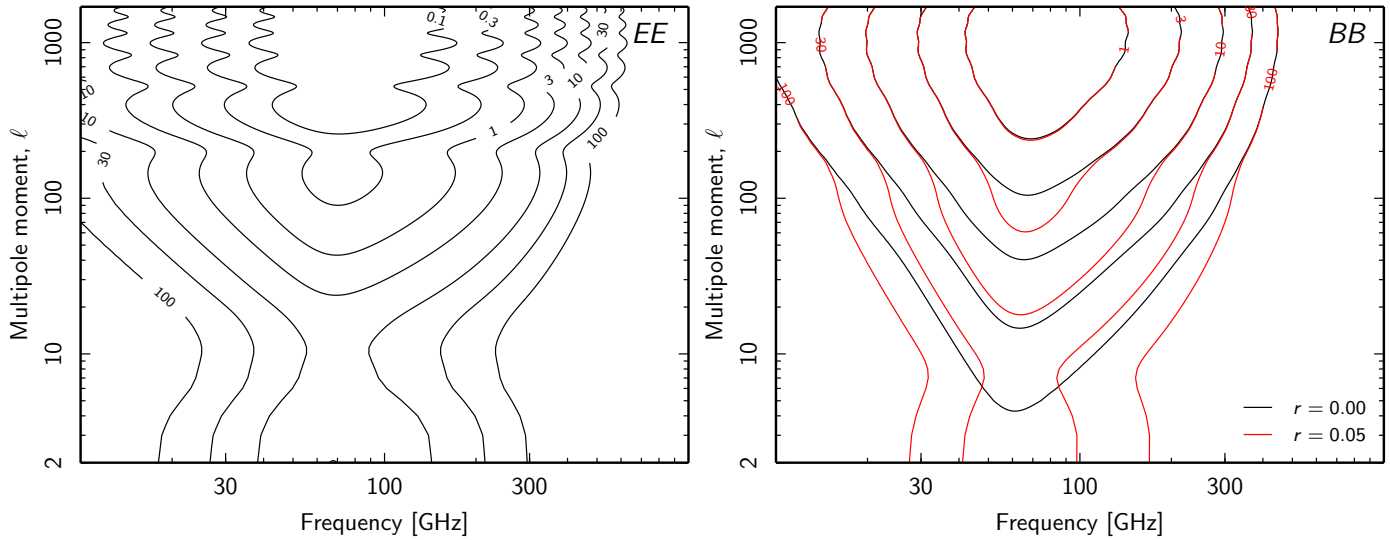

Fig. 45. Amplitude ratio between total polarized foregrounds and CMB as a function of both multipole moment and frequency, defined by $f(\ell, \nu) = [C_\ell^{\rm fg}(\nu)/C_\ell^{\rm CMB}]^{1/2}$, as defined Eq. (22) with parameters derived from 73% of the sky. The *left and right panels* show the *EE* and *BB* spectra, and the black and red contours in the latter corresponds to tensor-to-scalar ratios of $r = 0.0$ and 0.05, respectively.

corresponding power spectrum ratio goes as the square of these ratios, and we thus find that polarized foregrounds have a small effect on the *EE* spectrum at multipoles above a few hundred, in agreement with the results pesented in Planck Collaboration XI (2016). However, we also see that the same is by no means true at low multipoles; the foregrounds-to-CMB ratio is larger than 3 throughout the reionization peak for $\ell = 2$–10.

The right panel of Fig. 45 shows the corresponding ratio for *BB*, but in this case two different contour sets are plotted; one for the standard ΛCDM with a vanishing tensor-to-scalar ratio (black contours), and one with a tensor-to-scalar ratio of $r = 0.05$ (red contours). The peak around $\ell \approx 1000$ corresponds to the signature of weak gravitational lensing, converting E-modes into B-modes, whereas the "plateau" at low multipoles in the red contours corresponds to additional primordial fluctuations from inflationary gravitational waves. First of all, we see that foregrounds are sub-dominant to the lensing signal at multipoles above $\ell \gtrsim 200$ for frequencies around 70 GHz in this model, although they never fall below the 10% level. Second, for a vanishing tensor-to-scalar ratio the foreground-to-CMB around the recombination peak of $\ell \approx 100$ is about 3, and at the reionization peak, below $\ell \lesssim 10$, it is about 100. Increasing the tensor-to-scalar ratio to $r = 0.05$ decreases these numbers to about 2 and 20, respectively.

Before concluding this section, several caveats regarding the above observations are in order. First of all, it is important to remember that the angular power spectra reported here are computed over a large sky fraction including 72% of the sky. For a dedicated B-mode experiment, it obviously makes sense to consider more conservative masks. Second, it is also important to bear in mind that the angular spectra presented here covers only a limited multipole range, and the extrapolation to small angular scales is therefore associated with considerable uncertainty. Clearly, extrapolating actual observations that are made between

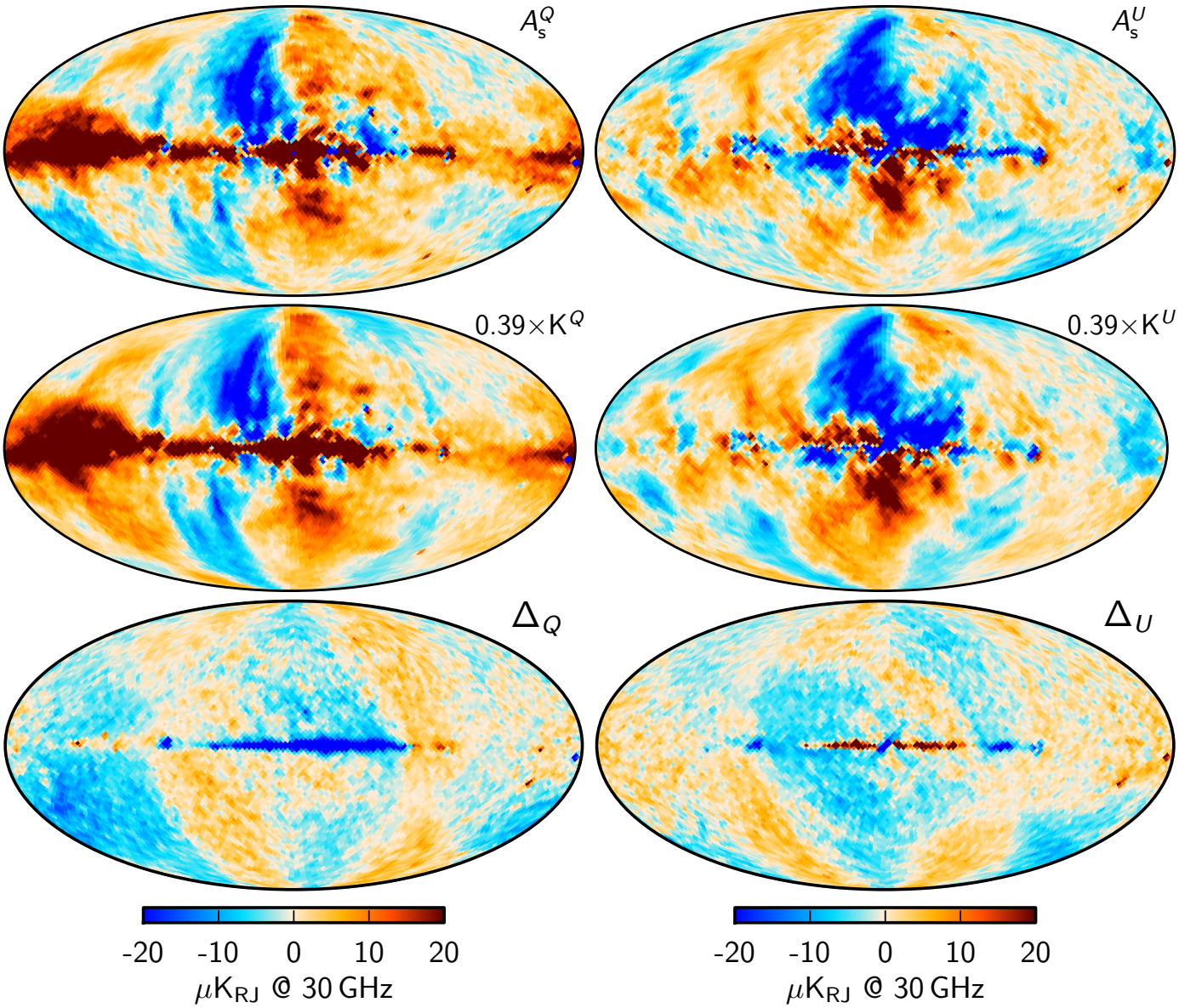

Fig. 46. Comparison of the *Planck* polarized synchrotron map (*top*) and the 9-yr WMAP *K*-band map, scaled to 30 GHz assuming a spectral index of $\beta_s = -3.2$ (*middle*); the bottom row shows the difference between the two maps. All maps are smoothed to a common resolution of 2° FWHM.

$\ell \approx 10$–100 to $\ell \approx 1000$ for synchrotron emission implies strong assumptions regarding the foreground composition of both diffuse foregrounds and compact objects.

6.3. Comparison with independent data products

We now turn to consistency tests based on external (or at least independently derived) data products. Of course, given the pioneering nature of the *Planck* polarization observations, the number of available external cross-checks is significantly sparser compared to the temperature case. On the low-frequency side, the WMAP *K*-band data represents an excellent comparison for the synchrotron map, while no products of comparable data quality exists on the high-frequency side at the moment. This lack of polarized dust measurements has of course been a major limitation for the entire CMB field for a long time, and the WMAP solution to this problem was to construct a polarized dust template by combining the FDS thermal dust intensity map (Finkbeiner et al. 1999) with polarization directions from starlight polarization observations (see Page et al. 2007 for full details).

We compare our new polarized thermal dust and synchrotron maps with the WMAP maps/templates in Figs. 46 and 47, and show corresponding T–T scatter plots in Figs. 48 and 49.

Starting with the synchrotron case, we see first of all in Fig. 48 that the overall pixel-to-pixel scatter between the *Planck* synchrotron map and the WMAP *K*-band map is substantial. Indeed, based on this full-sky scatter plot, any synchrotron spectral index between $\beta_s = -3.4$ and -3.0 appears consistent with the observations. Adopting a mean value of $\beta_s = -3.2$, and assuming an effective *K*-band frequency of 22.6 GHz, this translates into a total scaling factor of 0.39 between *K*-band and 30 GHz[16]. This scaling factor has been applied to the *K*-band map shown in Fig. 46, and it also allows us to form a

[16] The *Planck* 2015 foreground product maps are defined at sharp frequencies, and not as bandpass-averaged channel maps. The relevant comparison for synchrotron emission is therefore indeed 30 GHz, and not the effective frequency of the *Planck* 30 GHz band, which is 28.4 GHz.

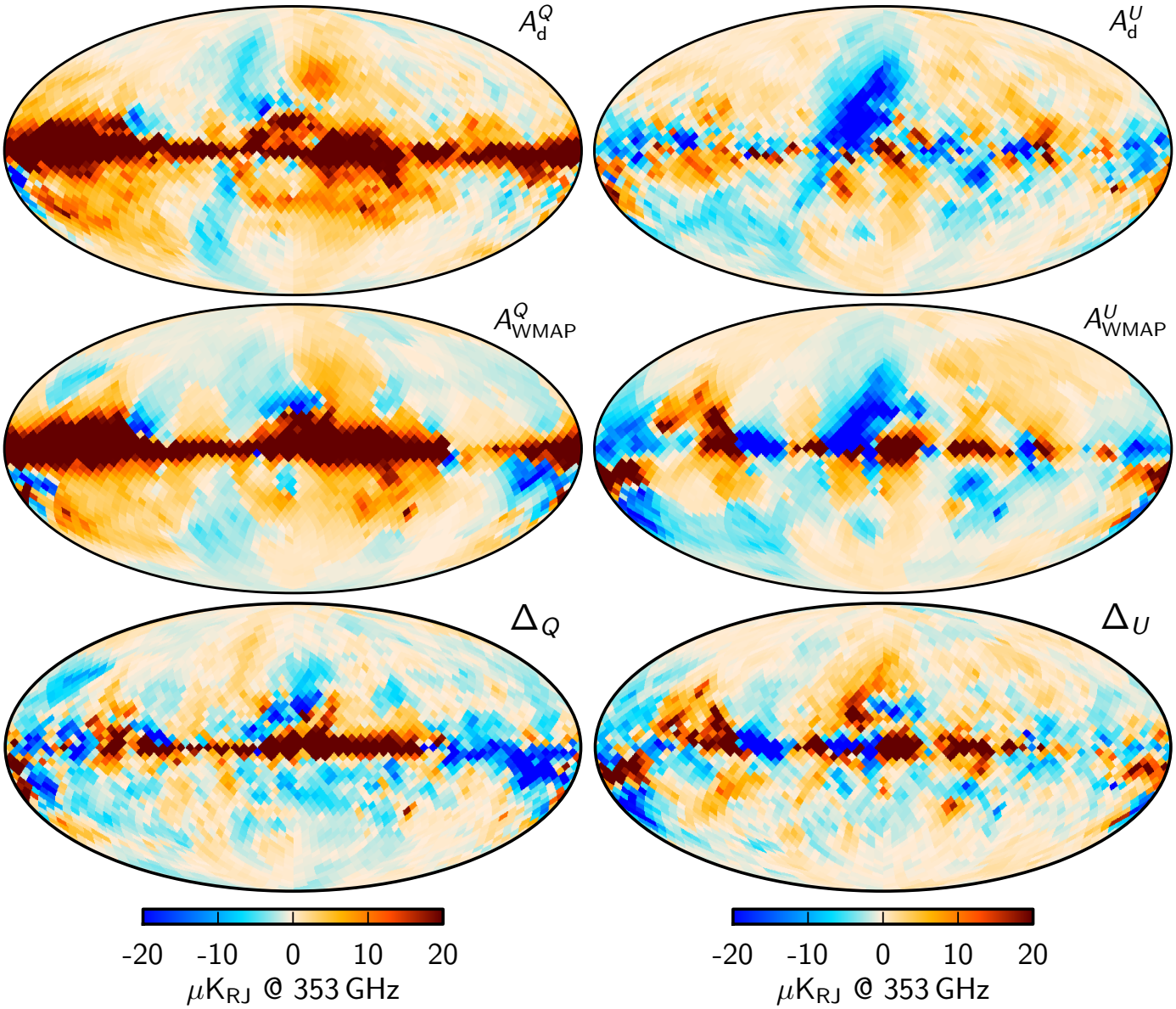

Fig. 47. Comparison of the *Planck* polarized thermal dust map at 353 GHz (*top*) and the WMAP polarized dust template, scaled to 353 GHz assuming a scaling factor of 480 μK (*middle*). The *bottom row* shows the difference between the two maps. All maps are pixelized at a `HEALPix` resolution of $N_{\rm side} = 16$.

meaningful residual map, as seen in the bottom row of the same figure.

The relative residuals between the *Planck* and WMAP synchrotron maps are clearly substantial, with amplitudes reaching 5 μK at high Galactic latitudes, and with a morphology clearly associated with the scanning strategy of either *Planck* or WMAP, both of which have symmetries defined by the Ecliptic reference frame. Furthermore, the residuals are very large-scale in nature, and obviously dominated by the two lowest multipoles, $\ell = 2$ and 3. It is therefore natural to consider what effects may cause such large-scale features. Starting with *Planck*, a large suite of null-tests and simulations, specifically targeting large-scale systematics in the LFI observations, is presented in Planck Collaboration II (2016). One noteworthy conclusion from that work is a significant null-test failure in the 44 GHz polarization frequency map for $\ell = 2$–4, and for two 70 GHz surveys. In addition, the HFI channels between 100 and 217 GHz are also affected by low level residual systematics (Planck Collaboration VIII 2016). As a result, these observations are currently excluded from the *Planck* 2015 low-ℓ likelihood, which instead only relies on the 30, 70 and 353 GHz channels (Planck Collaboration XI 2016). These large-scale 44 GHz modes are likely to contribute significantly to the residuals seen in Fig. 46. For WMAP, on the other hand, the statistical uncertainties in the WMAP EE $\ell = 2$ and BB $\ell = 3$ modes are very large (Bennett et al. 2013), due to the combination of the differential detectors of WMAP, and an opening angle of 141° between the A and B side reflectors. Although these uncertainties are appropriately described by the low-resolution WMAP covariance matrices, it is algorithmically non-trivial to account for this effect properly in component separation at higher resolution, and they are also likely to contribute to the residuals in Fig. 46.

These differences are also discussed in Planck Collaboration XXV (2016), with consistent conclusions. However, that analysis proceeds with co-adding the *Planck* and WMAP data sets

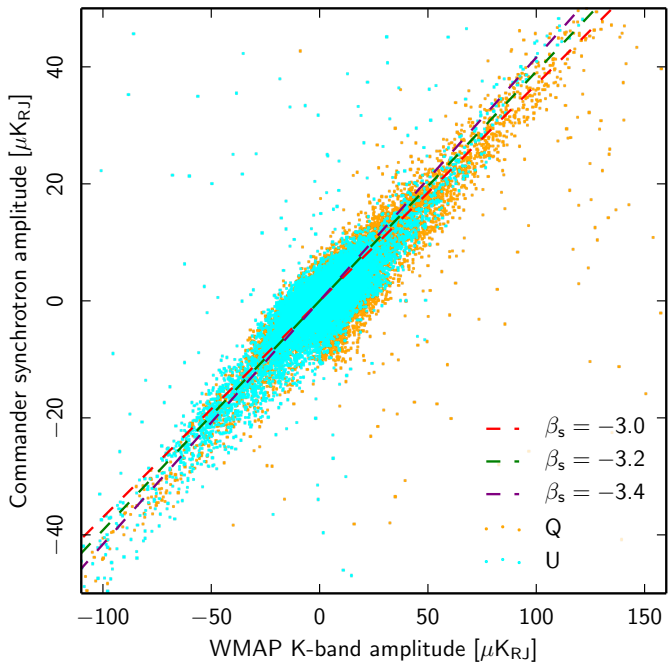

Fig. 48. T–T correlation plot between the *Planck* polarized synchrotron map at 30 GHz and the WMAP K-band map at 23 GHz for both Stokes Q and U parameters. The dashed coloured lines indicate synchrotron spectral indices of $\beta_s = -3.0$ (red), -3.2 (green) and -3.4 (violet), respectively.

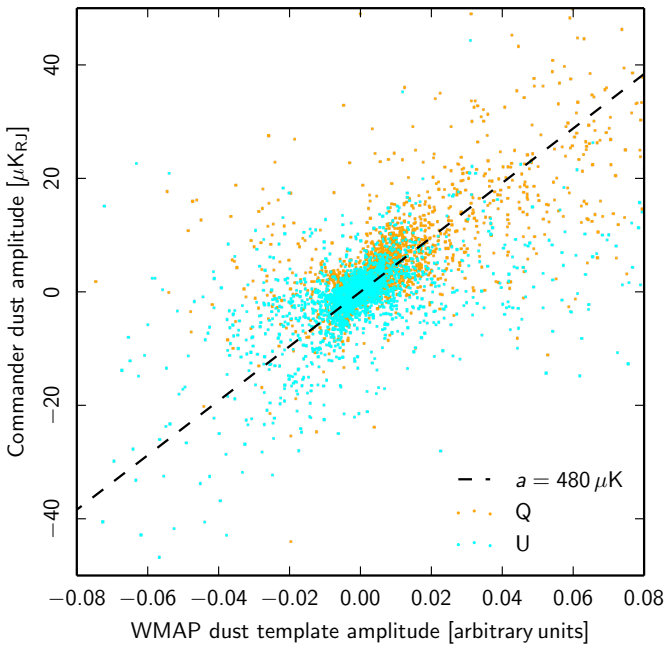

Fig. 49. T–T correlation plot between the *Planck* polarized thermal dust map (at 353 GHz) and the WMAP polarized dust template map (in arbitrary units) for both Stokes Q and U parameters. The dashed black line corresponds to a relative scaling factor of $480\,\mu$K$_{RJ}$.

to produce an alternative synchrotron map with higher signal-to-noise ratio, and use that map to identify new polarized synchrotron features and loops. A similar approach is not straightforward within the framework adopted in the current paper, which relies sensitively on parametric fits in the frequency domain. Within such a methodology, even just a single large-scale mode can severely bias the resulting spectral index map, rendering the full reconstruction meaningless; for a fully analogous problem, see the offset discussion in Sect. 4.1 for the temperature case. The proper way to solve this problem is either to account for the full covariance matrix in the analysis (as for instance was done by Dunkley et al. 2009), but this is only possible at very low angular resolution. An alternative approach is to marginalize over just a few modes using the template formalism described in Sect. 2. This requires accurate spatial templates in the first place, which possibly may be extracted as high-noise eigenmodes from the full noise covariance matrices. Exploratory work in this direction is already on-going, but the results have unfortunately not yet converged.

For now, we recognize that there are significant uncertainties in the synchrotron model provided, with respect to the very lowest multipoles. Fortunately, higher-ordered modes are in much better agreement between *Planck* and WMAP. This is important for several reasons, not least of which is estimation of the optical depth of reionization, τ, which depends sensitively on the low-ℓ modes. However, as shown in Planck Collaboration XI (2016), most of the statistical power for τ comes from $\ell = 4$–6, not $\ell = 2$ and 3. Thus, after removing the 44 GHz channel from the likelihood data set, all remaining null-tests pass.

A similar comparison between the *Planck* thermal dust map and the WMAP dust template is presented in Figs. 47 and 49. Of course, this is not a validation test of the *Planck* products in any way, since the two maps are by no means equivalent data products. Rather, this comparison provides an interesting reality check on the WMAP model.

The WMAP polarized dust template is provided in arbitrary units, and must therefore be re-scaled to match the amplitude of the *Planck* thermal dust map. The appropriate scale factor is given as the slope of the T–T correlation plot in Fig. 49. Averaging over the two Stokes parameters, we estimate this to be $480\,\mu$K$_{RJ}$ per WMAP unit. This allows us to form the difference map in the bottom row of Fig. 47. With the benefit of hindsight, we see that the WMAP model is accurate to within 20–30% over most of the high-amplitude sky, although some regions show deviations at the 50% level. Larger scales are reproduced with greater fidelity than smaller scales.

Given the lack of proper external validation data sets for the polarized thermal dust emission maps, we instead compare our products with an independent internal *Planck* product, similar to what was done for the CO intensity maps in Sect. 5.5.3. Specifically, we compare the `Commander` dust map with an equivalent map derived with the `SMICA` algorithm (Planck Collaboration XII 2014; Planck Collaboration IX 2016). The results from this comparison are summarized in Fig. 50, in terms of: the polarization amplitude difference between the two maps (top panel); the fractional polarization amplitude difference map (middle panel); and a T–T correlation plot of the individual Stokes Q and U parameters[17]. First, we see that the two codes agree to better than 2% in the Galactic plane, which is very good, considering the quite different effective bandpass treatments in the two approaches. In particular, no explicit bandpass integration corrections are applied in the `SMICA` analysis, but all calculations are performed at the bandpass integrated frequency channel level.

[17] The only reason for not showing the `SMICA` map itself is that it appears nearly identical to the `Commander` map shown in Fig. 38, and the map therefore does not provide much new information.

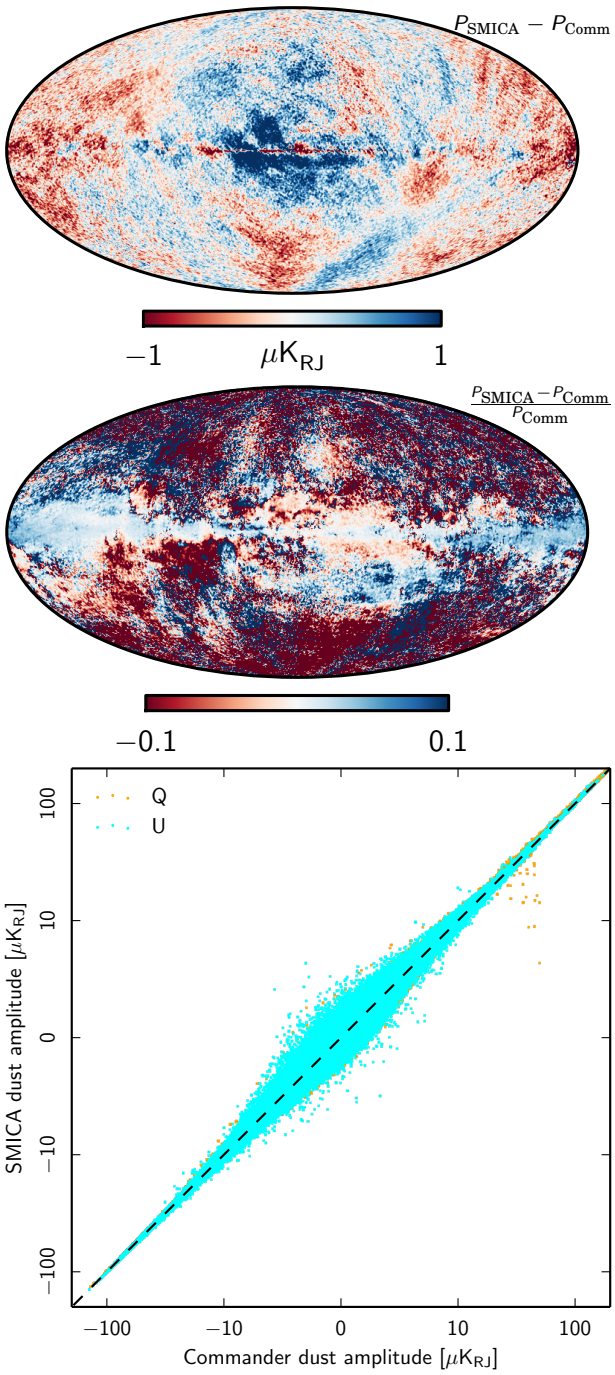

Fig. 50. Comparison between the polarized dust amplitude maps, $P = \sqrt{Q^2 + U^2}$, derived by `SMICA` and `Commander` at 353 GHz. The three panels show the difference map, $\boldsymbol{d}_{\rm SMICA} - \boldsymbol{d}_{\rm Comm}$ (*top*), the fractional difference map, $(\boldsymbol{d}_{\rm SMICA} - \boldsymbol{d}_{\rm Comm})/\boldsymbol{d}_{\rm Comm}$ (*middle*), and a T–T correlation plot. Units are μK$_{\rm RJ}$.

However, the agreement is not equally good at high Galactic latitudes, with residuals at the roughly 1 μK$_{\rm RJ}$ level. Furthermore, these residuals have a morphology that resembles known instrumental systematics, in particular in the form of monopole and dipole leakage and ADC corrections (Planck Collaboration IX 2016). Thus, the two algorithms clearly respond differently to known systematics, and we accordingly estimate that the systematic uncertainty in the large-scale modes of the *Planck* polarized dust map due to instrumental effects to be (at least) 1 μK$_{\rm RJ}$ at 353 GHz. Fortunately, these instrumental effects are expected to be significantly reduced in the final *Planck* data release.

7. Summary and conclusions

We have presented the baseline *Planck* 2015 astrophysical foreground products in both temperature and polarization, as derived within a Bayesian parameter estimation framework. Combining the new *Planck* sky maps with complementary ancillary data in the form of the 9-yr WMAP temperature sky maps and the low-frequency 408 MHz Haslam et al. survey, we are able to reconstruct a total of six primary emission temperature mechanisms – CMB, synchrotron, free-free, spinning dust, CO, and thermal dust emission – in addition to two secondary components, namely thermal SZ emission around the Coma and Virgo clusters, and line emission between 90 and 100 GHz. For polarization, we reconstruct three primary emission mechanisms – CMB, synchrotron, and thermal dust. In addition to these astrophysical parameters, we account jointly for calibration and bandpass measurement errors, as well as monopole and dipole uncertainties. Statistical uncertainties are propagated from raw sky maps to final results by means of standard MCMC sampling techniques, while various model errors are assessed by end-to-end simulations. All data products are made publicly available, as summarized in Table 5.

Three particularly noteworthy highlights from this analysis is the following.

- We have presented the first full-sky polarized thermal dust map, which is a direct result of the exquisite sensitivity of the HFI instrument. This map will remain a cornerstone of future CMB cosmology for the next decade or more, as the search for primordial gravitational waves enters the next phase in which foregrounds are more important than instrumental noise.
- We have also presented a full-sky spinning dust intensity map. In addition to its obvious scientific value, this map is also interesting for algorithmic reasons, as a clear demonstration of both the importance and power of joint global analysis. Neither WMAP nor *Planck* have the statistical power to disentangle spinning dust from synchrotron, but together beautiful new results emerge. We believe that this will be the default approach for virtually all future microwave surveys, as no experiment will have the power to replace *Planck* and WMAP by themselves. Rather, each new experiment will contribute with a new critical piece of information regarding a given phenomenon, frequency coverage, or range of angular scales, and thereby help refining the overall picture. Global Bayesian analysis provides a very natural framework for this work.
- Another useful illustration of the power of global analysis presented in this paper is the identification of important instrumental systematic errors. One example is the detection of, and correction for, systematic errors in the *Planck* bandpass measurements. More generally, the residual maps shown in Figs. 2, 21, and 40 comprise a treasure trove of information on instrumental systematics that should prove very valuable for improving the raw *Planck* sky maps before the next data release.

All things considered, the sky model presented in this paper provides an impressive fit to the current data, with temperature residuals at the few microkelvin level at high latitudes across the CMB-dominated frequencies, and with median fractional

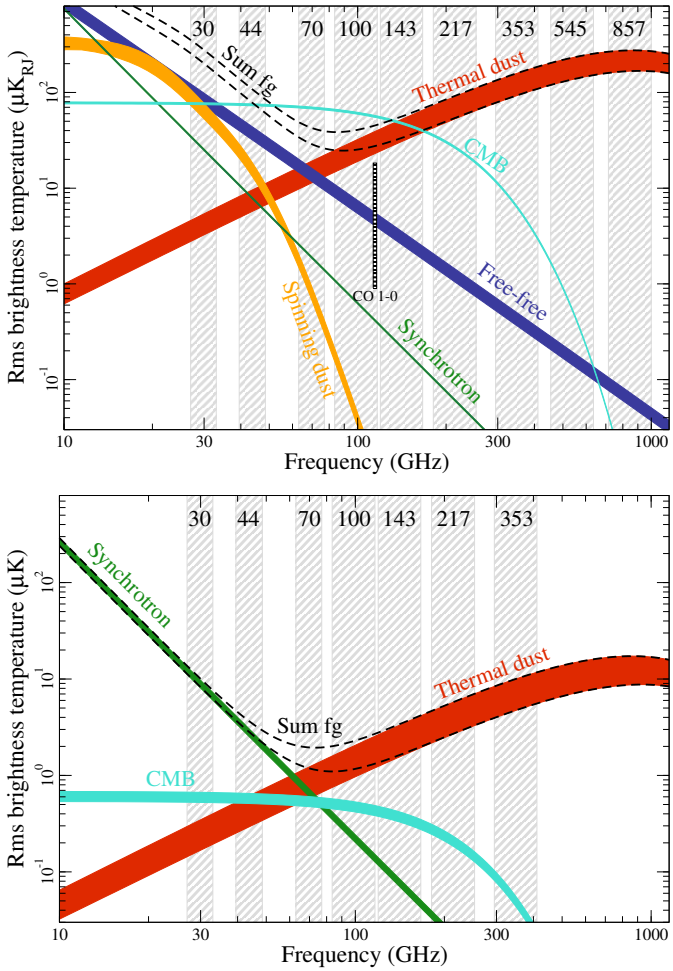

Fig. 51. Brightness temperature rms as a function of frequency and astrophysical component for temperature (*top*) and polarization (*bottom*). For temperature, each component is smoothed to an angular resolution of 1° FWHM, and the lower and upper edges of each line are defined by masks covering 81 and 93% of the sky, respectively. For polarization, the corresponding smoothing scale is 40′, and the sky fractions are 73 and 93%. We note that foreground rms values decrease nearly monotonically with sky fraction, whereas the CMB rms is independent of sky fraction, up to random variations. For reference, zodical light emission is roughly two orders of magnitude weaker than thermal dust emission in temperature.

errors below 1% in the Galactic plane across the *Planck* frequencies. For polarization, the residuals are statistically consistent with instrumental noise at high latitudes, but limited by significant temperature-to-polarization leakage in the Galactic plane. Overall, this model represents the most accurate and complete description currently available of the astrophysical sky between 20 and 857 GHz.

Figure 51 provides an overview of the main components in both temperature (top panel) and polarization (bottom panel), summarized in terms of the brightness temperature rms evaluated over 93% and 73% of the sky, respectively. For polarization, this is the first version of such a plot that is based on observations alone. For temperature, the most recent previous version is figure 22 of Bennett et al. (2013), summarizing the WMAP temperature foreground model. While the two versions agree well in terms of total foreground power and location of the foreground minimum, there are a few subtle differences as well. The most important of these is the relative amplitude of synchrotron and spinning dust. Specifically, synchrotron dominates over spinning dust at all frequencies in the WMAP model, whereas in our new model spinning dust dominates over synchrotron between 15 and 60 GHz. Such differences are not surprising, considering the complexity of the astrophysical foregrounds at low frequencies. As emphasized repeatedly, even when combining the *Planck* and WMAP observations, as done in this paper, degeneracies between synchrotron, free-free and spinning dust remain the leading source of uncertainty on the low frequency side. Additional observations between, say, 2 and 20 GHz are essential to break these degeneracies. For a more complete analysis of the low-frequency foreground model presented here, we refer the interested reader to Planck Collaboration XXV (2016).

On the high-frequency side, the main outstanding issue are uncertainties in the net 545 and 857 GHz calibration, i.e., the product of calibration and bandpass uncertainties. As of today, the 545 GHz calibration is uncertain at least at the 1–2% level, and this translates into an effective 3–6% uncertainty for the 857 GHz channel in our fits (in order to maintain a physical thermal dust frequency scaling). Cross-correlations with H I observations suggests a total systematic error on the thermal dust temperature at high Galactic latitudes of 1–2 K. Recognizing both calibration and modelling errors, we emphasize that the thermal dust model presented here does not represent an accurate model of frequencies beyond 857 GHz. For instance, naive extrapolation to the DIRBE 100 μm channel results in residuals as large as 40%. Both more physical models and better calibration are needed to extend into this regime. In addition, it is important to note that the current model makes no attempt at separating Galactic thermal dust emission from CIB fluctuations, and these therefore constitute a significant contaminant in our thermal dust model on small angular scales.

Finally, for polarization the main limitations are instrumental systematics, primarily in the form of temperature-to-polarization leakage, uncertainties in the analogue-to-digital conversion, and very long time constants (Planck Collaboration I 2016; Planck Collaboration VI 2016; Planck Collaboration VIII 2016). Thus, although the new *Planck* 2015 observations already have opened up a completely new window on the physics of our own Galaxy, through its deep observations of polarized thermal dust, more work is required in order to fully realize the science potential of the *Planck* measurements. This will be the main focus of the *Planck* analysis efforts in the coming months.

Acknowledgements. The Planck Collaboration acknowledges the support of: ESA; CNES, and CNRS/INSU-IN2P3-INP (France); ASI, CNR, and INAF (Italy); NASA and DoE (USA); STFC and UKSA (UK); CSIC, MINECO, JA and RES (Spain); Tekes, AoF, and CSC (Finland); DLR and MPG (Germany); CSA (Canada); DTU Space (Denmark); SER/SSO (Switzerland); RCN (Norway); SFI (Ireland); FCT/MCTES (Portugal); ERC and PRACE (EU). A description of the Planck Collaboration and a list of its members, indicating which technical or scientific activities they have been involved in, can be found at http://www.cosmos.esa.int/web/planck/planck-collaboration

References

Ali-Haïmoud, Y. 2010, SpDust/SpDust.2: Code to Calculate Spinning Dust Spectra, Astrophysics Source Code Library
Ali-Haïmoud, Y., Hirata, C. M., & Dickinson, C. 2009, MNRAS, 395, 1055
Alves, M. I. R., Calabretta, M., Davies, R. D., et al. 2015, MNRAS, 450, 2025
Battistelli, E. S., De Petris, M., Lamagna, L., et al. 2003, ApJ, 598, L75
Bennett, C. L., Larson, D., Weiland, J. L., et al. 2013, ApJS, 208, 20
Bull, P., Wehus, I. K., Eriksen, H. K., et al. 2015, ApJS, 219, 10
Carretti, E., Gaensler, B., Staveley-Smith, L., et al. 2009, *S*-band Polarization All Sky Survey (*S*-PASS), ATNF Proposal
Dame, T. M., Hartmann, D., & Thaddeus, P. 2001, ApJ, 547, 792
Davies, R. D., Dickinson, C., Banday, A. J., et al. 2006, 370, 1125
de Oliveira-Costa, A., Kogut, A., Devlin, M. J., et al. 1997, ApJ, 482, L17

Dickinson, C., Davies, R. D., & Davis, R. J. 2003, MNRAS, 341, 369
Diego, J. M., & Ascasibar, Y. 2008, MNRAS, 389, 1805
Draine, B. T. 2011, Physics of the Interstellar and Intergalactic Medium (Princeton University Press)
Draine, B. T., & Hensley, B. 2013, ApJ, 765, 159
Draine, B. T., & Lazarian, A. 1998, ApJ, 494, L19
Draine, B. T., & Lazarian, A. 1999, ApJ, 512, 740
Dunkley, J., Komatsu, E., Nolta, M. R., et al. 2009, ApJS, 180, 306
Erickson, W. C. 1957, ApJ, 126, 480
Eriksen, H. K., O'Dwyer, I. J., Jewell, J. B., et al. 2004, ApJS, 155, 227
Eriksen, H. K., Dickinson, C., Lawrence, C. R., et al. 2006, ApJ, 641, 665
Eriksen, H. K., Jewell, J. B., Dickinson, C., et al. 2008, ApJ, 676, 10
Finkbeiner, D. P., Davis, M., & Schlegel, D. J. 1999, ApJ, 524, 867
Fixsen, D. J. 2009, ApJ, 707, 916
Gelman, A., Carlin, J. B., Stern, H. S., & Rubin, D. B. 2003, Bayesian Data Analysis (Chapman and Hall/CRC)
Gispert, R., Lagache, G., & Puget, J. L. 2000, A&A, 360, 1
Gold, B., Odegard, N., Weiland, J. L., et al. 2011, ApJS, 192, 15
Górski, K. M., Hivon, E., Banday, A. J., et al. 2005, ApJ, 622, 759
Greaves, J. S., Holland, W. S., Friberg, P., & Dent, W. R. F. 1999, ApJ, 512, L139
Handa, T., Yoda, T., Kohno, K., et al. 2012, in Galactic Archaeology: Near-Field Cosmology and the Formation of the Milky Way, eds. W. Aoki, M. Ishigaki, T. Suda, T. Tsujimoto, & N. Arimoto, ASP Conf. Ser., 458, 221
Hartmann, D., Magnani, L., & Thaddeus, P. 1998, ApJ, 492, 205
Haslam, C., Stoffel, H., Salter, C. J., & Wilson, W. E. 1982, A&AS, 47, 1
Hauser, M. G., Arendt, R. G., Kelsall, T., et al. 1998, ApJ, 508, 25
Hu, W., & White, M. 1997, New Astron., 2, 323
Hurier, G., Macías-Pérez, J. F., & Hildebrandt, S. 2013, A&A, 558, A118
Jeffreys, H. 1946, Proc. Royal Society of London. Series A, Math. Phys. Sci., 186, 453
Jewell, J., Levin, S., & Anderson, C. H. 2004, ApJ, 609, 1
Kalberla, P. M. W., McClure-Griffiths, N. M., Pisano, D. J., et al. 2010, A&A, 521, A17
Kamionkowski, M., Kosowsky, A., & Stebbins, A. 1997, Phys. Rev. D, 55, 7368
Keating, B., Timbie, P., Polnarev, A., & Steinberger, J. 1998, ApJ, 495, 580
King, O. G., Copley, C., Davies, R., et al. 2010, in SPIE Conf. Ser., 7741, 1
King, O. G., Jones, M. E., Blackhurst, E. J., et al. 2014, MNRAS, 438, 2426
Kogut, A., Banday, A. J., Bennett, C. L., et al. 1996, ApJ, 464, L5
Kogut, A., Dunkley, J., Bennett, C. L., et al. 2007, ApJ, 665, 355
Lazarian, A., & Draine, B. T. 2000, ApJ, 536, L15
Leitch, E. M., Readhead, A. C. S., Pearson, T. J., & Myers, S. T. 1997, ApJ, 486, L23
Lewis, A. 2013, J. Cosmol. Astropart. Phys., 8, 53
Liu, H., Mertsch, P., & Sarkar, S. 2014, ApJ, 789, L29
Macellari, N., Pierpaoli, E., Dickinson, C., & Vaillancourt, J. E. 2011, MNRAS, 418, 888
Magnani, L., Hartmann, D., Holcomb, S. L., Smith, L. E., & Thaddeus, P. 2000, ApJ, 535, 167
McClure-Griffiths, N. M., Pisano, D. J., Calabretta, M. R., et al. 2009, ApJS, 181, 398
Meisner, A. M., & Finkbeiner, D. P. 2015, ApJ, 798, 88
Moskalenko, I. V., & Strong, A. W. 1998, ApJ, 493, 694
Netterfield, C. B., Devlin, M. J., Jarosik, N., Page, L., & Wollack, E. J. 1997, ApJ, 474, 47
Orlando, E., & Strong, A. 2013, MNRAS, 436, 2127
Pacholczyk, A. G. 1970, Radio astrophysics. Nonthermal processes in galactic and extragalactic sources (San Francisco: Freeman)
Page, L., Hinshaw, G., Komatsu, E., et al. 2007, ApJS, 170, 335
Planck Collaboration ES. 2015, The Explanatory Supplement to the Planck 2015 results, http://wiki.cosmos.esa.int/planckpla/index.php/Main_Page (ESA)
Planck Collaboration XVIII. 2011, A&A, 536, A18
Planck Collaboration XX. 2011, A&A, 536, A20
Planck Collaboration XXI. 2011, A&A, 536, A21
Planck Collaboration I. 2014, A&A, 571, A1
Planck Collaboration V. 2014, A&A, 571, A5
Planck Collaboration VIII. 2014, A&A, 571, A8
Planck Collaboration IX. 2014, A&A, 571, A9
Planck Collaboration XI. 2014, A&A, 571, A11
Planck Collaboration XII. 2014, A&A, 571, A12
Planck Collaboration XIII. 2014, A&A, 571, A13
Planck Collaboration XIV. 2014, A&A, 571, A14
Planck Collaboration XVII. 2014, A&A, 571, A17
Planck Collaboration XXI. 2014, A&A, 571, A21
Planck Collaboration XXVII. 2014, A&A, 571, A27
Planck Collaboration XXVIII. 2014, A&A, 571, A28
Planck Collaboration XXX. 2014, A&A, 571, A30
Planck Collaboration I. 2016, A&A, 594, A1
Planck Collaboration II. 2016, A&A, 594, A2
Planck Collaboration III. 2016, A&A, 594, A3
Planck Collaboration IV. 2016, A&A, 594, A4
Planck Collaboration V. 2016, A&A, 594, A5
Planck Collaboration VI. 2016, A&A, 594, A6
Planck Collaboration VII. 2016, A&A, 594, A7
Planck Collaboration VIII. 2016, A&A, 594, A8
Planck Collaboration IX. 2016, A&A, 594, A9
Planck Collaboration X. 2016, A&A, 594, A10
Planck Collaboration XI. 2016, A&A, 594, A11
Planck Collaboration XII. 2016, A&A, 594, A12
Planck Collaboration XIII. 2016, A&A, 594, A13
Planck Collaboration XIV. 2016, A&A, 594, A14
Planck Collaboration XV. 2016, A&A, 594, A15
Planck Collaboration XVI. 2016, A&A, 594, A16
Planck Collaboration XVII. 2016, A&A, 594, A17
Planck Collaboration XVIII. 2016, A&A, 594, A18
Planck Collaboration XIX. 2016, A&A, 594, A19
Planck Collaboration XX. 2016, A&A, 594, A20
Planck Collaboration XXI. 2016, A&A, 594, A21
Planck Collaboration XXII. 2016, A&A, 594, A22
Planck Collaboration XXIII. 2016, A&A, 594, A23
Planck Collaboration XXIV. 2016, A&A, 594, A24
Planck Collaboration XXV. 2016, A&A, 594, A25
Planck Collaboration XXVI. 2016, A&A, 594, A26
Planck Collaboration XXVII. 2016, A&A, 594, A27
Planck Collaboration XXVIII. 2016, A&A, 594, A28
Planck Collaboration Int. X. 2013, A&A, 554, A140
Planck Collaboration Int. XV. 2014, A&A, 565, A103
Planck Collaboration Int. XVII. 2014, A&A, 566, A55
Planck Collaboration Int. XIX. 2015, A&A, 576, A104
Planck Collaboration Int. XX. 2015, A&A, 576, A105
Planck Collaboration Int. XXI. 2015, A&A, 576, A106
Planck Collaboration Int. XXII. 2015, A&A, 576, A107
Planck Collaboration Int. XXIII. 2015, A&A, 580, A13
Planck Collaboration Int. XXIX. 2016, A&A, 586, A132
Planck Collaboration Int. XXX. 2016, A&A, 586, A133
Press, W. H., Teukolsky, S. A., Vetterling, W. T., & Flannery, B. P. 2002, Numerical recipes in C++: the art of scientific computing (Cambridge: Cambridge Univ. Press)
Remazeilles, M., Dickinson, C., Banday, A. J., Bigot-Sazy, M.-A., & Ghosh, T. 2015, MNRAS, 451, 4311
Rephaeli, Y. 1995, ARA&A, 33, 541
Rubiño-Martín, J. A., López-Caraballo, C. H., Génova-Santos, R., & Rebolo, R. 2012, Adv. Astron., 2012, 40
Silsbee, K., Ali-Haïmoud, Y., & Hirata, C. M. 2011, MNRAS, 411, 2750
Strong, A. W., Moskalenko, I. V., & Ptuskin, V. S. 2007, Ann. Rev. Nucl. Part. Sci., 57, 285
Strong, A. W., Orlando, E., & Jaffe, T. R. 2011, A&A, 534, A54
Sunyaev, R. A., & Zeldovich, Y. B. 1972, Comm. Astrophys. Space Phys., 4, 173
Takekawa, S., Oka, T., Tanaka, K., et al. 2014, ApJS, 214, 2
Tucci, M., & Toffolatti, L. 2012, Adv. Astron., 2012, 52
Vidal, M., Dickinson, C., Davies, R. D., & Leahy, J. P. 2015, MNRAS, 452, 656
Wandelt, B. D., Larson, D. L., & Lakshminarayanan, A. 2004, Phys. Rev. D, 70, 083511
Wehus, I. K., Fuskeland, U., Eriksen, H. K., et al. 2016, A&A, in press, DOI: 10.1051/0004-6361/201525659
Yoda, T., Handa, T., Kohno, K., et al. 2010, PASJ, 62, 1277
Zaldarriaga, M., & Seljak, U. 1997, Phys. Rev. D, 55, 1830

[1] APC, AstroParticule et Cosmologie, Université Paris Diderot, CNRS/IN2P3, CEA/lrfu, Observatoire de Paris, Sorbonne Paris Cité, 10 rue Alice Domon et Léonie Duquet, 75205 Paris Cedex 13, France
[2] Aalto University Metsähovi Radio Observatory and Dept of Radio Science and Engineering, PO Box 13000, 00076 Aalto, Finland
[3] African Institute for Mathematical Sciences, 6–8 Melrose Road, Muizenberg 7945, Cape Town, South Africa
[4] Agenzia Spaziale Italiana Science Data Center, via del Politecnico snc, 00133 Roma, Italy
[5] Aix-Marseille Université, CNRS, LAM (Laboratoire d'Astrophysique de Marseille) UMR 7326, 13388 Marseille, France
[6] Astrophysics Group, Cavendish Laboratory, University of Cambridge, J J Thomson Avenue, Cambridge CB3 0HE, UK

[7] Astrophysics & Cosmology Research Unit, School of Mathematics, Statistics & Computer Science, University of KwaZulu-Natal, Westville Campus, Private Bag X54001, 4000 Durban, South Africa
[8] Atacama Large Millimeter/submillimeter Array, ALMA Santiago Central Offices, Alonso de Cordova 3107, Vitacura, 763 0355 Casilla, Santiago, Chile
[9] CGEE, SCS Qd 9, Lote C, Torre C, 4° andar, Ed. Parque Cidade Corporate, CEP 70308-200, Brasília, DF, Brazil
[10] CITA, University of Toronto, 60 St. George St., Toronto, ON M5S 3H8, Canada
[11] CNRS, IRAP, 9 Av. colonel Roche, BP 44346, 31028 Toulouse Cedex 4, France
[12] CRANN, Trinity College, Dublin, Ireland
[13] California Institute of Technology, Pasadena, CA 91125, USA
[14] Centre for Theoretical Cosmology, DAMTP, University of Cambridge, Wilberforce Road, Cambridge CB3 0WA, UK
[15] Centro de Estudios de Física del Cosmos de Aragón (CEFCA), Plaza San Juan, 1, planta 2, 44001 Teruel, Spain
[16] Computational Cosmology Center, Lawrence Berkeley National Laboratory, Berkeley, CA 94720, USA
[17] Consejo Superior de Investigaciones Científicas (CSIC), 28006 Madrid, Spain
[18] DSM/Irfu/SPP, CEA-Saclay, 91191 Gif-sur-Yvette Cedex, France
[19] DTU Space, National Space Institute, Technical University of Denmark, Elektrovej 327, 2800 Kgs. Lyngby, Denmark
[20] Département de Physique Théorique, Université de Genève, 24 quai E. Ansermet, 1211 Genève 4, Switzerland
[21] Departamento de Astrofísica, Universidad de La Laguna (ULL), 38206 La Laguna, Tenerife, Spain
[22] Departamento de Física, Universidad de Oviedo, Avda. Calvo Sotelo s/n, 33007 Oviedo, Spain
[23] Department of Astronomy and Astrophysics, University of Toronto, 50 Saint George Street, Toronto, Ontario, Canada
[24] Department of Astrophysics/IMAPP, Radboud University Nijmegen, PO Box 9010, 6500 GL Nijmegen, The Netherlands
[25] Department of Physics & Astronomy, University of British Columbia, 6224 Agricultural Road, Vancouver, British Columbia, Canada
[26] Department of Physics and Astronomy, Dana and David Dornsife College of Letter, Arts and Sciences, University of Southern California, Los Angeles, CA 90089, USA
[27] Department of Physics and Astronomy, University College London, London WC1E 6BT, UK
[28] Department of Physics, Florida State University, Keen Physics Building, 77 Chieftan Way, Tallahassee, Florida, USA
[29] Department of Physics, Gustaf Hällströmin katu 2a, University of Helsinki, 00014 Helsinki, Finland
[30] Department of Physics, Princeton University, Princeton, NJ 08544, USA
[31] Department of Physics, University of California, Santa Barbara, CA 93106, USA
[32] Department of Physics, University of Illinois at Urbana-Champaign, 1110 West Green Street, Urbana, Illinois, USA
[33] Dipartimento di Fisica e Astronomia G. Galilei, Università degli Studi di Padova, via Marzolo 8, 35131 Padova, Italy
[34] Dipartimento di Fisica e Scienze della Terra, Università di Ferrara, via Saragat 1, 44122 Ferrara, Italy
[35] Dipartimento di Fisica, Università La Sapienza, P.le A. Moro 2, 00185 Roma, Italy
[36] Dipartimento di Fisica, Università degli Studi di Milano, via Celoria 16, 20133 Milano, Italy
[37] Dipartimento di Fisica, Università degli Studi di Trieste, via A. Valerio 2, Trieste, Italy
[38] Dipartimento di Matematica, Università di Roma Tor Vergata, via della Ricerca Scientifica 1, 00133 Roma, Italy
[39] Discovery Center, Niels Bohr Institute, Blegdamsvej 17, 2100 Copenhagen, Denmark
[40] Discovery Center, Niels Bohr Institute, Copenhagen University, Blegdamsvej 17, 2100 Copenhagen, Denmark
[41] European Southern Observatory, ESO Vitacura, Alonso de Cordova 3107, Vitacura, 19001 Casilla, Santiago, Chile
[42] European Space Agency, ESAC, Planck Science Office, Camino bajo del Castillo, s/n, Urbanización Villafranca del Castillo, 28692 Villanueva de la Cañada, Madrid, Spain
[43] European Space Agency, ESTEC, Keplerlaan 1, 2201 AZ Noordwijk, The Netherlands
[44] Gran Sasso Science Institute, INFN, viale F. Crispi 7, 67100 L'Aquila, Italy
[45] HGSFP and University of Heidelberg, Theoretical Physics Department, Philosophenweg 16, 69120 Heidelberg, Germany
[46] Haverford College Astronomy Department, 370 Lancaster Avenue, Haverford, PA 19041, USA
[47] Helsinki Institute of Physics, Gustaf Hällströmin katu 2, University of Helsinki, 00014 Helsinki, Finland
[48] INAF–Osservatorio Astrofisico di Catania, via S. Sofia 78, 95123 Catania, Italy
[49] INAF–Osservatorio Astronomico di Padova, Vicolo dell'Osservatorio 5, 35122 Padova, Italy
[50] INAF–Osservatorio Astronomico di Roma, via di Frascati 33, 00040 Monte Porzio Catone, Italy
[51] INAF–Osservatorio Astronomico di Trieste, via G. B. Tiepolo 11, 40127 Trieste, Italy
[52] INAF/IASF Bologna, via Gobetti 101, 40129 Bologna, Italy
[53] INAF/IASF Milano, via E. Bassini 15, 20133 Milano, Italy
[54] INFN, Sezione di Bologna, viale Berti Pichat 6/2, 40127 Bologna, Italy
[55] INFN, Sezione di Ferrara, via Saragat 1, 44122 Ferrara, Italy
[56] INFN, Sezione di Roma 1, Università di Roma Sapienza, P.le Aldo Moro 2, 00185 Roma, Italy
[57] INFN, Sezione di Roma 2, Università di Roma Tor Vergata, via della Ricerca Scientifica 1, 00185 Roma, Italy
[58] INFN/National Institute for Nuclear Physics, via Valerio 2, 34127 Trieste, Italy
[59] IPAG: Institut de Planétologie et d'Astrophysique de Grenoble, Université Grenoble Alpes, IPAG; CNRS, IPAG, 38000 Grenoble, France
[60] IUCAA, Post Bag 4, Ganeshkhind, Pune University Campus, 411 007 Pune, India
[61] Imperial College London, Astrophysics group, Blackett Laboratory, Prince Consort Road, London, SW7 2AZ, UK
[62] Infrared Processing and Analysis Center, California Institute of Technology, Pasadena, CA 91125, USA
[63] Institut Néel, CNRS, Université Joseph Fourier Grenoble I, 25 rue des Martyrs, Grenoble, France
[64] Institut Universitaire de France, 103 bd Saint-Michel, 75005 Paris, France
[65] Institut d'Astrophysique Spatiale, CNRS, Univ. Paris-Sud, Université Paris-Saclay, Bât. 121, 91405 Orsay Cedex, France
[66] Institut d'Astrophysique de Paris, CNRS (UMR 7095), 98bis boulevard Arago, 75014 Paris, France
[67] Institut für Theoretische Teilchenphysik und Kosmologie, RWTH Aachen University, 52056 Aachen, Germany
[68] Institute of Astronomy, University of Cambridge, Madingley Road, Cambridge CB3 0HA, UK
[69] Institute of Theoretical Astrophysics, University of Oslo, Blindern, 0371 Oslo, Norway
[70] Instituto de Astrofísica de Canarias, C/Vía Láctea s/n, La Laguna, 38205 Tenerife, Spain
[71] Instituto de Física de Cantabria (CSIC-Universidad de Cantabria), Avda. de los Castros s/n, 39005 Santander, Spain
[72] Istituto Nazionale di Fisica Nucleare, Sezione di Padova, via Marzolo 8, 35131 Padova, Italy
[73] Jet Propulsion Laboratory, California Institute of Technology, 4800 Oak Grove Drive, Pasadena, CA 31109, USA
[74] Jodrell Bank Centre for Astrophysics, Alan Turing Building, School of Physics and Astronomy, The University of Manchester, Oxford Road, Manchester, M13 9PL, UK
[75] Kavli Institute for Cosmological Physics, University of Chicago, Chicago, IL 60637, USA

[76] Kavli Institute for Cosmology Cambridge, Madingley Road, Cambridge, CB3 0HA, UK
[77] Kazan Federal University, 18 Kremlyovskaya St., 420008 Kazan, Russia
[78] LAL, Université Paris-Sud, CNRS/IN2P3, 91898 Orsay, France
[79] LERMA, CNRS, Observatoire de Paris, 61 avenue de l'Observatoire, 75014 Paris, France
[80] Laboratoire AIM, IRFU/Service d'Astrophysique – CEA/DSM – CNRS – Université Paris Diderot, Bât. 709, CEA-Saclay, 91191 Gif-sur-Yvette Cedex, France
[81] Laboratoire Traitement et Communication de l'Information, CNRS (UMR 5141) and Télécom ParisTech, 46 rue Barrault, 75634 Paris Cedex 13, France
[82] Laboratoire de Physique Subatomique et Cosmologie, Université Grenoble-Alpes, CNRS/IN2P3, 53 rue des Martyrs, 38026 Grenoble Cedex, France
[83] Laboratoire de Physique Théorique, Université Paris-Sud 11 & CNRS, Bâtiment 210, 91405 Orsay, France
[84] Lawrence Berkeley National Laboratory, Berkeley, California, USA
[85] Lebedev Physical Institute of the Russian Academy of Sciences, Astro Space Centre, 84/32 Profsoyuznaya st., GSP-7, 117997 Moscow, Russia
[86] Max-Planck-Institut für Astrophysik, Karl-Schwarzschild-Str. 1, 85741 Garching, Germany
[87] Max-Planck-Institut für Extraterrestrische Physik, Giessenbachstraße, 85748 Garching, Germany
[88] McGill Physics, Ernest Rutherford Physics Building, McGill University, 3600 rue University, Montréal, QC, H3A 2T8, Canada
[89] National University of Ireland, Department of Experimental Physics, Maynooth, Co. Kildare, Ireland
[90] Nicolaus Copernicus Astronomical Center, Bartycka 18, 00-716 Warsaw, Poland
[91] Niels Bohr Institute, Blegdamsvej 17, 2100 Copenhagen, Denmark
[92] Niels Bohr Institute, Copenhagen University, Blegdamsvej 17, 2100 Copenhagen, Denmark
[93] Nordita (Nordic Institute for Theoretical Physics), Roslagstullsbacken 23, 106 91 Stockholm, Sweden
[94] Optical Science Laboratory, University College London, Gower Street, WC1E 6BT London, UK
[95] SISSA, Astrophysics Sector, via Bonomea 265, 34136 Trieste, Italy
[96] SMARTEST Research Centre, Università degli Studi e-Campus, via Isimbardi 10, 22060 Novedrate (CO), Italy
[97] School of Physics and Astronomy, Cardiff University, Queens Buildings, The Parade, Cardiff, CF24 3AA, UK
[98] School of Physics and Astronomy, University of Nottingham, Nottingham NG7 2RD, UK
[99] Sorbonne Université-UPMC, UMR 7095, Institut d'Astrophysique de Paris, 98bis boulevard Arago, 75014 Paris, France
[100] Space Research Institute (IKI), Russian Academy of Sciences, Profsoyuznaya Str, 84/32, 117997 Moscow, Russia
[101] Space Sciences Laboratory, University of California, Berkeley, CA 94720, USA
[102] Special Astrophysical Observatory, Russian Academy of Sciences, Nizhnij Arkhyz, Zelenchukskiy region, 369167 Karachai-Cherkessian Republic, Russia
[103] Sub-Department of Astrophysics, University of Oxford, Keble Road, Oxford OX1 3RH, UK
[104] The Oskar Klein Centre for Cosmoparticle Physics, Department of Physics,Stockholm University, AlbaNova, 106 91 Stockholm, Sweden
[105] Theory Division, PH-TH, CERN, 1211, Geneva 23, Switzerland
[106] UPMC Univ. Paris 06, UMR 7095, 98bis boulevard Arago, 75014 Paris, France
[107] Université de Toulouse, UPS-OMP, IRAP, 31028 Toulouse Cedex 4, France
[108] Universities Space Research Association, Stratospheric Observatory for Infrared Astronomy, MS 232-11, Moffett Field, CA 94035, USA
[109] University of Granada, Departamento de Física Teórica y del Cosmos, Facultad de Ciencias, 18071 Granada, Spain
[110] University of Granada, Instituto Carlos I de Física Teórica y Computacional, 18071 Granada, Spain
[111] W. W. Hansen Experimental Physics Laboratory, Kavli Institute for Particle Astrophysics and Cosmology, Department of Physics and SLAC National Accelerator Laboratory, Stanford University, Stanford, CA 94305, USA
[112] Warsaw University Observatory, Aleje Ujazdowskie 4, 00-478 Warszawa, Poland